

Motion tracking tMRI datasets to quantify
abnormal left ventricle motion using Finite
Element Modelling



Susan Ipe MSc

Department of Computer Science

University of Hull

A thesis submitted for the degree of

Doctor of Philosophy

2015

For Malcolm

Acknowledgements

The research described in this document was a project at the Departments of Computer Science at the University of Hull that was jointly funded by the Departments of Computer Science and Biological Sciences.

Prof. Roger Phillips as the lead supervisor provided excellent guidance on the approaches and mechanisms to ensure the project progresses smoothly.

Prof. Michael Fagan from the Department of Engineering has been very helpful with the understanding of finite element analysis procedures for finite element models using ANSYS.

I would like to thank the Cardiac Atlas Project for the use of tMRI dataset without which the project would not have been possible. I would also like to thank Elliot McVeigh and Dr Leon Axel who guided me to the tMRI dataset when I had all but lost hope. Finally I thank my husband for his support.

Abstract

According to ‘The Atlas of Heart Disease and Stroke’[MMMG04] published by the World Health Organization, heart disease accounts for nearly half the deaths in both the developed and developing countries and is the world’s single biggest killer. However, early detection of a diseased heart condition can prevent many of these fatalities. Regional wall motion abnormalities of the heart precede both ECG abnormalities and chest pain as an indicator of myocardial ischaemia and are an excellent indicator of coronary stenosis [GZM97]. These motion abnormalities of the heart muscle are difficult to observe and track, because the heart is a relatively smooth organ with few landmarks and non-rigid motion with a twisting motion or tangential component. The MRI tissue-tagging technique gives researchers the first glimpse into how the heart actually beats. This research uses the tagged MRI images of the heart to create a three dimensional model of a beating heart indicating the stress of a region. Tagged MRI techniques are still developing and vary vastly, meaning that there needs to be a methodology that can adapt to these changes rapidly and effectively, to meet the needs of the evolving technology. The focus of this research is to develop and test such a methodology by the means of a Strain Estimation Pipeline along with an effective way of validating any changes made to the individual processes that it comprises of.

Contents

1	Introduction	1
1.1	Human heart anatomy	1
1.2	Heart disease	3
1.2.1	Heart performance and abnormalities in CAD	3
1.3	Non-invasive investigation of CAD	4
1.3.1	Electrocardiogram	4
1.3.2	Echocardiography	5
1.3.3	Chest radiography	5
1.4	MRI	6
1.4.1	Contrast imaging	6
1.4.2	Tissue tagging	7
1.4.3	Phase-contrast MRI	8
1.4.4	Displacement Encoding with Stimulated Echoes	8
1.4.5	Strain Encoded imaging	8
1.4.6	Comparison of MRI techniques used for tissue tracking	9
1.5	Aim	11
1.6	Research challenges and hypothesis	12
1.7	Objectives	13
1.8	Research path & thesis overview	14
2	Regional Strain Model using tMRI	17
2.1	tMRI techniques	17
2.1.1	Basic tMRI techniques	18
2.1.2	Advanced tMRI techniques	18
2.1.3	Challenges posed by tMRI	20

2.2	Capturing a tMRI slice	28
2.2.1	Ventricle of interest	28
2.2.2	Coordinate systems for RF induced tag planes	29
2.2.3	Coordinate systems for tMRI slice acquisition	29
2.2.4	Distance between slices & number of slices	30
2.2.5	Acquired tMRI dataset	31
2.3	Representing the data	31
2.3.1	Geometric model	32
2.3.2	Tag lines	33
2.4	Processing the tMRI	33
2.4.1	Image preparation	34
2.4.2	Boundary surface extraction and tag tracking	35
2.4.3	Tag tracking and motion estimation operating in the frequency domain	37
2.4.4	Motion estimation of myocardium operating in the spatial domain	38
2.4.5	Segmentation based motion estimation methods	42
2.5	Regional strain calculation	48
2.5.1	Frames of reference	48
2.5.2	Types of strain in the myocardium	49
2.5.3	Strain calculation	50
2.5.4	Calculated regional strain values	51
2.6	Visualization	51
2.7	Chapter summary	52
3	Processing tMRI datasets using a Strain Estimation Pipeline	54
3.1	Strain Estimation Pipeline	55
3.1.1	Calculation of strain	57
3.1.2	Estimation of motion	59
3.1.3	Creation of geometry	69
3.1.4	Extraction of features	74
3.2	Evaluation and validation of results	81
3.2.1	Validation of tMRI processing algorithms	82

3.2.2	Evaluation and validation of SEP	84
3.3	Implemented software tool chain	87
3.3.1	‘Extract Features’	88
3.3.2	‘Create FEM’	90
3.3.3	‘Estimate Motion’	91
3.3.4	‘Calculate Strain’	91
3.4	Chapter summary	93
4	Developing a Strain Estimation Pipeline	95
4.1	Overview of simulation pipeline	96
4.2	Generating the mathematical model	98
4.2.1	Creating the FEM	98
4.2.2	Creating the ‘Virtual Tag Planes’	101
4.3	Motion model simulation	103
4.3.1	Deforming forces	103
4.3.2	Application of forces	105
4.4	Acquisition of ‘Virtual Slices’	105
4.4.1	Acquisition coordinate axes and planes	106
4.4.2	Acquiring VTP information	108
4.4.3	Acquiring model wall contour information	108
4.5	Developing the SEP modules	109
4.5.1	‘Calculate Strain’	111
4.5.2	‘Estimate Motion’	113
4.5.3	‘Create FEM’	115
4.5.4	‘Extract Features’	118
4.6	Chapter summary	120
5	SEP Validation and Use	121
5.1	Methodology of validation	121
5.1.1	Measure of comparison	122
5.1.2	‘Estimate Motion’ algorithm variations	122
5.1.3	Simulated models	125
5.2	Validation tests using simulation	126
5.2.1	Mechanics model	126

5.2.2	Weight of selected MC points	126
5.2.3	Selection of MC points using threshold distances	128
5.2.4	Applied force patterns	128
5.2.5	Selection of MC points using threshold numbers	130
5.2.6	Location of selected MC points	132
5.2.7	Induced numbers of VTP	134
5.2.8	Acquired number of VS	134
5.2.9	Number of elements in FEM	136
5.3	Achieved accuracy of SEP	139
5.4	Analysis of tMRI dataset	142
5.4.1	Using the ‘Extract Features’ module to identify chamber walls and tag lines in tMRI data	142
5.4.2	Using the ‘Create FEM’ module to create an ANSYS FEM from the processed tMRI data	144
5.4.3	Using the ‘Estimate Motion’ module to estimate the deformation of the ANSYS FEM created from the processed tMRI data	145
5.4.4	Using the ‘Calculate Strain’ module to produce the regional strain pattern of the ANSYS FEM deformed using the processed tMRI data	146
5.4.5	Results of processing tMRI data using SEP	146
5.5	Chapter summary	146
6	Conclusions	148
6.1	Achieved objectives	150
6.1.1	SEP	151
6.1.2	Simulation pipeline as a method of evaluating the SEP	152
6.1.3	Validation of the SEP using simulation	153
6.1.4	Analyse tMRI data generating a regional strain pattern for the deforming myocardium	154
6.1.5	The relationship between the tMRI acquisition parameters and the accuracy of the reconstructed motion	154
6.1.6	Problems faced	155

CONTENTS

6.2	Future work	156
6.2.1	Limitations of current SEP tool	156
6.2.2	Extending the diagnostic tool	158
A		160
A.1	Electrocardiogram (ECG)	160
A.2	Ultrasound	160
A.3	Nuclear Medicine	161
A.4	Magnetic Resonance Imaging	162
A.4.1	The machine	162
A.4.2	Principles	163
B		165
B.1	Defining the conical volume	165
B.2	Defining the VTP	165
B.3	Springs	167
B.3.1	Forces acting along a spring	167

List of Figures

1.1	Cross-section of heart showing myocardial ischaemia	2
1.2	Tissue tagging pattern	7
1.3	Research path	16
2.1	Sample of SPAMM tMRI fading over three time steps	25
2.2	2D motion of points within a tag line	26
2.3	3D motion of points within a tag plane	26
2.4	Tag grid motion (3D)	29
2.5	Planes of slice acquisition for LV	30
2.6	Motion estimation by reconstruction of Virtual Tag Planes	43
3.1	Research stage: SEP	54
3.2	Strain Estimation Pipeline	55
3.3	Calculation of strain in SEP	57
3.4	Motion estimation, strain estimation & geometry creation in SEP	60
3.5	Partial displacement information	63
3.6	Motion meshes	64
3.7	Motion cloud (MC)	64
3.8	Selecting mesh points from MC	65
3.9	Springs connecting tag plane points	68
3.10	Strain estimation & geometry creation in SEP	69
3.11	Step one of creating the FEM	71
3.12	Step two of creating the FEM	72
3.13	Calculating the FEM nodes	73
3.14	‘Throwing’ of radial rays to create FEM elements	73

LIST OF FIGURES

3.15	Specification of elements of type SOLID185 in ANSYS	74
3.16	Initial edge-based segmentation attempt	76
3.17	Canny edge-based segmentation	77
3.18	Basic active contour model based segmentation	78
3.19	Result of sparse field method	79
3.20	Using GVF to extract chamber walls	80
3.21	Final SEP with the expected inputs and outputs	81
3.22	Validating the SEP	85
3.23	Software tool chain	87
3.24	Data flow when extracting features from tMRI dataset	88
3.25	Segmentation software tool chain	88
3.26	Segmented slices in scalable vector graphics (SVG)	89
3.27	Data flow to create FEM	90
3.28	Software tool chain to create FEM	90
3.29	Data flow to estimate motion	91
3.30	Software tool chain used to estimate motion of FEM	92
3.31	Data flow to calculate strain	92
3.32	Software tool chain used to calculate regional strain of FEM	93
4.1	Research stage: simulation pipeline	95
4.2	‘Virtual Slice’ simulation	97
4.3	Conical volume definition	99
4.4	Cross-section of conical volume changes with number of sectors . .	99
4.5	Conical simulation volume	100
4.6	Virtual tag plane definition	101
4.7	VTP points (LINK180) and influencing nodes (SOLID185)	103
4.8	Forces to mimic motion of heart	104
4.9	Regional force	105
4.10	Planes of acquiring simulated tMRI slices of mathematical model	107
4.11	Sample of virtual tMRI slices that will be acquired	107
4.12	Virtual tag line	108
4.13	Model wall contour	109
4.14	Validating the SEP	110

LIST OF FIGURES

4.15	Evaluation of ‘Calculate Strain’ using simulation data	112
4.16	Evaluation of ‘Estimate Motion’ using simulation data	114
4.17	Evaluation of ‘Create FEM’ using simulation data	116
4.18	Results of refining	117
4.19	Evaluation of ‘Extract Features’ using simulation data	119
5.1	Research stage: validation	121
5.2	Validation of SEP using Lagrangian motion estimation	127
5.3	Validation of SEP using Newtonian motion estimation	127
5.4	Varying weights of MC points	128
5.5	Varying weights of MC points - coordinate components	129
5.6	Varying threshold distances of MC points	130
5.7	Varying force patterns	131
5.8	Varying threshold numbers	131
5.9	Varying threshold numbers with non-uniform force pattern applied	132
5.10	Varying threshold space	133
5.11	Location based algorithm	133
5.12	Varying numbers of VTP	134
5.13	Error components for varying number of VTP	135
5.14	Varying number of VS with even & uneven forces	135
5.15	Error components for varying number of VS	136
5.16	Varying number of FEM elements	137
5.17	Varying number of FEM elements using location based selection algorithm	137
5.18	Error components for varying number of FEM elements - coordi- nate components	138
5.19	RMSE results for each validation test run	140
5.20	RMSE results for the different sections of the model	141
5.21	Chamber section specific rmse results for varying number of FEM elements	141
5.22	Research stage: cardiac strain patterns using SEP	142
5.23	tMRI LA slices at time step 0 and 24	143
5.24	Chamber wall identification	143

LIST OF FIGURES

5.25	Identified tag lines at time step t22	144
5.26	tMRI result of SEP before FEM analysis	145
6.1	Initial tMRI image before segmentation	156
B.1	Calculation of points on concentric circles of volume	165
B.2	Calculation of points along length of conical volume	166
B.3	Intersection types One & Two	166
B.4	Intersection types Three & Four	167
B.5	Padding of a line with additional points	167

List of Tables

1.1	Suitability of different imaging modalities in identifying key abnormalities in CAD	5
1.2	MRI techniques used for tissue tagging	10
2.1	Basic tMRI techniques	19
2.2	Comparison of SPAMM tMRI techniques	19
2.3	Comparison of CSPAMM tMRI techniques	19
2.4	Advanced tMRI Techniques	21
2.5	Comparison of HARP tMRI Techniques	21
2.6	Comparison of DENSE tMRI Techniques	22
2.7	Comparison of SENC tMRI Techniques	22
2.8	Details of acquired dataset	31
2.9	Estimating Motion	39
3.1	Algorithm for Motion Estimation	61
3.2	Algorithm for weighted contribution of selected MC points	62
3.3	Algorithm to enforce that a given number of MC points are selected	66
3.4	Algorithm to enforce that the selected MC points are not more than a maximum distance away from the node	66
3.5	Algorithm for a spatially aware selection of MC points	67
3.6	Algorithm to compute motion using analytical mechanics	68
4.1	Overview of Simulation Pipeline processes	97

1

Introduction

In 2009, over 180,000 people died from cardiovascular disease, accounting for one in three of all deaths in the UK, according to the British Heart Foundation (BHF). As of the 2010 BHF report [BHF10], there are nearly 2.7 million people in the UK with coronary heart diseases.

The first sections discuss the basic medical context, explaining why it is important to develop a diagnostic tool for coronary artery disease (CAD) and myocardial ischaemia and how these conditions can be detected. This is followed by an overview of the available non-invasive technology to investigate cardiac function and in turn the onset of CAD using the MRI technologies of tissue tagging, phase-contrast MRI, displacement encoded MRI and strain encoded MRI.

1.1 Human heart anatomy

The heart is an involuntary muscle that has approximately seventy to ninety contractions per minute during a restful state. Each side of the heart works as two separate pumps, each with two chambers, an atrium and a ventricle, on two different sides of the heart separated by a wall of muscle called the septum. The atria act as reservoirs for blood with a small pumping action to assist ventricular filling. The ventricles are larger pumping chambers for delivering blood to the pulmonary and systemic circulations. The heart has four valves that ensure the flow of blood in the required direction, from atria to ventricle (tricuspid and mitral valves), and then to the arterial circulations (pulmonary and aortic valves).

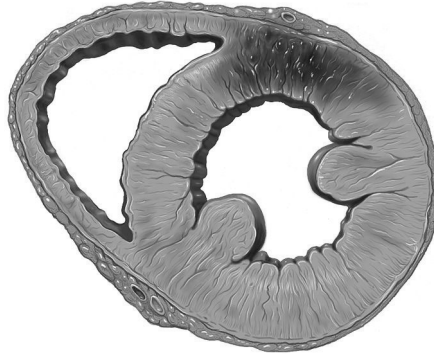


Figure 1.1: Cross-section of heart showing myocardial ischaemia
(www.peacehealth.org/OHVI/HeartRhythmSvc.htm) accessed in August 2008

The contraction of the heart begins in the atria and causes the blood to be squeezed out into the ventricles. The ventricle begins its work of pumping blood as the atrium finishes its squeeze. The active action of these two chambers working together is called systole. Each of these active periods will be followed by a short resting period known as diastole, although the heart never actually stops.

The right atrium is the thin-walled area that receives the oxygen and nutrient depleted blood returning from the tour of the body. This blood is emptied into the right ventricle (RV), which pumps the blood into the blood vessels of the lungs where the blood is oxygenated. The left atrium receives this oxygenated blood and pumps it into the left ventricle (LV). The LV is the largest and strongest chamber with walls about half an inch thick doing the majority of the work pumping the blood around the body.

The walls of the heart are made of three distinct layers, the endocardium, myocardium and pericardium. The endocardium forms the interior membrane and the valves of the heart. The myocardium is the actual muscle tissue of the heart and is by far the thickest layer and finally the pericardium is the outer layer. The heart muscle receives oxygen from the blood that flows through a group of arteries that begins less than half an inch from where the aorta begins. These arteries are known as the coronary arteries which deliver oxygen to both

the heart muscle and the nerves of the heart.

1.2 Heart disease

Based on the complexity of the heart and its proper functioning, it is clear that there may be numerous causes for disease. These diseases can be classified according to the cause and the region affected. Heart disease can be caused by congenital defects or by the malfunctioning of heart muscles or nerves. Congenital heart disease refers to any cardiac lesions present from birth while heart diseases caused by the malfunctioning of nerves include disorders of rate, rhythm and conduction. Heart diseases caused by malfunctioning heart muscles include disease of cardiac valves, disease of the pericardium and disease of the myocardium. Diseases caused by the disruption of blood flow to the heart muscle include CAD and disease of the aorta. Systemic disorders and hypertension are also known to affect the functioning of the human heart.

Among the more fatal heart diseases are those caused by myocardial malfunctioning. Heart failure and CAD, which includes angina pectoris and acute myocardial infarction, are examples of diseases that affect the myocardium. Cardiomyopathy and myocarditis are relatively uncommon types of myocardial disease that cannot be attributed to coronary atherosclerosis, congenital or valvular heart disease or hypertension.

1.2.1 Heart performance and abnormalities in CAD

A wide variety of parameters are used to evaluate the performance of the heart muscle. Some of these parameters are radial thickening, circumferential shortening, longitudinal shortening, the time derivatives of these quantities and the Eigen vectors and Eigen values of the strain tensor. The important abnormalities that are indicative of CAD, as identified in [JCM05], are as listed below.

- **Myocardial perfusion:** The myocardial perfusion test evaluates the blood flow within the heart tissue and the function of the heart muscle layers. Myocardial perfusion imaging is also used to evaluate previous damage to the heart and risk of future heart damage.

- **Wall motion / thickening:** Abnormalities of heart wall motion and/or thickness both indicate a diseased heart.
- **Myocardial hibernation:** It is important to identify hibernating myocardium as these are regions that show improvement in function after revascularization. Hibernating myocardium is defined as reversible left ventricular dysfunction due to chronic CAD.
- **Transmural extent of infarction:** This refers to finding the transmural extent or the depth (from the endocardium through the myocardium to the epicardium) of the affected area of the heart muscle.
- **Coronary stenosis:** Coronary stenosis refers to the constriction or narrowing of coronary arteries. Constriction of the coronary arteries results in reduced blood supply to the heart muscles and may result in infarction, subsequently hibernation or necrosis of heart muscle tissue.

1.3 Non-invasive investigation of CAD

The non-invasive investigation techniques of CAD are using electrocardiogram (ECG) and cardiac imaging of which, echocardiogram or ultrasound and chest radiography are a part.

1.3.1 Electrocardiogram

The ECG is the first line of non-invasive investigation for coronary disease with the tests conducted in states of rest and stress (induced by exercise). ECG interpretation is however largely a matter of experience and pattern interpretation. Additionally, the sensitivity and specificity of the test are limited and it can not measure regional myocardial tissue viability or the transmural extent of infarction. The principle behind the working of ECG can be found in Appendix A.

1.3 Non-invasive investigation of CAD

Table 1.1: Suitability of different imaging modalities in identifying key abnormalities in CAD

reproduced from [JCM05]

	Perfusion	Wall Motion / Thickening	Hibernation	Transmural Extent of Infarction	Coronary Stenosis
Stress Echo	+	+++	++	+	-
Nuclear Medicine	+++	+	+	+	-
MRI	++	+++	++	+++	+

1.3.2 Echocardiography

Echocardiography is used to investigate ventricle dimensions and function as well as valve lesions. It is also used to detect regional wall motion abnormalities.

Echocardiography is used to detect pressure differences across narrowed valves and to estimate pulmonary artery pressure using tissue Doppler imaging. However velocities measured by tissue Doppler imaging are angle dependent and, like all echocardiographic techniques, may be limited by poor acoustic windows and operator dependence. Echocardiography is limited in its detection of regional abnormalities and tissue viability. The reasons for this limitation can be understood from the principles of its working found in Appendix A.

1.3.3 Chest radiography

Imaging modalities can be used to evaluate myocardial perfusion, regional wall motion and thickening, myocardial hibernation and transmural extent of infarction. Imaging techniques allow the opportunity to diagnose coronary heart disease without the need for invasive procedures that may encounter complications due to the use of anaesthetics. The most common imaging modalities widely used for evaluating cardiac function is echocardiography, nuclear medicine (SPECT, PET) and MRI and the suitability of each to detect the important abnormalities in CAD have been compared in table 1.1. The basic principles behind the working of these imaging modalities can be found in Appendix A.

Although the use of nuclear medicine is the accepted standard in clinical practise to measure myocardial perfusion, MRI offers the advantage of increased

spatial resolution and the absence of overlying tissue attenuation effects. It is clear from the table that, on the whole, MRI is better able to detect the important abnormalities in CAD.

1.4 MRI

Cine MRI is critical in imaging the anatomy of the heart and calculating global indexes but has limited ability to track local motion. Regional wall motion abnormalities of the heart precede both ECG abnormalities and chest pain as an indicator of myocardial ischaemia and is an excellent indicator of coronary stenosis [GZM97]. Regional wall motion abnormalities are a result of reduced blood flow indicating blocked coronary arteries. Due to the complexity in imaging the coronary arteries, the focus is on the imaging of the myocardium. Since the regional wall motion abnormalities of the heart precede other indicators of myocardial ischaemia, detecting these motion abnormalities will be the main focus of the research project. The following sections briefly discuss the techniques currently used in investigating myocardial function.

1.4.1 Contrast imaging

In contrast imaging, the heart is imaged after the administration of a contrast agent (normally containing gadolinium).

1.4.1.1 Enhancement MRI

The most common technique for cardiac perfusion MRI uses ‘T1 - enhancement’, in which the myocardial signal increases as the contrast agent perfuses the heart. Regions of ischaemia with poor perfusion will show a significantly delayed enhancement compared to the normal regions. The symptoms of impaired myocardial blood flow are usually only apparent when the patient is under stress, which needs to be pharmacologically induced (using adenosine) for MRI.

1.4.1.2 Delayed-enhancement MRI

Delayed enhancement imaging is the technique used to directly image the non-viable myocardial region. The image slice is acquired at approximately ten minutes after contrast administration. It is exclusively related to irreversible injury, irrespective of contractile function or age of injury. Delayed enhancement imaging can thus be used to diagnose myocardial hibernation and the extent of infarction.

1.4.2 Tissue tagging

Creating MRI tags in a tissue provides a way of visualising its movement. Spin tagging prepulses produce non-invasive markers in the myocardial tissue that persist during at least part of the cardiac cycle (usually systole). The tag patterns fade because of T1 relaxation of the magnetisation. The varying magnetisation produces alternating light and dark pattern on the image, as seen in figure 1.2, that is typically separated by 4-8mm.

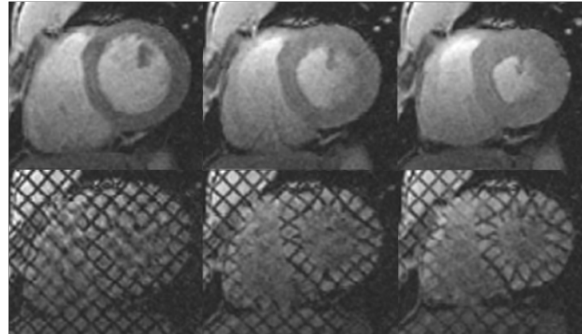


Figure 1.2: Tissue tagging pattern

The accuracy of the tagged MRI (tMRI) has been verified using sonomicrometry by Yeon [YRT⁺01]. The research by Croisille [CMJ99] demonstrates that the use of tMRI can distinguish viable from nonviable myocardial tissue after an ischaemic injury as well as show evidence of restoration of function after treatment. The most commonly used approach to track the three dimensional (3D) motion of the heart is by using multiple orthogonal image planes to cover the volume of interest. Myocardial tagging was first introduced by Zerhouni

[ZPR⁺88] and Axel [AD89b]. Researchers have since then developed various tagging schemes, including higher-order SPAMM [AD89a], DANTE [MS90], radial tags [BMZ90], hybrid SPAMM-DANTE [MA92] and sinc-modulated DANTE [WTT02]. SPAMM [AD89b] and CSPAMM [FMMB93] are the most commonly used tagging sequences.

1.4.3 Phase-contrast MRI

Phase-contrast MRI is based on the idea that the motion of tissue on blood produces a change in the MR signal phase that is proportional to the velocity of the tissue. It is for this reason that phase-contrast MRI is also called velocity-encoded MRI. The procedure is to have a reference scan without velocity encoding followed by two or three further acquisitions with velocity encodings along different directions. The velocity information in velocity-encoded MRI can be used to directly calculate strain rate by integrating with respect to time.

1.4.4 Displacement Encoding with Stimulated Echoes

Aletras [ADBW99] created a new technique named displacement encoding with stimulated echoes (DENSE) which combines many of the advantages of tissue tagging and phase-contrast mapping. DENSE is a high resolution myocardial displacement mapping method. The phase of the DENSE images is proportional to the displacement. Three RF pulses are used to generate a stimulated echo while displacement, as in phase-contrast MRI, is encoded directly into the signal phase. Details of the technique can be found in the [ADBW99] paper. DENSE has the advantage of having simple and quick post-processing. However, as pointed out by Simpson [SKF12], the encoding does not last for the whole cardiac cycle due to T1 recovery as seen in tissue tagging. In addition, since the sequence is based on a stimulated echo, the technique has intrinsically low SNR.

1.4.5 Strain Encoded imaging

The unique advantage of strain-encoded (SENC) imaging is that it directly encodes the regional strain of the heart into the acquired image without measuring

the displacement or velocity. Developed by Osman [OSAP01], SENC, uses tag planes parallel to the image planes to encode one dimensional out-of-plane strain. According to Osman [Osm03], the existence of stiff masses can be detected in the acquired SENC images without post-processing.

SENC is often used in conjunction with other techniques to obtain 3D information. Sampath [SOP09] integrates SENC with HARP, a tissue tagging technique that can produce 2D in-plane strain while Hess [HZS⁺09] combines DENSE and SENC to obtain 3D strain map in a single slice of myocardium.

1.4.6 Comparison of MRI techniques used for tissue tracking

Contrast imaging can indicate the area of reduced blood flow but has the drawback of requiring pharmacologically induced stress and a contrast agent.

Phase-contrast velocity mapping can show the total blood ejected from the LV during a cardiac cycle and is widely used to image blood flow and has been shown to be useful for measuring myocardial motion in CAD. It is however, prone to motion artefacts and phase distortion. Additionally, although strain can be calculated from phase velocity mapping, the integration process makes it sensitive to noise and most researchers have focused on reporting velocity and strain rate measurements.

DENSE combines many of the advantages of tagging and phase velocity mapping. However, since it is based on stimulated echo, there is an inherent 50% signal loss which is in addition to the problem that the encoding does not last for the whole cardiac cycle due to T1 recovery.

The main problem with SENC is that it cannot quantify in-plane strain without combining it with another technique like HARP (by Sampath [SDA⁺03]) or DENSE (by Hess [HZS⁺09]). SENC, like DENSE and tMRI also has the problem of fading through the cardiac cycle due to T1 recovery.

It is easy to see the features and relative advantages and disadvantages of the various MRI techniques in table 1.2 as reproduced from Simpson [SKF12].

One of the main disadvantages of phase contrast, DENSE and SENC is that they all need a longer preparation time than the original tMRI. tMRI also has the

Table 1.2: MRI techniques used for tissue tagging
reproduced from [SKF12]

	Tagging	Tagging w/HARP	SENC	DENSE	Phase Velocity
What does it measure	Displacement by following tags	Motion of pixels of consistent phase	Strain encoded in intensity pixel by pixel	Displacement encoded in phase pixel by pixel	Velocity encoded in phase pixel by pixel
How to get strain	Lagrangian strain from difference in distance between two points at two time points	Eulerian strain from spatial gradient of phase	Directly measures Eulerian strain	Eulerian strain calculated from displacement field using finite element analysis	Velocity from phase map is related to Eulerian strain-rate
		Lagrangian strain from following points of invariant phase		Lagrangian strain from cine DENSE between two time points	Integrate to get strain
Spatial resolution	Limited by tag spacing	Limited to pixel size but is much reduced due to required k-space filter	Limited to pixel	Limited to pixel size but can be reduced due to reduced due to k-space filter	Limited to pixel size
Advantages	Visually appealing	Quick processing	Through plane measurements	Quick processing	Standard on scanners
	Tissue tracking techniques allow generation of strain-time curves	Used clinically	Very quick processing	High precision	Quick processing
		Tissue tracking techniques allow generation of strain-time curves		Tissue tracking techniques allow generation of strain-time curves	Can analyse entire cycle
Disadvantages	Slow processing	Low SNR due to selecting one spectral peak	Not widely tested	Not widely tested	High Precision Prone to motion artefacts
	Tags fade through cycle	Tags fade through cycle	Low SNR	Low SNR due to selecting one spectral peak	Integrating to get strain leads to error propagation
			Cannot measure radial strain	Tags fade through cycle	High resolution images require lengthy acquisition times
			Tags fade through cycle		

advantage of being less sensitive to artefacts and having a higher achievable time resolution. With the ongoing advances in gradient technology, image reconstruction techniques and data analysis algorithms, tMRI has become the reference modality for calculating strain in the heart. According to Wang [WA12], tMRI is becoming the gold standard for quantifying regional function. tMRI techniques can, thus, be used to study in vivo regional heart muscle motion and better understand both normal and abnormal cardiac physiology.

1.5 Aim

On account of the large numbers of people affected by CAD, the motivation of the research was first identified as the development of a tool to diagnose and investigate CAD and myocardial ischaemia. As explained before, indications of CAD and myocardial ischaemia include abnormalities in the regional wall motion and myocardial perfusion, the presence of myocardial hibernation, the transmural extent of infarction and coronary stenosis. Although coronary stenosis is the first sign of CAD, it is demanding to detect and image. Thus making regional wall motion abnormality the first indication of CAD that is feasible to investigate. The regional abnormal wall motion can indicate the region of coronary stenosis and thus narrow the search for the affected arteries that feed the tissue to begin possible treatment reducing the required scans and associated radiation.

The discovery of the importance of the regional wall abnormalities of the LV in the diagnosis and investigation of CAD and myocardial ischaemia leads to the refinement of the research to focus on the development of a diagnostic tool to identify abnormalities in wall motion of the LV in order to identify and investigate CAD and myocardial ischaemia.

As discussed in previous sections, using different techniques, the use of MRI is well suited to detect all of the signs of CAD and myocardial ischaemia. Currently with MRI, regional wall motion abnormalities can be detected by tagging the myocardial tissues or using phase-contrast velocity mapping, while myocardial perfusion, hibernation and the transmural extent of ischaemic necrosis can be detected by using delayed-enhancement imaging using a contrast agent usually containing gadolinium. The use of tMRI is establishing itself as a standard means

1.6 Research challenges and hypothesis

to reduce the need for invasive investigations and has resulted in an improved understanding of the working of the heart tissues. With this establishment of tMRI as a means to detect regional wall motion abnormalities, the focus of the research is further refined to become the development of a diagnostic tool to identify abnormalities in wall motion of the LV in order to identify and investigate CAD and myocardial ischaemia using tMRI.

However, tMRI is a rapidly developing technique that requires a software methodology that can be used to identify regional motion abnormalities, and can adapt effectively to meet the needs of the evolving technology. The aim of this research is hence to develop and test such a methodology along with an effective way of validating any changes made.

1.6 Research challenges and hypothesis

The first challenge in developing a diagnostic tool for CAD and myocardial ischaemia using information from tMRI slices is to identify the processes to calculate the three dimensional strain pattern of the LV from the two dimensional tMRI slice information. The second major challenge is that tissue tagging techniques vary vastly between themselves and are constantly improving, with a consequent constant need for new software tools. Thus, in order for the developed diagnostic tool to remain relevant, the tool needs to be easy to modify whenever required. The diagnostic tool developed thus needs to be capable of calculating the regional strain model of the LV from tMRI slice information regardless of the actual tissue tagging technique used. This may be possible if the diagnostic tool is designed and implemented as a standard set of modules that adapt to changes in the technology used by modifying or swapping out existing algorithms of individual modules allowing for the reuse of software.

The final challenge is the validation of the methods or methodology used to process the tMRI and reconstruct or estimate the regional motion of the LV walls. Validation of the methods used to process tMRI slices often involve ex-vivo data or the visual and expert manual verification of results against in-vivo data as discussed in Chapter 3. For instance, the accuracy of motion reconstruction methods is done by visual corroboration or by overlaying the results with the tMRI slices

and/or delayed-enhancement images. Although this method is acceptable it is not always possible to acquire both sets of data at the same time and the patient may become stressed due to the amount of time it would take to acquire all the required images which in turn could cause an inadvertent discrepancy of results. In addition, this is still incomplete information since overlaying can only tell us if the motion is accurately reconstructed on the acquisition planes. Thus, a better method of validating and quantifying the accuracy of the results is required. It is for these reasons that simulation is proposed as a method by which to validate the results of a diagnostic tool and quantify its results. It is possible to use simulation as a validation mechanism because the 3D motion pattern of a mathematical model would be known, making it possible to compare and verify the results of the diagnostic tool and thus validate the tool and quantify its accuracy. A mathematical model that is used to validate the output of the tool would need to approximate the LV both in geometry and motion to be appropriate.

The hypothesis of this research project is thus that it is possible to develop a pipeline of procedures that is adaptable to changes in the requirements, using which to process tMRI slices of the LV to produce regional strain patterns. In addition, the results of the pipeline can be validated and its accuracy quantified using a simulated model of the LV.

1.7 Objectives

The focus of this research is to identify, develop and test a methodology to estimate strain patterns within the LV, in order to quantify the severity and extent of regional wall motion abnormalities, along with an effective way of validating the methodology and any changes made to it.

The identified objectives of the project are as follows:

- Obj 1 Identify the main modules that will process the tMRI data to calculate a regional strain model.
- Obj 2 Identify and implement a validation process for the modules identified (Obj 1).

- Obj 3 Implement and validate the modules used to calculate a regional strain model from tMRI data using the implemented validation process (Obj 2).
- Obj 4 Analyse tMRI data resulting in a motion model of the myocardium and the regional strain and stress maps for the deforming myocardium.
- Obj 5 Find a relationship between the distance between consecutive slices, the number of phases acquired, the tag plane distance and the accuracy of the reconstructed motion.

1.8 Research path & thesis overview

As presented in the previous section, the focus of this research is to identify, develop and test a methodology to estimate strain patterns within the LV to quantify the severity and extent of regional wall motion abnormalities, along with an effective way of validating the methodology and any changes made to it. The review of literature in Chapter 2, explains the requirements since processing tMRI data varies due to the large numbers of tMRI techniques available. The next chapter explains the various tissue tagging techniques along with their relative advantages and drawbacks. These tMRI techniques are rapidly improving and evolving which results in the need for a standard pipeline procedure to process a tMRI dataset to identify any abnormality in motion. A review and analysis of past research follows the acquisition of slices using tMRI, the processing of the slices to construct a regional strain model, problems faced in calculating strain using these slices and how it can be effectively visualised.

The first step taken to test the stated hypothesis of the research is to identify the procedures that can be used to process tMRI slices and implement it as a modular diagnostic tool that can produce a regional strain map. Such a standard pipeline procedure would minimise the need for a brand new solution with each development in the underlying technology. Organising the processing of the dataset into individual modules means that individual modules may then be changed or improved as desired or dictated by the changes in the tMRI technology and other clinical requirements. Using the literature review in Chapter 2, Chapter 3 fulfils the first research objective with the identification of the key

processes that the tMRI slices need to undergo in order to create the required regional strain model organising the procedure into a pipeline of software modules called the Strain Estimation Pipeline (SEP). The standard pipeline, or SEP, is identified in Chapter 3 making it possible to adapt to changes in the technology. The key to implementing a standard solution is to ensure that any changes made to the SEP can be validated properly and for this reason the plans for the implementation, evaluation and validation of the pipeline of modules, following which the remaining research objectives can be achieved, are also discussed here.

The next step to test the hypothesis would be to identify the methodology by which simulation can be used to validate the diagnostic tool. The difficulty in validating and quantifying the accuracy of the results of the SEP arises from the fact that the 3D motion of the LV is not known. The reasoning of the methodology is that if there is a model of the LV for which the 3D motion is already known, it is possible to compare the results of the SEP against this known 3D motion, to determine the accuracy of the SEP. To this end, tMRI slices are simulated for a mathematical model of the LV and used as input to validate the SEP. Chapter 4 discusses the implementation details of using simulation as the validation methodology. Details of the creation of the mathematical model to simulate tMRI are followed by how it is used to evaluate and refine the SEP and its constituent modules.

The next step towards testing the hypothesis is to use the identified simulation methodology to validate the diagnostic tool which is then used to process tMRI slices to produce the regional strain pattern of the acquired LV. Ideally, the final step to test the hypothesis of the thesis is to test the adaptability of the SEP to process tMRI slices that have been acquired using a different technique. Chapter 5 details the validation methodology and the simulation models that are used to test the achievable accuracy of the SEP along with the results of the methods used. This chapter also discusses the use of the validated SEP to process tMRI data.

The final chapter discusses the achieved results and the future direction in which the research can be taken. The figure 1.3 depicts the complete path of the research that is to be followed and discussed in this thesis.

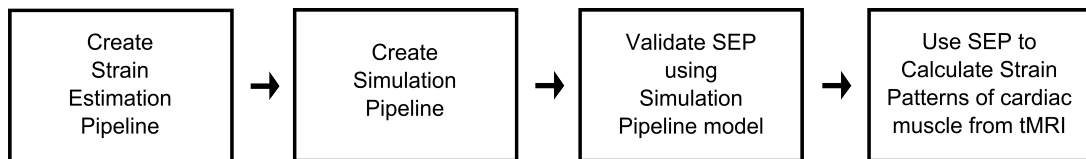


Figure 1.3: Research path

2

Regional Strain Model using tMRI

As introduced in the previous chapter, tMRI is used to capture image slices of the LV due to its suitability in estimating the regional motion of the tissue. This chapter further discusses tMRI and its challenges, as well as how the required regional strain model can best be represented. The first section elaborates the various available tMRI techniques along with their relative applicability and the problems faced in using tMRI to calculate the regional strain of an LV model. The subsequent sections discuss the acquisition of the tMRI dataset, how tMRI is set up for slice acquisition, how the tMRI dataset has been typically processed in past research, how the regional strain model is represented and how it is visualized.

2.1 tMRI techniques

As introduced in Chapter 1, tMRI induces temporary features in the tissue allowing for the observation and measurement of its motion and deformation. These induced features make the tissue motion more discernible and more importantly digitally detectable. There are a number of Radio Frequency (RF) pulse sequences that can be used to generate tag features in a tissue. A convenient classification of tissue tagging techniques is made by Ibrahim [Ibr11], based on the concept behind the motion decoding and the post-processing criterion used.

2.1.1 Basic tMRI techniques

The basic techniques generate a visible pattern of magnetisation saturation which do not require any post production for visual inspection of myocardial contractility. These techniques do, however, require post processing for the quantification of myocardial motion. The basic techniques started with the invention of tissue tagging by magnetisation saturation by Zerhouni [ZPR⁺88] and includes the other commonly used techniques of SPAMM [AD89b], DANTE [MS90] and CSPAMM [FM93]. Table 2.1 chronologically lists a number of basic tagging techniques with their advantages and disadvantages.

In the basic techniques, tissue tagging is done in two steps. In the initial set up step, a special sequence of RF pulses is applied, before acquiring the images, causing the suppression of the signal from the muscle tissue at finite intervals. This marks the tissue in evenly spaced, parallel planes. Next, a sequence of MR images is obtained in which the motion pattern of the saturated tissue is visible. The motion pattern in the image sequence can then be analysed for the motion of the tissue. Typical parameters for a SPAMM tagged acquisition are 32ms temporal resolution acquired in a 14 heartbeat breath-hold. Cine images are typically acquired over multiple cardiac cycles within a breath hold duration of 10-20s. Myocardial tags fade as a function of T1, which is on order of 850 ms. Therefore, myocardial tags are produced with each cardiac cycle in order to compensate for relaxation-induced fading.

2.1.2 Advanced tMRI techniques

The advanced techniques that were created in the second stage of development began in 1999 using the k-space of the images allowing for faster and more automatic analysis of myocardial motion. Advanced techniques, however, do not generate a visible tagging pattern.

The development of the advanced techniques started with the invention of HARP [OKMP99], DENSE [ADBW99] and SENC [OSAP01].

HARP analysis is based on the phase invariance property of tissue over time. The tissue phase is determined by the tagging preparation and thereafter remains constant, allowing tissue to be tracked by tracking regions of constant phase. The

2.1 tMRI techniques

Table 2.1: Basic tMRI techniques
adapted from [Ibr11]

Year	Technique	Advantages	Disadvantages
1988	Magnetization Saturation [ZPR ⁺ 88]	Simple idea	Low resolution, Long scan time, High SAR
1989	SPAMM [AD89b]	Low SAR available for clinical applications	Moderate resolution, 2D only, Tag fading
1990	Radial Tagging [BMZ90]	Suitable for measuring radial strain and heart rotation	low resolution for measuring circumferential strain
1990	DANTE [MS90]	High-density pattern of thin tags	Long tag preparation time
1992	Cine SPAMM [MA92]	Cine capability	Multiple breath-holds
1993	CSPAMM [FM93]	Improved tagging contrast, No tag fading	Double scan time as SPAMM
1994	Slice-Following(sf) CSPAMM [FMS ⁺ 94]	Tracks tissue through-plane motion	Lower SNR than CSPAMM
1996	Localized SPAMM [CY96]	Tagging confined to region of interest	Complicated tag preparation
1998	Variable-Density SPAMM [MB98]	Sensitive motion estimation	Long tag preparation time
1999	Singlebreath-Hold sf CSPAMM [SSF ⁺ 99]	High temporal resolution, Fast data acquisition	EPI may cause motion artefacts
2003	Ring Tagging [SLSB03]	Suitable for measuring circumferential strain	Low resolution for measuring radial strain

Table 2.2: Comparison of SPAMM tMRI techniques
adapted from [Ibr11]

Technique	Year	Advantages	Disadvantages
SPAMM [AD89b]	1989	Low SAR available for clinical applications	Moderate resolution, 2D only, Tag fading
Cine SPAMM [MA92]	1992	Cine capability	Multiple breath-holds
Localized SPAMM [CY96], [IS02]	1996, 2002	Tagging confined to region of interest	Complicated tag preparation
Variable-Density SPAMM [MB98], [IS03]	1998, 2003	Sensitive motion estimation	Long tag preparation time

Table 2.3: Comparison of CSPAMM tMRI techniques
adapted from [Ibr11]

Technique	Year	Advantages	Disadvantages
CSPAMM [FM93]	1993	Improved tagging contrast, No tag fading	Double scan time as SPAMM
Slice-Following(sf) CSPAMM [FMS ⁺ 94]	1994	Tracks tissue through-plane motion	Lower SNR than CSPAMM
Singlebreath-Hold sf CSPAMM [SSF ⁺ 99]	1999	High temporal resolution, Fast data acquisition	EPI may cause motion artefacts

original implementation of HARP is a two dimensional technique that used a higher order SPAMM acquisition rather than 1-1 SPAMM. Analysis using HARP takes just 2 minutes to produce strain at 48 points through 20 time frames when a similar analysis of SPAMM data using FindTags, the software developed by Guttman[GZM97] took an hour.

zHarp develops the original HARP technique to create a 3D model by using two CSPAMM datasets that are acquired over two breath-holds with tags in perpendicular directions, which have equal but opposite through-plane phase encoding. By using all of the resulting k-space peaks, HARP images for motion in x, y, z can be calculated. This technique is much faster than other 3D HARP methods as it does not require the acquisition of long-axis images and it also reduces the issue of registration errors inherent in building a 3D model from short and long-axis images acquired over multiple breath-holds.

Although HARP analysis is the most used of the advanced techniques it does have disadvantages. The main problem is that it is unable to measure the whole cardiac cycle due to tag fading (a problem that is shared by SENC and DENSE). The use of a k-space filter to isolate the spectral peak also results in greatly reduced spatial resolution. Table 2.4 chronologically lists a number of advanced tagging techniques with their advantages and disadvantages.

2.1.3 Challenges posed by tMRI

A brief comparison of the different MRI techniques that can be employed to detect the onset of CAD along with the requirement of measuring myocardial tissue function leads to the conclusion that tissue tagging is a good MRI technique to use in the investigation of cardiac function. However, tissue tagging techniques are still developing and vary vastly between themselves with the consequent, constant need for new software tools. This would imply that in order for a diagnostic tool that uses tissue tagging MRI to be relevant, there needs to be a defined methodology that can adapt to these changes and developments both rapidly and effectively, to meet the requirements of the evolving technology. There are a number of papers, including those by Axel [AMK05], Herzka [HM09] and Ibrahim [Ibr11], that have reviewed various emerging tMRI techniques but,

2.1 tMRI techniques

Table 2.4: Advanced tMRI Techniques
adapted from [Ibr11]

Year	Technique	Advantages	Disadvantages
1999	HARP [OKMP99]	Fast tag analysis	Phase errors, Low SNR
1999	DENSE [ADBW99]	High spatial resolution, Black-blood	Low SNR
1999	Fast-DENSE [ABW99]	Single breath-hold	EPI artefacts
2001	Meta-DENSE [AW01]	Higher SNR	Longer acquisition time
2001	SENC [OSAP01]	High resolution, Simple processing, Intuitive view	Low SNR
2003	Real-Time HARP [SDA ⁺ 03]	High temporal resolution	Complicated Setup
2004	DENSE With CANSEL [EG04]	Higher SNR, Less artefacts	Long scan time
2005	3D HARP [PPLO05]	3D strain analysis	Long tag analysis time
2005	zHarp [AEOPS07]	3D tissue tracking, Short scan time	Complicated data analysis
2006	Sf-SENC [FPSO06]	Through-plane tracking	Low SNR
2006	Fast-SENC [PSK ⁺ 06]	Real-Time imaging	Low resolution
2007	FastHarp [AESOP07]	Short data acquisition time - 25 frames per sec	Complicated setup
2007	Sf-Fast-SENC [ISF ⁺ 07]	Real-time imaging, Tissue tracking	Low resolution, Low SNR
2008	C-SENC [ISK ⁺ 07]	Strain and viability information in a single scan	No cine capability

Table 2.5: Comparison of HARP tMRI Techniques
adapted from [Ibr11]

Technique	Year	Advantages	Disadvantages
HARP [OKMP99]	1999	Fast tag analysis	Phase errors, Low SNR
Real-Time HARP [SDA ⁺ 03]	2003	High temporal resolution	Complicated Setup
3D HARP [PPLO05]	2005	3D strain analysis	Long tag analysis time
zHarp [AEOPS07]	2005	3D tissue tracking, Short scan time	Complicated data analysis
FastHarp [AESOP07]	2007	Short data acquisition time - 25 frames per sec	Complicated setup

Table 2.6: Comparison of DENSE tMRI Techniques
adapted from [Ibr11]

Technique	Year	Advantages	Disadvantages
DENSE [ADBW99]	1999	High spatial resolution, Black-blood	Low SNR
Fast-DENSE [ABW99]	1999	Single breath-hold	EPI artefacts
Meta-DENSE [AW01]	2001	Higher SNR	Longer acquisition time
DENSE With CANSEL [EG04]	2004	Higher SNR, Less artefacts	Long scan time

Table 2.7: Comparison of SENC tMRI Techniques
adapted from [Ibr11]

Technique	Year	Advantages	Disadvantages
SENC [OSAP01]	2001	High resolution, Simple processing, Intuitive view	Low SNR
Sf-SENC [FPSO06]	2006	Through-plane tracking	Low SNR
Fast-SENC [PSK+06]	2006	Real-Time imaging	Low resolution
Sf-Fast-SENC [ISF+07]	2007	Real-time imaging, Tissue tracking	Low resolution, Low SNR
C-SENC [ISK+07]	2008	Strain and viability information in a single scan	No cine capability

as can be clearly seen in tables 2.1 and 2.4, each tagging method has its relative advantages and disadvantages. In general the advanced techniques have the advantage of requiring less post-production but have the problem of low SNR. The basic techniques on the other hand require considerable manual post-production but can be visually inspected.

2.1.3.1 Physiology

In addition to the complex geometry and lack of visible landmarks, the heart also moves within the thoracic chamber making the use of MRI in cardiology complex. This motion has been termed as the ‘global’ motion of the heart and causes additional noise and occlusion by the surrounding organs. The global motion of organs within the thoracic chamber is caused by breathing and the heart walls are not always clearly distinguishable due to the proximity and movement of these organs.

The difficulty in obtaining an image of the heart due to the global motion is tackled in tMRI by the use of gating or the breath-hold technique. Typically several heart beats are required over a brief breath-hold, to gather enough data to form a high-resolution image sequence of the tag motion. The effectiveness of the gating technique largely depends on the accuracy of the patient’s breath-hold. Motion artefacts are known to be caused if the patient does not remain still, which may however be reduced with coaching. According to McVeigh [McV96], the position of the heart can be reproduced, for repeated breath-holds, with a precision of a few millimetres if the patient is coached. The images are typically acquired over multiple cardiac cycles within a breath-hold duration of 10-20s. Since heart motion is repetitive, this method of data acquisition is possible. Gating does, however, assume that the heart returns to the same position at diastole, although this may not always be accurate.

2.1.3.2 Image quality

Some of the properties that are used to define the quality of an MR image are the signal to noise ratio, the resolution or clarity of the image that can be acquired, the number of images that can be acquired per second and the number of images

that can be acquired per cm (of an axis). The two properties that are specific to tMRI slices are the number of tag planes that can be induced per cm (along an axis) and the life of a tag plane or the time duration during which a tag plane will remain visible.

The signal to noise ratio (SNR) is used in MRI to describe the relative contributions to a detected signal of the true signal and random superimposed signals ‘background noise’. The SNR will depend, in part, on the electrical properties of the tissue sample or patient being studied. Contrast to noise ratio (CNR) is the relationship of signal intensity differences between two regions, scaled to image noise. It is the difference in SNR between two relevant tissue types and can be thought of as the summary of SNR and contrast. Improving CNR increases perception of the distinct differences between two clinical areas of interest.

Due to the sinusoidal intensity profiles of the stripes produced in the original technique of SPAMM [AD89b] there is an overall decrease in the SNR of the image which affects the analysis of the myocardial 3D motion. Axel [AD89a] describes an improved version of SPAMM which substitutes more of the RF pulses with their relative amplitudes distributed according to the binomial sequence, resulting in sharper stripes. This technique significantly improves the quality of stripes and permits the use of SPAMM to produce a two dimensional grid of stripes. Thus tag patterns can be induced in a tissue either along a single axis creating a striped pattern or along two axes creating a grid-like pattern. However, as McVeigh [McV96] explains, it is more difficult to image a grid tag pattern than two images with orthogonal parallel line tagging patterns in a breath-hold because of its larger Fourier spectrum. Further research by Nguyen [NRDJ98] has improved the contrast of the images and has added flexibility of tag spacing, thickness and high resolution. A limiting factor in the fineness of the tagged pattern that can be imaged is the resolution of the imaging method, rather than the production of the tags themselves.

The resolution of the images that can be acquired is constantly improving as a result of advancing hardware technology, like increasing Tesla (magnetic field strength). This results in a higher clarity of images as can be understood from the details in Appendix A. Images acquired at 3 Tesla have increased SNR (103%)

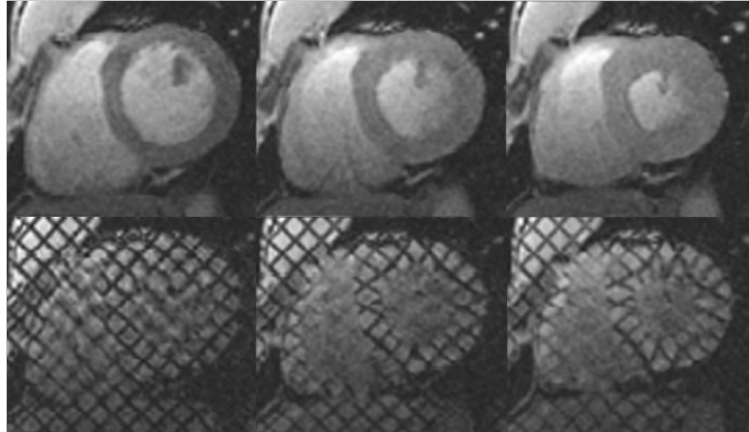


Figure 2.1: Sample of SPAMM tMRI fading over three time steps

and CNR (19%) with the increased myocardial T1 also resulting in increased tag persistence.

2.1.3.3 Fading of tags

As briefly mentioned before, the tags are not clearly visible in the tissue for the entire duration of the heart beat. Since the tags are only visible for approximately one second, the tags are created at the beginning of a heart beat and the image slices are acquired during systole and part of diastole. In other words, tracking the heart muscle is not possible for a complete heart cycle since the contrast between the tissue and the tags decreases considerably during the later phases of the cardiac cycle as seen in figure 2.1.

This is the problem that is the basis of a number of tagging techniques, including CSPAMM that effectively deals with the issue of fading but takes twice as long to scan. The time and the low rate at which radio frequency energy is absorbed by the body (SAR) makes SPAMM is still the most popular technique despite the complications caused by the fading of tags.

2.1.3.4 Through-plane motion of tags

Although it is easy to see the regional wall motion of the imaged tissue using basic tMRI techniques, it is not trivial to quantify the 3D motion due to what is

called ‘through-plane’ motion. The tag line that is visible on a slice is really the intersection of the RF induced tagged tissue, which is a plane, with the (normally perpendicular) plane on which the slice is acquired.

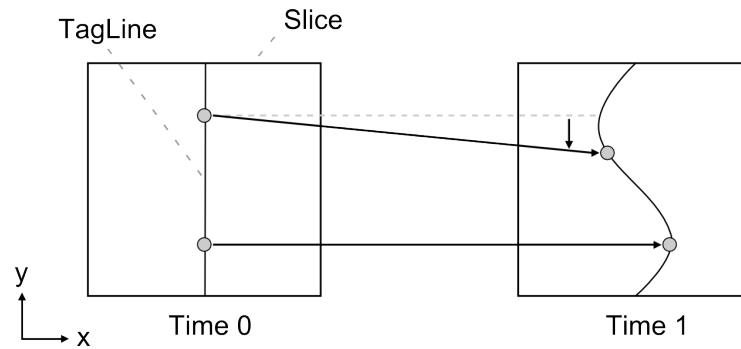


Figure 2.2: 2D motion of points within a tag line

The concept is more clear in figure 2.2 where a 2D view clearly shows the motion of the points in the x direction but shows how there is no accurate way to see if the points have moved in the y direction or along the line.

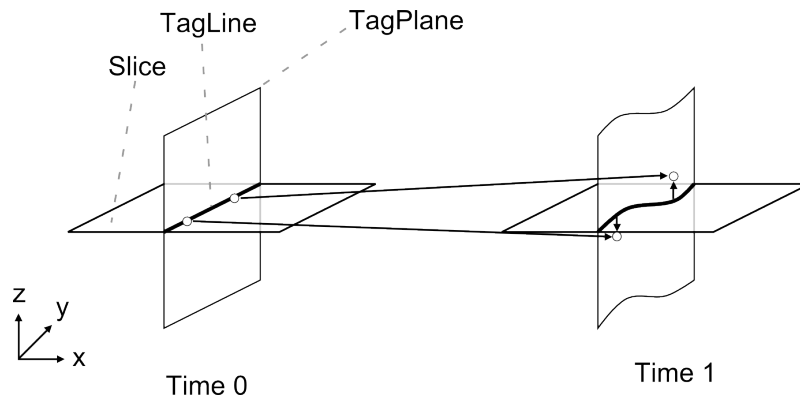


Figure 2.3: 3D motion of points within a tag plane

Figure 2.3 shows the complexity of the 3D case where the motion of a point in the volume cannot be quantified without further information. The motion of the points in the x direction can be clearly seen but shows how there is no accurate way to see if the points have moved in the y direction, along the line, or in the

z direction, through the plane. This means that the visible tag lines in a slice sequence may not represent the same physical points within the tissue due to the ‘through-plane’ motion.

Slice following techniques have been proposed to deal with this problem and work by saturating slices either side of the tagged slice of interest and increasing the imaging slice thickness so that it encompasses the tagged slice at the extremes of its motion.

2.1.3.5 Data acquisition

The pursuit for the required tMRI data began locally, at the Castle Hill hospital. After the initial step of convincing Cardiologists of the usefulness of the tMRI technology came the task of convincing the Radiologists that acquire the dataset. Although tMRI as a technique is gaining popularity among the research community and tissue can be tagged with currently available machines, its use was not seen as necessary by local Radiologists. Not fully convinced of its usefulness or requirement the dataset was acquired while a patient was waiting for the Gadolinium to circulate before the session for the Delayed-Enhancement images to be acquired. However, the acquired dataset was not complete and did not meet the requirement of being acquired along the Long Axis as well as the Short Axis. After further attempts to acquire data locally came up with similar results, the national and international experts in the field of tMRI including those from Johns Hopkins University and Pennsylvania State University were contacted in the hope of receiving advice on how to obtain a usable dataset. UK universities in possession of suitable datasets were unable to share the datasets citing ethical issues in their agreements to store and use patient data. However, two tMRI datasets were received from UCLA (Elliot McVeigh) and from the Cardiac Atlas Project submitted from a hospital in Auckland, New Zealand (Alistair Young) as part of a Motion Tracking challenge dataset for a 2011 MICCAI workshop.

2.2 Capturing a tMRI slice

The two stages in the capture of a tMRI slice are the tagging of the tissue with the RF pulse sequence, followed by the acquisition of the image slices over time. A number of decisions need to be made before capturing a tMRI slice. The first step is to identify the chamber of interest. Following this decision the coordinate systems of the RF induced tag planes and the slice acquisition that allow for the 3D reconstruction of the motion is decided. This decision is based on the tagging pattern (grid or lines) to be induced in the tissue and the chamber of interest. Finally, before image slices of the tagged tissue can be acquired, decisions need to be made on the distance between the slices and the number of phases to be acquired.

The first section briefly discusses the basis on which the LV is decided upon as the chamber of interest. This is followed by a description of the coordinate systems used when inducing tag planes in the tissue and when the slices are acquired from which the 3D motion is to be estimated.

2.2.1 Ventricle of interest

The decision of which heart ventricle is analysed is dictated by the complexities involved in tracking the RV and relative importance of the LV in diagnosing disease. The complexity in tracking the RV arises from the fact that its muscle walls are relatively thin, with fewer available tag lines from which to reconstruct motion. Work by [HMA00b] found that the RV exhibits significant motion (greater than 10 mm) through two or more consecutive image slices. Additionally, the RV also has a more complex geometry to model as can be seen in figure 1.1 in Chapter 1.

Although the analysis of the RV may hold information, since the LV is the largest chamber of the heart with the thickest myocardium, from a diagnostic point of view the analysis of the LV motion is the most important.

2.2.2 Coordinate systems for RF induced tag planes

The motion of any point in 3D space can be completely described by the specified coordinates of any 3D coordinate system with mutually orthogonal axes. The

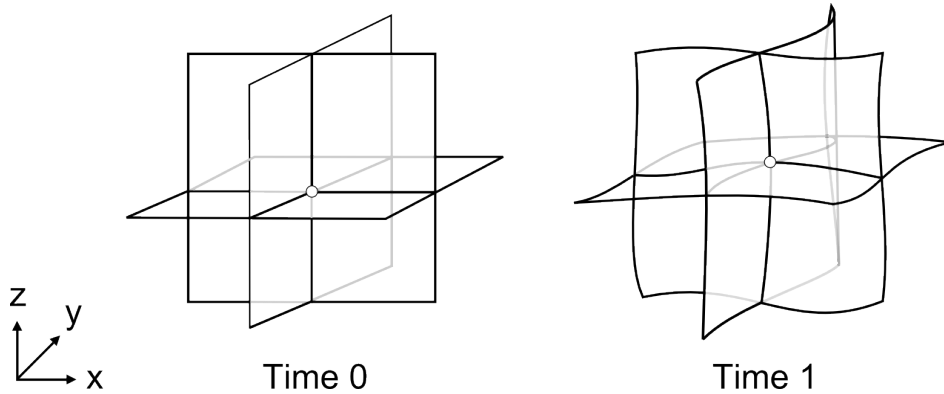


Figure 2.4: Tag grid motion (3D)

through-plane motion of the tags mean that complete displacement cannot be quantified with the use of tag lines in a single direction. In order to describe the complete motion of the LV, the tissue needs to be tagged in three mutually orthogonal directions as in figure 2.4.

2.2.3 Coordinate systems for tMRI slice acquisition

The tMRI slices need to be acquired within a coordinate system having 3 orthogonal axes to enable the reconstruction of the complete motion. The research generally uses a Cartesian coordinate system to induce tags in the tissue and acquire the tMRI slices in a polar coordinate system. Polar acquisition of MR slices is the chosen mode by the researchers since it provides more uniform motion information through the volume. Thus, the tag planes are induced in the myocardial tissue using a Cartesian coordinate system and the image slices are acquired following a polar coordinate system.

In general an axis, called the Long Axis (LA), is defined to run along the centre of the LV volume passing through the base of chamber as shown in figure 2.5. The short axes (SA) are then defined to be mutually perpendicular and

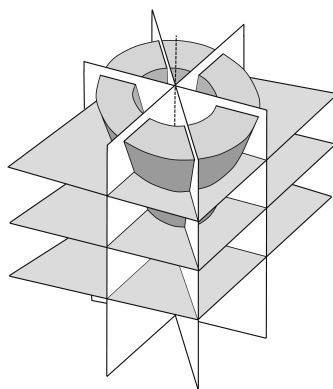


Figure 2.5: Planes of slice acquisition for LV
adapted from [HMA98]

on a plane that is perpendicular to the LA. LA slices are those slices that are acquired as rotations about the LA, while SA slices are defined as those that show movement along the SA at various distances along the LA, as shown in figure 2.5. In other words, the SA slices show the tag lines that are a result of the image plane intersecting the tag planes that are initialised perpendicular to SA and parallel to the LA. On the other hand, the LA slices capture the intersection of the tag planes that are induced to be perpendicular to it and parallel to the SA. The SA slices may show two sets of tag planes in perpendicular directions on the same plane. Thus, the SA image slices are perpendicular to the LA and shows the set of tag planes that are perpendicular to it, while the LA slice is orthogonal to the two SA slices and shows the set of tag planes that are perpendicular to the SA slices.

2.2.4 Distance between slices & number of slices

Due to the physical constraints of the tMRI techniques and MRI machines, the distance between consecutive SA slices is commonly around 6mm but tends to be between 5 - 8mm. A SA stack has between 6 and 9 slices and LA image slices are acquired at angle of 30° - 40° between consecutive slices. The number of phases acquired varies from 10-20.

Table 2.8: Details of acquired dataset

Property	UCLA	Cardiac Atlas Project
Tag pattern	Line	Grid (7x7mm)
Slice Thickness	5mm	8mm
Frames	18	25
SA Positions	4	3
LA Positions	none	4
Resolution	192 x 144	256 x 208
Machine	Siemens Avanto (1.5T)	Siemens Symphony (1.5T)
TR	32.1, 32.6 ms	46 ms
TE	3.52, 3.59 ms	4 ms
Flip Angle	15°	10°
Sequence	True fast imaging with steady state free precession	Unknown

2.2.5 Acquired tMRI dataset

Since the UCLA dataset had only SA slices, it is the Cardiac Atlas Project dataset that is used. The tMRI dataset from the Cardiac Atlas Project acquires a slice at three SA locations and four LA locations over 25 time steps or frames making the complete acquired dataset a total of 175 slices. The slices are tagged using SPAMM and as mentioned earlier the dataset was made publicly available as part of a motion tracking challenge for a conference. Details of the two acquired datasets can be seen in 2.8.

2.3 Representing the data

As mentioned before, from a diagnostic point of view the analysis of the LV is important due to its chamber size and the myocardial thickness relative to that of the RV. Additionally, the regional motion of the RV has been more difficult to track due to the more complex motion of its muscle walls. As a result, the

research generally focuses on the LV but a few like Guttman [GZM97] and Yeon [YRT⁺01] have modelled the RV.

The representation of the data can be split into the representation of the geometric model and that of the tag planes. The geometric model is a representation of the LV chamber volume with knowledge of the material behaviour of the muscle while the tag lines are a representation of the tagged tissue planes with knowledge of its motion. Combining these two representations we can estimate the motion of the geometric volume and its regional strain pattern.

2.3.1 Geometric model

Several of the most relevant ideas are the finite element models that incorporate spring-like interconnections and nonlinear basis functions, locally deformable superquadrics [PMA95], b-snake interpolation [ACC⁺98], high order polynomial fitting of the sparse tag points [OMH⁺95], and an estimation theory based idea which uses a stochastic vector field to assist in the interpolation [DP94]. The more recent use of iso-surfaces and quadric surfaces is seen nicely in the research by Park [PMMA05], where the LV is modelled with an iso-surface formed by b-splines using prolate spheroidal coordinates. In order to model the entire heart, they use blending of deformable primitives, described by cutting surfaces apart and gluing them together. Blending starts with 2 underlying shapes, which are then mapped into a new domain.

The work by Haber [HMA00b] models both ventricles by the generation of a volumetric finite element mesh based on contour information from the images. The mesh is the starting point for recovering the 3D motion from the MRI images. A common approach taken to model the heart ventricle is using quadric surfaces. By nature, b-splines try to create smooth curves, which would imply that the motion of the muscle wall is smooth and uniform. This is reasonable when the muscle wall tissue is uniform in material properties and is moving normally. The key is that it is only the surface that is represented and not the thickness of the muscle or ventricular volume.

The use of the FEM method is better suited to the task of creating a motion model of a possibly heterogeneous volume since each element can have different

material properties.

2.3.2 Tag lines

B-splines are commonly used to represent tag lines due to its several advantages including the compact representation, parametric continuity and the ability to control local shape. B-splines can describe the displacement of the tag lines and depict the deformations of the image plane, the volume and the space-time continuum. Amini [ACC⁺98] uses coupled b-spline grids to track tag deformations, efficiently reconstructing displacements from SPAMM grids. Ozturk [OM99] captures the motion of the heart using a 4D tensor product of b-splines on tMRI.

Active contours are the other commonly used method of representing tags due to its advantages of immediate generation of tag surfaces, subpixel accuracy of tag line localisation, parametric continuity and the ability to determine the location of a complete tag surface by assigning the location of a few control points.

2.4 Processing the tMRI

The analysis and conversion of the sequence of tMRI slice stacks into the useful stress and strain information can be split into a number of modules that can be applied to the dataset. The dataset would need to be processed in sequence to provide meaningful results.

The main stages of analysis of tagged images as outlined by Axel are image preparation, boundary surface extraction (segmentation), tag tracking and 3D motion reconstruction.

Due to the poor quality of the tMRI slices it is often required that the images are enhanced before they can be accurately analysed. Further, using an enhancement technique on an image may also result in a form that is more suitable for analysis. The techniques used for enhancement may be divided into two broad categories based on the domain in which they operate. The spatial domain of an image is the space in which processing involves the direct manipulation of its pixels. Techniques that work in this domain manipulate and change an image that represents an object in space to enhance the image for a given application.

Among the most basic techniques are the application of various filters and masks as well as more complex segmentation techniques like thresholding, edge detection and region growing methods. In contrast, the frequency domain is the space in which the values of each image position represents the amount that the intensity varies over a specific distance in the spatial domain. High frequencies correspond to pixel values that change rapidly across the image while strong low frequency components correspond to large scale features in the image. Frequency domain based image processing techniques thus modify the spectral transform of an image. In order to work on an image in the frequency domain, the image is first converted to its frequency representation after which the appropriate image processing technique can be applied, following which the inverse is computed to transform the image back into the spatial domain. The reason that these techniques are of interest is that some image processing operators are more efficient or only practical when applied in the frequency domain. A good reason that a tMRI slice may be suitable for such processing in the frequency domain is that the sinusoidal nature of the tag patterns can be exploited.

2.4.1 Image preparation

Image preparation typically involves three principal steps. The first and second steps involve the suppression of noise. The first is the suppression of background intensity variation that is caused by non-uniform RF fields and the second is the suppression of thermal noise. The final step is the normalization of image intensities.

Although there are a number of methods that are used for MRI data to suppress background intensity variation, a method specifically tailored for tMRI was developed by Montillo [MAM03]. There are a few approaches when dealing with the suppression of thermal noise in MR images with some methods, like Saha [SU01] targeting noise suppression in isolation, while others like Montillo [MUAM03] combine the suppression of background intensity variation with noise suppression for convenience.

One of the challenges with analysing MR images is that the same tissue can vary in nominal intensity from one subject to the next and even for the same

subject upon repeated scans. Research on an intensity normalization method has resulted in the successful adaptation by Montillo [MAM03] of a histogram modification method previously used on brain MRI by Nyul [NUZ00].

2.4.2 Boundary surface extraction and tag tracking

The segmentation of a slice is the identification of areas that are of interest in an image, which in this case are the boundaries of the LV wall (endocardial and epicardial surfaces) and the tag lines. This is especially challenging from tMRI slices for several reasons. One of the main problems is the artefacts and noise in the slices. Additionally, the tag lines interfere with boundary detection and the initialization of boundary surfaces is difficult. This difficulty arises from the complexity of heart geometry as well as the limitation in the acquisition of the slices capturing the volume of the heart with gaps and the non-uniform spacing between image planes. When considering the segmentation of the wall boundaries and the tag lines, the more laborious and time-consuming is the extraction of the boundaries.

Two of the general problems with segmentation are the time it takes and the expertise required for accurate results. Although historically it is a task that has exploited a trained expert for accurate results, it is possible for the process to be automated to reduce the time taken. Since automatic segmentation comes at the expense of accuracy, a balance is achieved by the use of semi-automatic segmentation, where the human expert can guide the segmentation process. This is normally done by marking the region of interest or by indicating points from which to start the automatic segmentation.

Soon after the emergence of tMRI for cardiology, semi-automated techniques were investigated to avoid the length of time involved in manual segmentation solution. Early techniques, like Kumar [KG94], Kraitchman [KYCA95] and Young [YKDA95], adapted active contour models to detect and track the tag lines of the dataset. Active contours or snakes suit interactive shape editing well, since they are computed rapidly and allow great flexibility in defining energy terms. The problem encountered when segmenting tMRI slices with active contours is that the many local minima caused by the tag lines makes distinguishing the

edges of the wall contours difficult. Despite the required intervention to overcome getting stuck in the numerous local minima, the overall results of using these semi-automatic techniques were good with Kraitchman [KYCA95] achieving a twelve fold reduction in time compared against manual segmentation. A fully manual segmentation of 5 slices at 5 time points, took as long as 5 hours to analyse in comparison to less than 25 minutes with the semi-automatic segmentation approach.

The main source of errors in these semi-automated methods is found in tag placement when the centre of a tag may lie in between 2 pixels. Additionally, as expected, the fading of the tags causes increased errors in tag detection towards the end of systole. However, in terms of achievable accuracy it was found that the semi-automated techniques provide results that are comparable to manual segmentation with the advantage of the considerable reduction in time taken. Some of the early techniques were further developed to create software packages like ‘SPAMMVU’ [AGB92] and ‘FindTags’ [GZM97]. However, due to the complexities involved, lots of researchers like Park [PMYA96], Young [You99] and Ozturk [OM99], Haber [HMA00a] and Park [PMA03] have continued to use manual segmentation focussing on other aspects of the research area despite the time costs.

In the past decade, fully automated techniques have been more successful in the processing of tMRI by using filters to remove the tags and facilitate an easier extraction of the myocardial boundaries. Montillo [MMA02] used shape similarity and a gradient flow snake to automatically isolate the blood volume, the epicardium and endocardium of the LV and RV and this was further developed into another fully automated, deformable model based method by Montillo [MMA03] to create a surface model of the walls of the RV and LV. The different methods have achieved results with varying accuracy based on slice positions. While the filter matching techniques tend to be relatively robust with respect to dealing with the fading of tags, a limitation of all tag line tracking methods is that temporal correspondences are available only for pixels along the tag lines and not for the pixels in between them.

2.4.3 Tag tracking and motion estimation operating in the frequency domain

Analysing the tMRI slice in the frequency domain allowed Gupta[GPAT97] to develop a fully automated optical flow method as detailed in section 2.4.4.2. Despite the advantage of automatic processing, as with all optical flow algorithms, the problem of brightness changes, that isn't caused by motion acting as noise, still remains. Processing tMRI in the frequency domain also allows to circumvent the problem of intensity discontinuity in the slices. As mentioned before, one of the problems faced when tMRI images are semi-automatically segmented is the discontinuity in the intensity of the chamber edges or local minimas in the gradient changes caused by the tag lines. This problem is effectively dealt with by processing the image in the frequency domain with Gabor filters to remove the tags from the slices. These filters have been successfully used by Montillo [MAM04] to automatically extract the tag lines from tMRI, while Qian [QMA06] uses a tunable 3D Gabor filter bank to extract the tag lines and track displacement.

Another analysis technique that uses the frequency domain is the sinusoidal analysis of the tMRI slices. The early method by Zhang [ZDY⁺96] used Fourier based frequency and phase information to separately track horizontal and vertical tag lines. A variation was developed by Clarysse [CBK⁺00] that tracked myocardial displacement by using cosine series model that successfully fitted the entire tMRI dataset. In Arts [APD⁺10] the image intensity in the environment of each pixel was modelled as a moving sine wavefront and the displacement is estimated at subpixel accuracy. The principle of sinusoidal analysis is to analyse the data into different frequency components. The algorithms model the environment of a pixel as part of a sine wave with local frequency and amplitude. Although these algorithms have shown results of high accuracy and a reduced sensitivity to noise, the data analysis is complicated.

2.4.4 Motion estimation of myocardium operating in the spatial domain

Research of RV wall motion by Haber, documented in [HMA98] and [HMA00b], have shown that there is considerable through-plane motion of the induced tags in SA and LA slices making it difficult to track its regional motion. In contrast, LV motion is easier to investigate due to its relative thickness and consequently easier to identify its abnormal regional motion. The normal motion of the LV is known to be twisting and contracting towards the centre of the chamber volume as well as up from the apex towards the base. Thus, any motion estimation approach will need the capacity to identify 3D motion in order to fully investigate the motion of the LV.

Using a stack of tMRI slices acquired over the entire duration of a heart beat captures the motion of the set of tag lines which can be used to estimate regional wall motion and subsequently calculate the regional stress and strain of the walls in that time. However, due to the through-plane motion of the tags, two points that appear to correspond on a given tag line at different times in the slice stack may not represent the same physical point within the tissue as shown in figures 2.3 and 2.2. As a result, complete motion information cannot be extracted from the slice sequence along a single axis but instead must be estimated based on tMRI slice sequences along orthogonal planes.

As can be seen in table 2.9, there are numerous motion reconstruction algorithms and a number of ways to classify the various algorithms based on the core principle of the approach taken. In order to discuss the various algorithms, they have been classified based on the domain of operation since images can be digitally processed in either the spatial or the frequency domain. Classification of the various algorithms based on the domain of operation is simple and straightforward, allowing for algorithms that combine different tracking and motion estimation approaches.

The three main motion estimation approaches that have been used when processing tMRI slices in the spatial domain are based on segmentation, optical flow and non-rigid registration. The segmentation based approach results in manual to semi-automated methods that require varying degrees of human intervention.

Table 2.9: Estimating Motion

Reference	tMRI Technique	Motion Estimation Technique
[MOMZ92]	SPAMM	Segmentation, with contours and Thin plate splines
[YAD ⁺ 93]	SPAMM	FEM, vtp grids to model tag planes
[OMH ⁺ 95]	SPAMM	Displacement field fitting
[DJP95]	SPAMM	Tag lines
[DJM97]	SPAMM	Displacement field fitting <i>dense mesh points</i>
[ACC ⁺ 98]	SPAMM	VTP grids
[HMA98]	SPAMM	Tag lines
[KP98]	SPAMM	Thin plate splines of intersection, VTP grids, without contours
[CMJ99]	SPAMM	Tag lines
[HADRA99]	SPAMM	Fits time-varying B-splines
[KMG ⁺ 00]	SPAMM	1D displacement field for the z-component
[ACER01]	SPAMM	3D B-splines track the tag lines from 2 sets of orthogonal tMRI views
[WCA01]	SPAMM	Multidimensional interpolation to reconstruct dense displacement fields
[HMA03]	SPAMM	FEM and statistical methods
[TDRA03]	SPAMM	Tagline intersections
[DDJ04] & [DDJ05]	SPAMM	3D deformation model is fitted directly to the tMRI dataset
[PMMA05]	SPAMM	Non-linear fem theory
[QMA06]	SPAMM	Tunable 3D Gabor filter bank to automatically extract tag lines and - track displacement
[FvA10]	CSPAMM	Multi-scale algorithm that uses local scale selection
[PM92]	HARP	Variable Brightness Optical Flow (VBOF)
[GPAT97]	HARP	Optical flow method
[APD ⁺ 10]	HARP	Sine wave with local frequency and amplitude
[CHBS ⁺ 10]	HARP	Variational optical flow

Although there are large numbers of segmentation based methods, tag tracking methods based on optical flow and non-rigid registration makes it possible to develop a fully automated motion reconstruction method. The methods based on optical flow allow for semi-automated and fully automated motion reconstruction solution while following a non-rigid registration tag tracking approach results in a fully automated motion reconstruction method.

2.4.4.1 Non-rigid registration methods

Non-rigid registration methods are used to process tMRI slices by matching corresponding tagged regions in the tMRI slice sequence by measuring the similarity between slices. There are a number of statistical techniques that are used by non-rigid registration techniques to measure the similarity. For instance, Petitjean [PRP⁺03] and Rougon [RPP⁺05] use a generalised information-theoretic metric called exclusive f-information as a measure of similarity of the slices. Registration is achieved by optimizing a cost function that measures the similarity between two slices as well as the smoothness of the deformation as found in Chandrashekhara [CMR04] and Ledesma-Carbayo [LCBSM⁺06].

Despite the possibility of automation of the non-rigid registration techniques by Chandrashekhara [CMR04] and Rougon [RPP⁺05], a required step is the segmentation of the myocardium. This is normally done manually in order to define the area of interest and ensure that the other parts of the body are not considered during the registration process to obtain more accurate results as well as reduce computation time. Another challenge when applying non-rigid registration with tMRI slices is that the intensity values of the tissue are not constant in tMRI. Most techniques assume that the intensity of the tissues remain constant through time despite the known deprecation of the slices through time.

2.4.4.2 Optical flow methods

Optical flow based methods are based on the classical method described in Horn [HS81], which estimates a velocity vector for each point in a scene given images of the scene at two or more different times. The basis for the optical flow technique in tMRI is the brightness constraint equation. It involves estimating the

spatial gradient of the intensity image, using finite differences of the intensities at neighbouring pixels, as well as a temporal intensity derivative which is estimated by subtracting the intensity at a pixel from one time-frame to the next in a cine acquisition.

In the early research of analysing tMRI using optical flow based methods, researchers like Denney [DP94] assumed that the time derivative of the brightness of a myocardial pixel was zero. However, since the brightness of a tMRI pixel may vary significantly due to tag fading and through-plane motion, researchers like Prince [PM92] and Dougherty [DAB⁺99] chose to deal with these problems with different strategies and to differing effect. Prince [PM92] developed the variable brightness optical flow method to model and compensate for the decay in tag pattern brightness based on MRI physics while Dougherty [DAB⁺99] developed an optical flow method that allowed for the rapid estimation of the myocardial displacement from tMRI by pre-processing the slices to suppress the effects of tag fading.

As briefly mentioned earlier, Gupta [GPAT97] developed a fully automated optical flow method that exploits the sinusoidal nature of the tag patterns by analysing the image in the frequency domain. By extracting directional sub-band images from the tMRI data and formulating constraint equations for each of the sub-band images, the system of equations are solved using least squares pseudo-inversion. Since there is no explicit regularisation the method prevents excessive smoothing across boundaries which is a common problem in standard optical flow algorithms.

The advantage of optical flow methods is the reduced processing time and the possibility for automatic processing. However, a problem with optical flow motion estimation algorithms is that phenomena other than motion can cause spurious brightness changes which violate the underlying brightness constancy assumption.

2.4.4.3 Segmentation based methods

Segmentation based methods typically begin by having a user manually identify the location of the tags in each imaged slice location at end diastole. Most

motion estimation methods based on segmentation construct virtual orthogonal tag planes from the segmented tag lines of tMRI stacks. These virtual tag planes are then used to estimate regional motion throughout the volume of the required chamber. The main problem facing these methods of estimation is the combining of information from the different image plane sets. It is only at the intersections of the imaged tissue slices (called material markers) that all motion components can be measured. Thus, reconstruction of the 3D motion is usually based upon interpolation between the points where 1D or 2D motion has been measured.

Following a segmentation approach has the advantage of being intuitive along with parametric continuity in the model representation and the control of the curve shape. However these methods do pose the problem of long processing times.

2.4.5 Segmentation based motion estimation methods

The main estimation approaches that are followed use thin-plate splines, displacement field fitting and a finite element method. The segmentation based motion estimation methods can also be classified based on the amount of the tag profile used when calculating the motion of the chamber as using the tag intersection or the entire tag line profile.

2.4.5.1 Estimation using tag line intersections

Methods of motion estimation that use tag line intersections work by reconstructing the 3D myocardial motion based on the interpolation between the tag line intersections that are called material points where motion can be measured.

One of the earliest algorithms developed using this approach was by Moore [MOMZ92] which involved tracking the set of discrete material points where the tag lines intersect the inner and outer boundaries of the myocardium. The problems associated with this method are the resulting sparse material markers dataset and that the accuracy relies on the accuracy of the myocardial boundary detection. These issues were successfully addressed by Kerwin [KP98], producing a comparatively denser array of material markers that did not rely on myocardial boundary detection. In this method the material markers are located at the

intersection of the three orthogonal tag surfaces. Since the intersection of the tag planes are not imaged, the material markers are calculated from the grid of virtual tag planes that are reconstructed using the 2D tag line information from multiple slices. Kerwin [KP98] validated the method by implanting markers that showed that highly accurate, sparse motion estimates are sufficient to estimate the motion of the myocardium and in some cases are preferable to dense ones.

The multiple intersecting tag planes are either generated by imposing a tag-grid pattern in a single acquisition, which can be done for 2D grid patterns, or by tagging along different planes in separate acquisitions and using the virtual tagged planes to create a grid as done in Young [YKDA95], Amini [ACC⁺98] and Kerwin [KP98]. Although Young [YKDA95] gave extra importance to the intersection points of the tag grid, the remainder of the tag line was also used when estimating the motion of the volume. The reason Kerwin [KP98] is special is that the material markers generated and used in the motion estimation algorithm were 3D intersections instead of 2D intersections. The key idea is to generate material markers at the intersection points of all three virtual tagged planes which are then used as the features for the overall motion estimation, as can be seen clearly in figure 2.6.

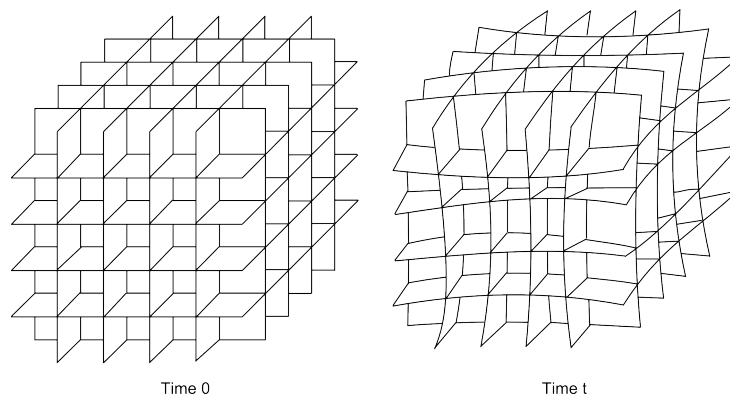


Figure 2.6: Motion estimation by reconstruction of Virtual Tag Planes

Park [PMYA96] used tag line intersections to guide the deformation of the model by applying corresponding forces.

In contrast, Amini [ACC⁺98] used 2D tag intersections as control points for the B-snake and thin-plate splines for the final direction. The Amini [ACC⁺98] research was further developed by Wang [WCA01], requiring multidimensional interpolation to reconstruct dense displacement fields. The displacement estimation was formulated as a variational problem and the solution was projected on spline subspaces. Numerical methods derived based on b-spline properties allowed the fast execution of the algorithm achieving faster computational times.

2.4.5.2 Estimation using tag lines

The motion estimation methods that use the entire tag line for the reconstruction of the chamber deformation are used by many researchers since it provides partial information in regions where there are few intersections making it more robust to noise than using the intersections alone. This approach is especially useful for the relatively thin walled RV, where the likelihood of having regularly spaced intersections is low.

O'Dell [OMH⁺95] were among the early researchers to use the position and displacement information along the entire length of each tag to reconstruct the motion of the LV. This approach eliminates the need for accurate simultaneous measurement of displacement in two dimensions and permits computation of the 3D deformation gradient tensor at any point in the heart wall. Denney [DJP95], Croisille [CMJ99] and Amini [ACER01] are among the researchers that used the O'Dell [OMH⁺95] approach of using the entire tag line for the motion estimation. Like O'Dell [OMH⁺95], Huang [HADRA99] takes the tag lines from all the image sequences however, unlike O'Dell [OMH⁺95], Huang [HADRA99] fits time-varying b-splines to the data. The advantage of this technique is that the tag surface reconstruction, 3D material point localisation and displacement assessment are performed in one step. Ozturk [OM00] develops on this and captures the motion of the heart using a 4D tensor product of b-splines on tMRI. The advantages that using b-splines provides includes the capacity to use all available tag line data, the compact representation and the calculated deformation being continuous in space and time.

Haber [HMA98] on the other hand developed the tag line intersection method by Park [PMYA96], using the entire tag line to influence the deformation of the LV model. This was modified further by Haber [HMA00a] to have the entire tag surface constrain and influence the deformation of an RV model. This was especially suited for the reconstruction of the RV motion since the motion is known to be through two slices.

2.4.5.3 Thin-plate splines

Thin-plate splines have been widely used as the non-rigid transformation model in image alignment and shape matching with the physical analogy from the bending of a thin sheet of metal. In tMRI processing, the deformation of the tissue in the direction that is orthogonal to the slice is modelled with thin-plate splines to depict through-plane motion. This makes thin-plate splines ideally suited to estimate the motion of tag line intersections.

An early motion estimation algorithm that used thin-plate splines was developed by Moore [MOMZ92], tracking the set of discrete material points, where tags intersect the inner and outer myocardial boundaries, with the use of one-dimensional splines. The later motion estimation method used by Kerwin [KP98] tracked the points located at the intersection of three tag surfaces that are within the myocardium of the LV and estimated their motion using a thin-plate spline. In both methods the markers were used to compute the average strain tensors within volumes delineated by the markers. However, Kerwin [KP98] produced a denser array of material markers without relying on myocardial boundary detection, which is typically much less accurate than tag detection.

Thin-plate splines are widely used for a number of reasons that include the smoothness of the interpolation and that it is invariant under rotations and translations. The reasons that Kerwin [KP98] choose this method included the expectation that the minimum bending energy property of thin-plate splines is likely to reflect the physical characteristics of LV contraction. In addition, thin-plate splines can be used with the irregular sampling patterns of tag line data, it does not require boundary conditions and it has the desirable characteristic of being continuously differentiable.

2.4.5.4 Displacement field fitting

Displacement field fitting is a method to estimate the values of a parameter throughout a region, given a set of measurements of the parameter in and around that region. This is the approach taken by O'Dell [OMH⁺95] to calculate myocardial motion. In this early algorithm the displacement data for each directional component is measured independently of the other directions and each individual displacement component is then used to compute the 3D displacement of any point in the deformed heart wall. As identified by Denney [DJM97], a drawback of the early displacement field fitting techniques was the reliance of the strain map computation on the chosen coordinate system. This was dealt with by Denney [DJM97] by constructing a high resolution displacement field from a dense mesh of points and using finite difference analysis on this mesh of points with a smoothness constraint that minimizes the spatial variation of displacement across the myocardium. The strain map that is then calculated is independent of any a priori displacement or deformation models. An added advantage of this algorithm is that the resulting fit accuracy is not dependent on the coordinate system used for the reconstruction.

An inherent disadvantage of a displacement field fit is the requirement of regularisation for a stable solution because the data is measured in a limited number of image planes. As a result, Kuijer [KMG⁺00], uses the CSPAMM imaging technique of slice following by Fischer [FMS⁺94] to detect SA motion components. These results are combined with a 1D displacement field for the z-component without the need for additional regularisation or smoothing in the circumferential direction and preserving the true spatial resolution of the measured data. A number of researchers since Kuijer [KMG⁺00], like Russel [RTK⁺09], use the method to reconstruct 3D displacement. Although displacement field fitting methods have the advantage of more automatic processing, the required processing takes a long time.

The approach taken by Tustison [TADRA02] uses b-splines to efficiently implement displacement field fitting, where the problem is solved as a 4D problem making the motion reconstruction simply a difference between the two constructed solids. Research by Deng [DDJ04] found that b-spline models based

on a cylindrical coordinate system was better suited to the morphology of the myocardium and resulted in more close fits than previously proposed Cartesian b-spline models. Although the method cannot reconstruct deformation between imaged phases, it can reconstruct the deformation at a single time frame without having to process the entire data set. In addition, the technique does not require explicit regularisation. The other approaches to implement displacement field fitting are the finite element method used by Young([YKDA95] and [YFA96]), the prolate spheroidal model used by O'Dell [OMH⁺95] and the discrete model used by Denney [DJM97].

2.4.5.5 Finite element methods

Finite element method is a numerical technique for finding approximate solutions, which is an extension of the idea that many tiny lines can approximate a large circle by dividing a large object into smaller elements. This involves solving for many simple equations over many small subdomains, named finite elements, to approximate a more complex equation over a larger domain.

All the algorithms that use finite element methods to process tMRI slices begin with the creation of a basic FEM at the initial time using the extracted myocardial boundaries. The deformation of the model on the other hand have been reconstructed by following different approaches. Algorithms by Park [PMYA96] and Haber [HMA98] apply force on the FEM nodes towards material points which are the reconstructed tag intersection, resulting in the deformation of the model. The estimation process used by Park [PMMA05] and Haber([HMA00b] and [HMA00a]) take it further and apply the force on the FEM nodes to move towards reconstructed tag surfaces allowing for more motion information and constraints to influence the solution. Another approach was taken by Young [You99] which tracks the motion of the tag planes by modelling the tag surfaces as material surfaces within the FEM thus creating the deformation using the material properties of the tag planes to constrain the forces acting on the FEM nodes.

Finite element methods have the advantage of reduced processing time over displacement field fitting methods but do not produce measurements that are directly related to clinical understanding.

2.5 Regional strain calculation

As mentioned in Chapter 1, a wide variety of parameters are used by cardiologists to evaluate the performance of the heart muscle which include radial thickening, circumferential shortening, longitudinal shortening, the time derivatives of these quantities and the Eigen vectors and Eigen values of the strain tensor. Research in Croisille [CMJ99] has shown that 3D strains can additionally be used to differentiate between stunned and nonviable myocardium after ischaemic injury. This makes 3D strain maps an essential tool in modelling, understanding and quantifying cardiac contraction in normal and pathological situations and will lead to better management of patients affected by the particular diseases.

However, as discussed in Bogaert [BR01], the myocardial strain pattern is complex and closely related to the variations in transmural fibre orientation, the irregular shape of the LV and the local differences in ventricular morphology like radius of curvature and wall thickness. These observations are supported by Shi [SSC⁺99] which claims that the non-homogeneous and non-linear stress-strain relationship throughout the myocardium is determined by the architectures and orientations of the myofibres, the organisation of the myocardial sheets and the collagen inter-connections between the micro-structures.

2.5.1 Frames of reference

Strain can be thought of as the measure of contraction which in turn measures the functionality of the ventricle. It can be measured in either the Lagrangian or Eulerian frame of reference. In the Lagrangian frame of reference, 1D strain of an object at time, t , is the ratio of the difference between the length of the object at time t and the original length of the object against the original length of the object. In contrast, Eulerian (or natural) strain is defined as the integral of the infinitesimally small amount of deformation occurring over an infinitesimally small time interval. In other words, Lagrangian strain represents the tissue strain at a specific location in the myocardium whereas Eulerian strain represents the tissue strain at a specific location in space. In practical terms, this difference in reference frame and coordinate system means that a positive Eulerian strain will be smaller than the Lagrangian equivalent and conversely a negative Eulerian

strain will be larger than the Lagrangian equivalent. To compare results between techniques or experiments it is, therefore, important to ensure that the strain is being measured in the same coordinate system.

2.5.2 Types of strain in the myocardium

There are two different approaches to calculating the myocardial strain of which the first approach was to base the coordinate for calculation on the tissue fibre direction along with precise orientation angles. The second and more popular approach is based on the cardiac geometry to define three orthogonal strains at each point making it more convenient for clinical purposes. This approach uses the coordinate system of the constructed LV model by using the radial, circumferential and longitudinal directions as the normal directions for the calculation of the regional strain. The radial and circumferential strains describe myocardial shortening in the short axis plane while longitudinal strain is the shortening of the myocardium from the base to apex along the long axis of the LV. The radial strain is in the radial direction towards the centre of the LV whereas circumferential strain is in a direction tangential to the epicardial surface. In this system a positive radial strain during systole reflects the regional contribution to wall thickening while a negative radial strain implies local wall thinning. With circumferential strain, negative values imply contraction and positive values indicate systolic bulging.

It is important to note that strain is independent of rigid body motion with normal strains as well as shear strains used to represent regional myocardial function. The three shear strains that are calculated are the radial-circumferential shear strain, the radial-longitudinal shear strain and the circumferential-longitudinal shear strain. In an LV model the circumferential-longitudinal shear strain is widely known as the torsion as it describes the twisting motion of the heart. Torsion which is characterised by the wringing motion of the LV during systole is caused by basal clockwise rotation and apical anti-clockwise rotation.

2.5.3 Strain calculation

Regional strain values of a model can be computed with knowledge of its deformation, the material properties of the heart and equations based on continuum mechanics. A 3D strain tensor is characterised by both length direction and the fractional change in length relative to its original length which can be defined in either the Lagrangian or Eulerian frames of reference. A strain tensor can thus, be used to quantify myocardial performance since it isolates the local deformation of the myocardium. The objective of the analysis of tagged images is hence, to obtain an estimate of the six components of the strain tensor at each point in the myocardium, at each time during the heart cycle.

The material properties of a model define how the shape changes when forces are applied to it, matching the properties of the human heart tissue as closely as possible to get the best possible results. Modelling the material properties of a muscle requires the consideration of the mechanical properties of the tissue. In the case of the myocardium, there are the passive tissue properties and the active muscle tension development to consider. The properties of the model may be considered to be homogeneous to simulate the function of a normal heart or inhomogeneous as would be expected in a diseased heart with necrosis or scarred tissue.

The two basic methods used to calculate regional strain patterns are using displacement fields and the finite element method with Lagrangian and Eulerian strain values the commonly calculated values in the literature. Displacement field fitting methods described in O'Dell [OMH⁺95], Denney [DJM97], Kuijer [KMG⁺00], Amini [ACER01] and Tustison [TDRA03] numerically differentiated the reconstructed displacement field to calculate regional strain. An early example of the finite element method can be found in Young [YA92], where the tag data is used to solve for low-order basis functions in finite element models of the heart. Haber [HMA00b] manage to calculate the regional strain values of the RV using finite elements while Park [PMMA05] use a finite element model to find the distribution of strain throughout the heart incorporating heart fibre orientation to analyse the cardiac function and differentiate between diseased and normal

conditions. Hu [HMA03] further works on the Haber [HMA00b] algorithm to statistically calculate the strain and stress of the heart including the fibre orientation creating an intuitive results model.

2.5.4 Calculated regional strain values

According to Epstein [Eps07], the typical values for radial, circumferential and longitudinal strains in healthy volunteers were found to be 0.35, -0.20 and -0.15 at end systole in the mid LV along the short axis. The circumferential, longitudinal, and radial strains increased from base to apex while the study conducted by Shehata [SCO⁺09] found that all three normal strain values increase from epicardium to endocardium.

Croisille [CMJ99] shows that radial strains differentiate viable from nonviable regions better than longitudinal or circumferential strains. However, Kuijer [KMG⁺02] found that radial strains show less regional variation.

During systole the base of the LV moves significantly further along the longitudinal axis than the apex, as found by Edvardsen [EGG⁺02], with the longitudinal velocities decreasing from base to apex from 7cm/s to 3cm/s. Both Moore [MLOMZ00] and Kuijer [KMG⁺02] confirm that maximum longitudinal as well as circumferential strains are greater at the apex than the base. In a healthy heart, the end-systolic circumferential and longitudinal strains increased gradually from base to apex and from epicardium to endocardium.

2.6 Visualization

The visualization techniques like the tagging techniques have developed over the years, starting from the use of simple animation to indicate motion to the use of more complex visualization techniques like the use of tensor ellipsoid, streamlines and hyperstreamlines to visualise more complex deformation and strain patterns.

Guttman [GZM97] integrates the display of the LV with the tMRI and depicts the motion by animation using polygon meshes and Gouraud-shaded quadrilaterals. Interactive displays were also used, allowing the user to control whether

to view a single, interpolated ‘shell’ representing a layer of the myocardium or a range of them.

Kerwin [KP98] concentrated their efforts in displaying the regional motion of the LV. In their first approach, they render just enough points, to clearly define the volume, as beads and generate a movie loop permitting vision of the motion of a point throughout the LV. The user is allowed to display several such strain movies simultaneously and synchronously (adapting to differing heart rates) or advance through movie frames manually to allow for better understanding of the data. In a second approach, Kerwin [KP98] uses connections between neighbouring points with colour coded lines to indicate length changes or average 1D axial strain between them. Each connection shows the average contraction in a given direction between two points in the myocardium. Second the connections move with the LV and therefore display information corresponding to the same piece of tissue at all time frames. Finally, Kerwin [KP98] uses 3D stereo pairs, for the end-diastole and end-systole time frames, depicting base-to-apex views of the points.

Wuensche [WLY04] uses colour maps and isosurfaces as well as the display of tensor ellipsoids at regular points throughout the mid-myocardium to visualize the strain information, while Wuensche [WY03] uses colour maps to give an overview of the strain distribution. Wuensche [WY03] have also used spectrum markers to indicate isocontours in the visualized scalar field and cyclical colour maps to reveal structures such as symmetries and discontinuities. Using tensor ellipsoids, streamlines and hyperstreamlines makes it possible to visualize complex deformation behaviour in a single image. In Wuensche [WY03] line integral convolution uncovers the presence of degenerate points at which the principal strains suddenly change direction.

2.7 Chapter summary

In this chapter the various tissue tagging techniques and problems associated with them are discussed. Of the various tagging techniques, 1-SPAMM is the most popular technique and will be used since it provides the advantage of easy visual inspection.

2.7 Chapter summary

The chapter also elaborates how tMRI images are acquired to capture the regional cardiac motion and discusses the existing research in converting these image slices into the required regional strain model.

3

Processing tMRI datasets using a Strain Estimation Pipeline

As discussed in the previous chapters, tMRI slices of the LV are used to calculate a regional strain model that can be used for diagnostic purposes. From the previous chapter it is clear that a sequence of modules can be used to convert the tMRI slice sequence into the final product of a regional strain model.

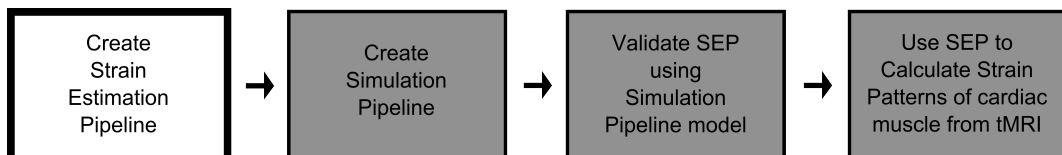


Figure 3.1: Research stage: SEP

This chapter discusses the conversion of tMRI slices into such a regional strain model. The first section discusses in detail the creation of the Strain Estimation Pipeline (SEP) and its modules, with special emphasis on the motion estimation methods. The final sections elaborate on how the SEP is evaluated and validated.

A Finite Element Model (FEM) is better suited to create the volumetric LV model due to its capacity to accurately model soft tissue mechanics and its applicability in the calculation of regional stress and strain. A FEM also lends itself nicely for varying tissue properties within the same model which is a condition that is important for this project. Since a FEM provides the most accurate tissue

representation and is thus most appropriate for the accuracy required for medical purposes, the methods used in the modules of the SEP will be dictated by its use.

3.1 Strain Estimation Pipeline

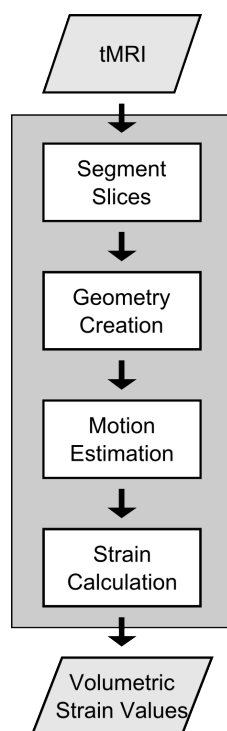


Figure 3.2: Strain Estimation Pipeline

As discussed in Chapter 2, the first step in processing an image slice is to identify the areas of interest. This includes the tag lines indicating the motion of the saturated muscle tissues of one or both the heart ventricles. The second step is to construct the geometry of the LV volume. The next crucial step is to estimate the motion of any given point in the volume of the LV. The final step is the calculation of the regional stress and strain of the LV.

It is clear to see that these modules need to be conducted in sequence and that the output of one module directly feeds into the next module (as its expected

3.1 Strain Estimation Pipeline

input) as seen in figure 3.2. This sequence of modules the tMRI dataset needs to be processed by to produce the required regional strain pattern information is defined as the SEP.

It is important to note that although the modules of the pipeline need to be followed in sequence to give meaningful results, they are independent of each other. In addition, although the development of the modules need not follow any sequence and may be done simultaneously, the modules of the SEP are developed in reverse order to ensure that the error introduced to the results of the SEP is introduced by the module being developed. As a result the ‘Estimate Motion’ module is developed first, followed by the ‘Create FEM’ module and finally the ‘Extract Features’ module.

The creation and testing of the SEP go alongside each other to arrive at or discover the best motion estimation method in the process of developing the SEP. The pipeline modules are developed with each iterative test phase resulting in adjustments to the entire SEP or a single SEP module to achieve the best results and accuracy.

As shown in figure 3.2, the first module extracts the areas of interest or features of the tMRI slices, in which the model geometry and the tag lines are identified and the next module uses this information to create a FEM. The next module uses the motion information that is extracted from the segmented tag lines to estimate the motion of the nodes of the created FEM and thus its deformation. The final module of the SEP calculates the regional stress and strain of the model using the commercially available FEM package, ANSYS. These steps together become the Strain Estimation Pipeline.

The modules are discussed in order of development. Thus strain calculation using the FEM package, ANSYS, is discussed first. The next module is the motion estimation of the FEM, followed by the creation of a FEM that is suitable for and understandable by ANSYS. This is followed by a discussion of the segmentation of the tMRI in which the LV wall boundaries and the tag line profiles are identified.

3.1.1 Calculation of strain

Stress and strain values are calculated using the available material properties of the heart tissue and continuum mechanics based equations using the FEM package, ANSYS. After the model has been integrated with the estimated motion information, the regional Lagrangian and Eulerian strains can be calculated. The work applied to deform a structure is stored as the stress energy, which is calculated by measuring the displacements of the points that define the structure. The deformation of the model or the 4D model is an expected input to the module and so it is outside this module.

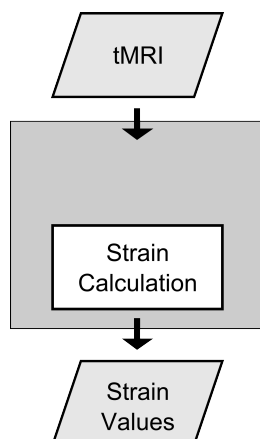


Figure 3.3: Calculation of strain in SEP

The two constants that are used to define the material properties of the solid are the Poisson's ratio and the Young's modulus. Poisson's ratio measures the tendency of a material to get thinner in the two directions that are not being stretched. Young's modulus is a measure of stiffness of a given material and the rate of change of stress with strain. According to Rodriguez [REW06] the change in the volume of the myocardium is less than 4% and as a result it is now widely accepted that the muscles are incompressible, undergoing volume-preserving deformations.

3.1.1.1 Tissue characteristics

The mechanical behaviour of the myocardium is complex and diverse with two aspects of its mechanical properties to be considered, the passive tissue properties and the active muscle tension development. According to research, a constitutive law for passive tissue properties requires a fully 3D relationship between the six components of strain (assuming symmetric material), whereas the active muscle law requires only a 1D relationship between the fibre strain and the active muscle tension in the myofibre direction. The active muscle tension development largely determines the active contraction and expansion of the myocardium. Incorporating active muscle law into the framework would add important physical constraints into the recovery process. However, since the objective is to calculate regional motion, not the forward activation of the LV and the active contraction phase is not clearly captured by tagging, the active muscle will not be considered. It should also be noted that the linear, isotropic constitutive equations do not properly describe the mechanical behaviours of the myocardium because myocardium is non-linear and an isotropic material undergoing finite deformation. A model of the heart would be more fully described by incorporating the orientation of the muscle fibres but it is beyond the scope of this project. The model does, however, have an approximation of the muscle tissue properties using the FEM package.

3.1.1.2 Poisson's ratio

The Poisson ratio is the ratio of the percent of expansion divided by the percent of compression, for small values of these changes. In other words, it measures the tendency of a material to get thinner in the two directions that are not being stretched. Poisson effect is the phenomenon whereby when a material is compressed in one direction, it tends to expand in the two directions perpendicular to the direction of compression and Poisson's ratio is a measure of this effect. If the material is stretched rather than compressed, it usually tends to contract in the directions transverse to the direction of stretching. In this case, the Poisson ratio is the ratio of relative contraction to relative stretching. In certain rare

cases, a material will actually shrink in the transverse direction when compressed or expand when stretched, which yields a negative value of the Poisson ratio.

The Poisson's ratio of a stable, isotropic, linear elastic material cannot be less than 1.0 nor greater than 0.5 since the Young's modulus, the shear modulus and bulk modulus are required to have positive values. Most materials have Poisson's ratio values ranging between 0.0 and 0.5; a perfectly incompressible material deformed elastically at small strains has a Poisson's ratio of exactly 0.5. Soft tissues are normally modelled using values close to but less than 0.5. However since soft tissue is nearly incompressible, research normally uses values starting from 0.499. For instance, Grande [GCRK98] uses a Poisson's ratio value of 0.45 to mimic the nearly incompressible behaviour that is expected of cardiac tissue.

3.1.1.3 Young's modulus

The modulus of elasticity or Young's modulus is a measure of stiffness of a given material. The Young's modulus for small strains, is defined as the ratio of the rate of change of stress with strain. This is experimentally determined from the slope of the stress-strain curve created during tensile tests conducted on a sample of the material. Young's modulus thus, allows the behaviour of a material under load to be calculated.

3.1.2 Estimation of motion

As discussed in chapter 2, there are different approaches that can be followed to estimate the motion of the LV model. The tMRI slices can be processed in the frequency domain, in the spatial domain or in both. Operating in the frequency domain offers the advantage of an increased possibility of completely automated processing but it involves complicated data analysis. The most popular approaches that operate in the spatial domain include methods based on non-rigid registration, optical flow and segmentation. The relative advantages and disadvantages of all the approaches are discussed in section 2.4.4.

The method for myocardial motion estimation in the SEP is dictated by the decision to use a FEM to model the LV. Since creating a FEM requires identifying the myocardial walls and tag lines, we follow a segmentation based approach to

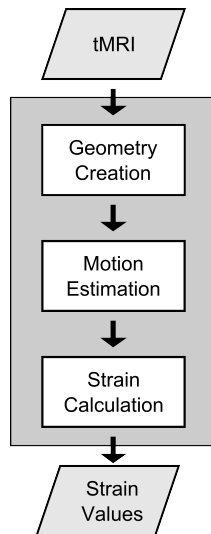


Figure 3.4: Motion estimation, strain estimation & geometry creation in SEP

reconstruct and estimate the motion of the myocardium. All segmentation based tracking methods tend to face problems near the chamber walls, where the epicardial and endocardial surfaces often appear as dark lines and are frequently confused as tag features. The myocardium near the chamber wall is particularly difficult to identify since tag lines can appear or disappear due to the combination of through-plane motion and chamber convexity. However, this is not a problem that is restricted to segmentation based methods and can cause failures for all the different approaches in several ways. For instance, the intensity template used by the tag line tracking approach may lock onto the chamber wall instead of a tag. Optical flow algorithms can be confused when the walls occlude tags resulting in spurious matches. Frequency domain processing can also result in motion inaccuracies caused by the walls by introducing apparent shifts of the tagging pattern in the tissue.

It is important to remember that the problem of reconstructing 3D motion using 2D motion information from tMRI slices is ill-posed regardless of the approach taken, with noise and image artefacts causing ambiguities in the tracking of tag, optical flow or phase features. As a result, researchers use different regularisation methods which balances staying true to information from the tag features with

3.1 Strain Estimation Pipeline

Table 3.1: Algorithm for Motion Estimation

Stage One - Creation of Motion Cloud (MC)

1. Create MC using tag line motion information from all VS

Stage Two - Estimate deformation of FEM (motion of nodes)

2. For each time step t
 2. 1. Read node output file from ANSYS
 2. 2. For each node n in output file - Estimate node locations at time step $t+1$
 2. 2. 1. Find closest MC points to the node n
 2. 2. 2. Sort the list of MC points in increasing distance from n
 2. 2. 3. Enforce selected threshold conditions
 2. 2. 4. Apply weights to chosen MC points list
 2. 2. 5. Calculate the motion (of n at $t+1$) using selected mechanics equations
 2. 3. Generate node modification file for time $t+1$ (to be used by ANSYS)
-

the smoothness constraint.

3.1.2.1 Overview of proposed method

As mentioned in Chapter 2, segmentation based motion reconstruction methods work by using the reconstructed tag plane information to estimate the motion of the chamber volume. The approach used here avoids reconstructing the tag planes and instead interpolates the motion of a given FEM node based on all the motion information that can be collected from the segmented slices. The basic motion estimation idea is to calculate the motion of the nodes of the FEM based on the motion of those neighbours for which the motion is known. This is done in separate stages as seen in table 3.1. Splitting the estimation in two stages allows for the isolation of errors which in turn improves the scope for improvement of the method accuracy.

The first stage of the motion estimation collects the points for which partial motion information is known (using the VS created from the tMRI slice stack sequence). This information is stored and termed as the Motion Cloud (MC) since it represents the 3D motion of the volume without any knowledge of its structure or geometry. Thus, the MC acts as a data structure storing the motion

Table 3.2: Algorithm for weighted contribution of selected MC points

-
1. For each MC point in list
 2. If inverse weight is required :
 1. set weight to be $(1.0 / \text{distance to the node})$
 3. If inverse square weight is required :
 1. set weight to be $(1.0 / \text{square}(\text{distance to the node}))$
-

information of all the arbitrary points in the volume for which motion is known.

The second stage of motion estimation computes the motion of the nodes based on the MC information. The motion of a FEM node is calculated as a function of the MC points that are closest to it where the individual contribution of each chosen MC point can be set or weighted as detailed in table 3.2.

3.1.2.2 Stage One - constructing a motion cloud

The MC is constructed from the motion information gleaned from tag lines that were identified in the segmentation step. It is the source of the closest points to a given FEM node in the imaged volume over the systolic duration. To get maximal motion information, the MC needs to have motion knowledge in three orthogonal directions of a volume. The MC is, thus, the motion information that is extracted from the segmented tag lines of a tMRI slice stack sequence, where each point in the MC stores the partial displacement in the direction perpendicular to the increment direction of the tag lines on a slice. It is in this direction that a set of tag lines are said to be ‘in’, making y tag lines those that increment in the y direction. Tag lines can only be used to calculate partial displacement in the direction of its increment due to the indiscernible ‘through plane’ motion as mentioned in Chapter 2.

A significant number of material points, whose motion is being tracked, along a tag line makes it feasible to assume that the motion between any two material points is minute and insignificant. The motion component along the tag line can then be assumed fixed and the component of displacement in the tag line direction calculated as a simple difference of the positions at the different time steps.

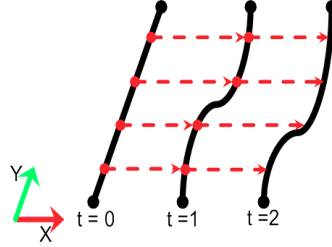


Figure 3.5: Partial displacement information
by ignoring movement within tag line in estimation

Calculating the partial displacement of a tag line over the duration of a heart beat will ultimately result in a separate motion mesh for each coordinate direction along which the tag lines are incremented. A motion mesh is a purely logical structure where a given motion mesh is said to be a primary mesh for the direction of the tag plane increment since it is along this direction that partial displacement can be discerned (and secondary for the remaining two directions) as seen in figure 3.6.

Figure 3.7 shows a number of motion meshes and the resulting MC. The appropriate motion mesh will be searched for the closest mesh point component to calculate the motion of a given FEM point in that direction. In other words, the reconstruction of the 3D motion of a node is estimated from the motion gathered from a collection of three orthogonal motion meshes that each store the one-dimensional motion information of a single tMRI slice stack sequence.

3.1.2.3 Selection of mesh points or neighbours

The next stage of the motion estimation is the selection of the appropriate MC points that influence the motion of a given FEM node for each time step. The MC points need to be selected for each time step since the motion information of each time step is taken from 2D tMRI slices which means that due to through-plane motion the MC points selected in time step i may not be the best choice at time step $i+n$.

It is reasonable to assume that the closest MC point to a node can be used to calculate its motion in a tissue structure. It is further reasonable to assume that

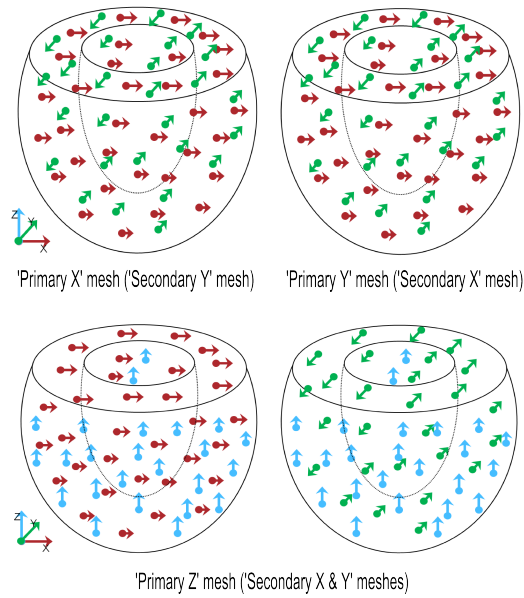


Figure 3.6: Motion meshes

primary X mesh and primary Y mesh created from SA slices; primary Z mesh created from LA slices

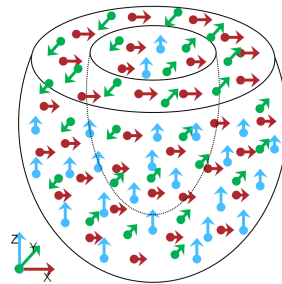


Figure 3.7: Motion cloud (MC)
created by multiple motion meshes

3.1 Strain Estimation Pipeline

the effect of a MC point diminishes as its distance from the node increases. One way to account for the diminishing influence of MC points in the calculation of node motion is to weight the contribution of the MC points based on its distance from the node. The weight can be simply calculated based on the number of MC points or it can be a more complex calculation based on both the number of MC points and its distance from the node.

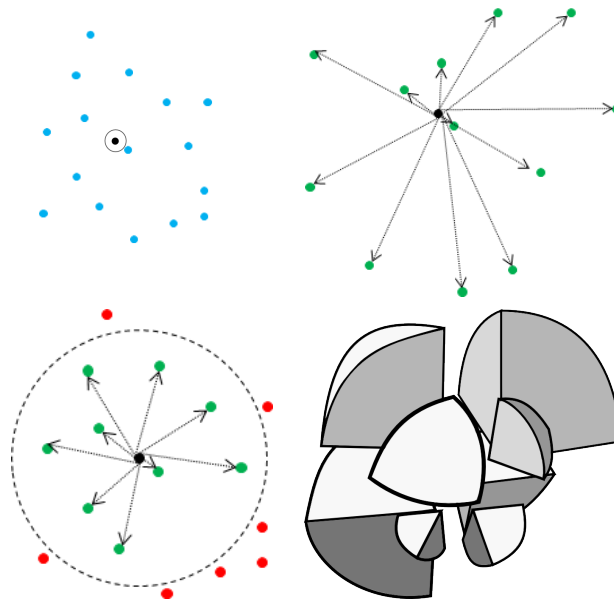


Figure 3.8: Selecting mesh points from MC

1:Surrounding mesh points in MC; 2:Selection of a threshold number of mesh points from MC; 3:Selection of mesh points from MC using a maximum distance; 4:Using spatial awareness to ensure neighbours exist in surrounding eight quadrants

There are a number of different strategies of increasing complexity can be adopted in the selection of MC points as seen in figure 3.8. Variations to the selection of the MC points are made based on fulfilling certain conditions and the relative location of the point to the node of the FEM. The first set of algorithms, to find the appropriate influencing mesh points, is based on the physical location of the neighbours either in relation to each other or to the node itself. The simplest methods check that a threshold criterion is achieved. The first criterion is the minimum numbers of identified neighbours seen in table 3.3 and the other

3.1 Strain Estimation Pipeline

Table 3.3: Algorithm to enforce that a given number of MC points are selected

-
1. If the selected MC points are less than the required number :
 1. Find the closest MC points to each of the MC points in the selected list
 2. Sort the list of selected MC points in increasing order of the distance from the node
 2. If the selected MC points are more than the required number :
 1. Delete the extra MC points from the end of the list
-

Table 3.4: Algorithm to enforce that the selected MC points are not more than a maximum distance away from the node

-
1. For each selected MC point
 2. If the distance from the node is greater than the maximum threshold distance :
 3. Remove the MC point from the selected MC points list
-

is that the maximum allowed distance of the mesh points from the node is not exceeded as seen in table 3.4.

The next set of algorithms incorporates spatial awareness by ensuring that there are a minimum number of neighbours possibly within a threshold radius, in every possible direction. By splitting the 3D space in the Cartesian coordinate system using the node as the origin we get eight quadrants within which, where possible, mesh points need to be found as depicted in figure 3.8 by the different sized wedges. Thus, as seen in the algorithm 3.5, the objective is not simply to find the closest points but to find the closest points in each different direction.

The final algorithm deals with the situation in which there are either not enough or no neighbouring mesh points from a given primary mesh that meets the threshold condition. The solution here is to use the neighbours from the secondary meshes that do meet the threshold criteria. The secondary mesh points are used as input to query the primary mesh to have the motion component estimated. The motion for these points is estimated by finding the closest mesh points that meets the threshold criteria. This motion information is only used in lieu of motion information from the primary motion mesh.

Table 3.5: Algorithm for a spatially aware selection of MC points

-
1. Find the position of each selected MC point relative to the node
 2. For each selected MC point
 2. 1. Find the position of the selected MC point relative to the node
 2. 2. Save the MC point in the appropriate quadrant list
 3. For each quadrant list
 3. 1. Enforce that threshold conditions are met by the list and the MC points in the list
-

3.1.2.4 Computing the motion of the FEM nodes

Once the influencing MC points have been selected, a computation algorithm is used to calculate a possible position of the given node in the volume.

The first set of implemented algorithms differ based on the motion mechanics model used to make the calculation. The motion of a point can be calculated according to classic mechanics (Newtonian) or analytical mechanics (Lagrangian or Hamiltonian). Classic mechanics use Newtonian equations of motion while analytical mechanics use the momentum of a point in calculating its displacement. The velocity and acceleration of the selected mesh points are used in estimating the motion of the Node using both Classical and Analytical mechanics approaches. When implemented the Euler-Lagrangian equations are very similar to Hamiltonian equations. Lagrangian mechanics assumes that the total energy is fixed and calculates the path as that in which the time integral of the kinetic energy is least. Hamiltonian mechanics allows time varying energy identifying the path along which the action or difference between the kinetic and potential energy is least, which makes it best suited for quantum mechanics.

Lagrangian (or Euler-Lagrangian) mechanics is implemented with the use of springs to incorporate momentum as described in 3.6. To this end the tag planes are modelled using a mass-spring system which is a grid-like structure of point masses connected to neighbouring masses by springs. This is ideally suited to the implementation of the motion estimation module since it is simply a question of adding springs to connect the chosen MC points and the FEM node. These springs exert forces on the connected FEM node and thus influence its motion. A

3.1 Strain Estimation Pipeline

Table 3.6: Algorithm to compute motion using analytical mechanics

-
1. For each selected MC point
 1. 1. Set up spring connecting MC point to the node at time t
 1. 2. Calculate forces applied by MC point on node along spring connection at time $t+1$
 1. 3. Update acceleration, velocity and displacement of node based on MC point
-

number of different types of springs are used to connect the points of the MC to enforce the expected behaviour. Each spring of the system can be damped, which reduces the speed of the point, to increase the stability of the system. Details of these calculations can be found in Appendix B. The first type of spring used is the ‘structural’ spring to prevent the point masses from moving to close or too far away from each other by connecting adjacent masses to each other, defining the shape of the tag plane. Two additional springs are used to maintain the shape of the tag plane when the deforming forces are applied to the points. A ‘flexion’ spring connects every alternate mass in the system to regulate the bending of the tissue plane by opposing movement of the points over different planes while the ‘shear’ springs connect diagonally adjacent masses to each other to opposing shearing deformations.

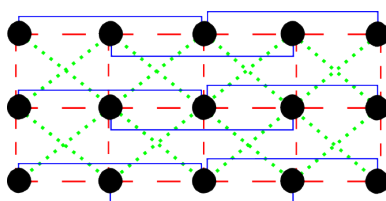


Figure 3.9: Springs connecting tag plane points

‘structural’ springs are indicated by the dashed lines, while ‘flexion’ springs are indicated by the dotted lines and ‘shear’ springs are indicated by the continuous lines

An advantage of using spring connections between the selected mesh points and the node in question is that it can simulate material properties incorporating the properties into the calculation of motion of the FEM node. However, using

springs to simulate materials is difficult to get correct when the underlying internal structure is known and is likely to create an unstable system since there is no physical internal structure to work with but it may be that this will provide better results than ignoring the material properties during the computation of motion.

The next set of algorithms vary the individual contribution of an MC point towards the final motion of the node based on the inverse of the distance or the square of distance between the points. The variation on each of the algorithms is to use the numerical integration technique of the fourth order Runge Kutta.

3.1.3 Creation of geometry

The model or geometry is generated based on contour information from the end-diastolic images which are also the starting point for recovering the 3D motion from the tMRI slices, where end-diastole is the end of the relaxation phase, right before the heart begins contracting in systole.

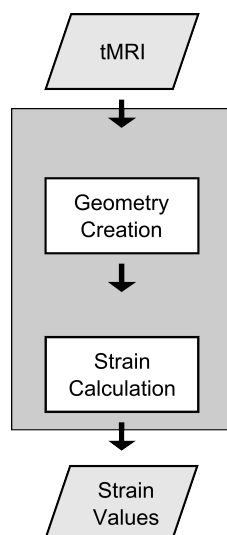


Figure 3.10: Strain estimation & geometry creation in SEP

As mentioned in Chapter 2, the two methods that are commonly used to model the geometry of the ventricles are modelling the volume using finite elements

3.1 Strain Estimation Pipeline

or modelling the walls of the volume using quadric surfaces. Park [PMYA96], Amini [ACC⁺98], Tustison [TADRA02] and Tustison [TAA04] use quadric curves and surfaces whereas Young [YKDA95], Haber [HMA00b], Park [PMMA05] and Cupps [CBW⁺08] are among the many that use finite element meshes to model the heart. Although quadric curves and surfaces have the advantage of a compact representation and parametric continuity the major advantage of using the FEM lies in its accuracy in estimating the mechanical properties of the heart muscle. It is for this key reason that FEM is used to model the LV geometry.

Haber [HMA00b] uses a finite element mesh geometry along with the deformable modelling approach applying Lagrange's equations of motion with spring like forces to attract the model to data extracted from the image. Park [PMMA05] provides another example of modelling using the FEM method, creating an initial anatomically accurate finite element model of the heart using the blending technique discussed in section 2.3.1. This accurate model is refined to create a patient specific model by adaptively varying a set of parameter function that creates external forces resulting in motion towards the required curve or to fit the segmented data.

There are two approaches that can be taken to create the model geometry. The first is to start with an existing geometric model, fitting the image data to it and the other is to start with the image data and create a geometry model from it. The advantage of creating a model from an image rather than having the model fit the image is that the model will not be restricted by ill-conceived notions of what the model should be and can thus adapt to the peculiarities of an individual LV. This approach can also help us to move towards a comprehensive shape atlas with multiple datasets. Of the two approaches fitting a model to an image is more popular in the research for the possible reason that the method helps to minimise the errors caused by inaccuracies in the automatic segmentation of the chamber walls. However, since the focus of the project is the estimation technique and not the anatomical accuracy of the model the approach followed here is to work from the image and create the model from the tMRI slice rather than fit the segmented tMRI wall boundaries to an existing LV volume. This approach is easy to change when the research expands to require the assurance of a more anatomically accurate model.

In general, the FEM geometry is defined in two stages with an initial partitioning of the identified contours into FEM nodes in the first stage and the generation of the FEM elements using those nodes in the second stage.

3.1.3.1 Aligning the slices

The additional step of aligning the slices is done first to make the calculation of the node positions less complicated.

The calculation of the node positions can be made easier by moving and aligning the slices to an axis that passes through the origin of the coordinate system, as shown in the figure 3.11. The axis is defined as the line that is perpendicular to the SA slices and passes through the centre of the chamber volume and its tip at the initial time step. All the LA slices are aligned to this imaginary line or axis and the SA slices are aligned about the point that is the intersection of the axis with the slice plane. The identified line will thus be the axis of the chamber volume that is to be constructed.

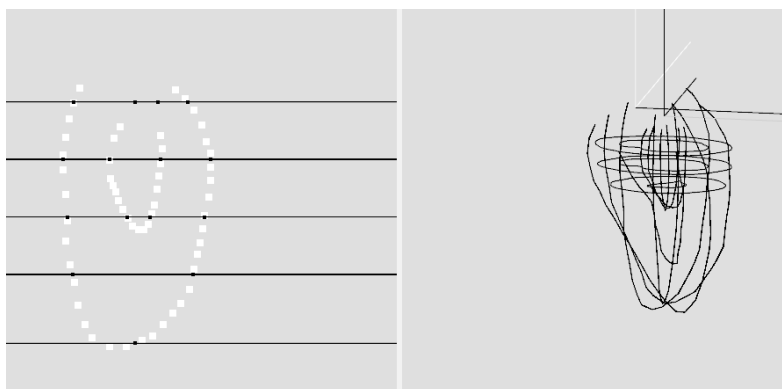


Figure 3.11: Step one of creating the FEM
using LA tMRI slices

In some of the literature it is found that a correction of the global motion may be required when there is a local central axis that is required to run through the centre of the LV at all times for the purposes of calculations. The correction of the global motion is attempted using geometric transformations at every stage to realign the axis with the centre of the chamber and the base of the LV thus

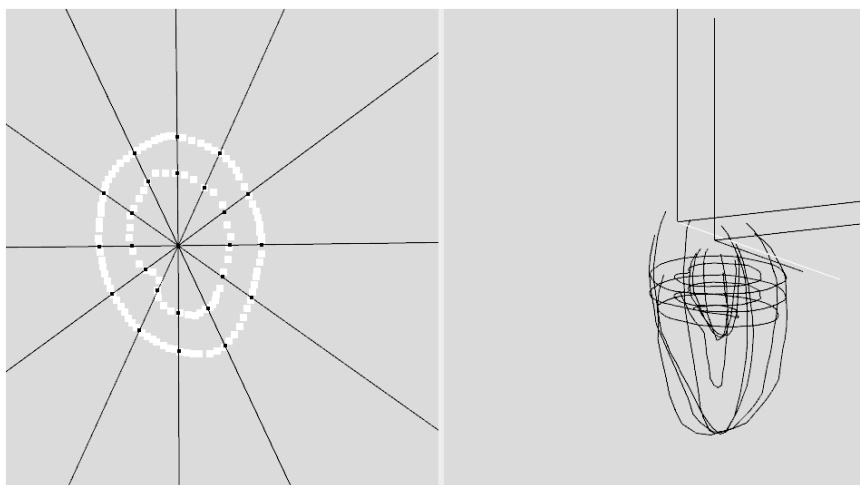


Figure 3.12: Step two of creating the FEM
using SA tMRI slices

making adjustments for the global motion of the heart. No correction is made here since the central axis is taken to be the axis that runs through the centre of the SA slice. Since the FEM is created at the first time step the global motion does not affect the model geometry. The estimated motion will, however, include any global motion that is conveyed in the tMRI images. This approach need not be a problem unless the FEM package, ANSYS, restricts the model is fixed for the stress or strain values to be calculated.

3.1.3.2 Calculating the FEM nodes

The basic method used to create the FEM nodes calculates the positions of a node as the intersection of the slice information and the two planes on which the FEM node is required. The LA slice is used as the guide to construct the volume according to the requirements of ANSYS by setting the distances along the axis at which nodes will be created. In other words, the nodes are specified at defined distances along the axis, thus setting the z values of their positions, as seen in figure 3.13.

The initial partitioning of the identified contours into FEM nodes is implemented by splitting the concentric contours of the inner and outer walls that are

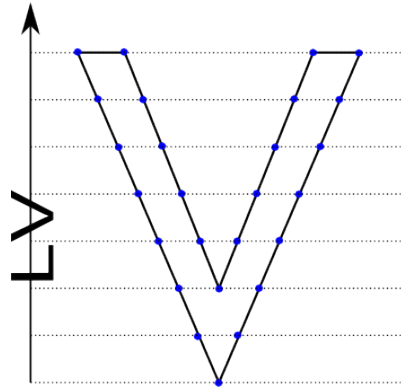


Figure 3.13: Calculating the FEM nodes
creating nodes along the LA and calculating the x and y positions of the nodes using LA slices

identified from the SA slices into segments, or two nodes, by throwing or casting rays at equal angles from the centre of the volume as seen in figure 3.14. The casting of the rays is made especially less complex by aligning the slices before calculating the node positions.

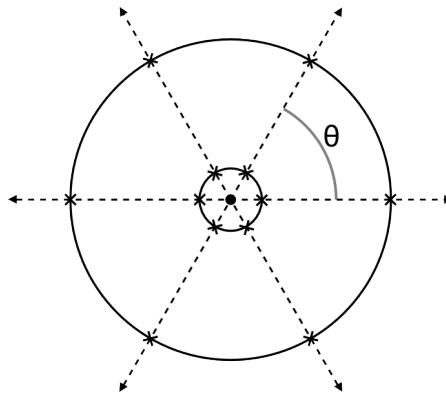


Figure 3.14: ‘Throwing’ of radial rays to create FEM elements

Both the LA slices and the SA slices are then used to fill in the gaps in x and y position information by a calculation of intersection of the known closest points on a slice or slices as seen in figures 3.13 and 3.14.

Once these values are calculated, the values for the remaining nodes are filled

in depending how many nodes there need to be along each ray that was cast out. The nodes thus calculated are combined to form the required shape of ANSYS element.

3.1.3.3 Creating the FEM elements

In ANSYS, a FEM is specified as a list of elements, each being defined as a list of nodes. This means that the segmented information of the chamber wall edges need to be fit to a model or split up into the elements that create the model and represented in the format required by ANSYS. This can be seen in figure 3.15.

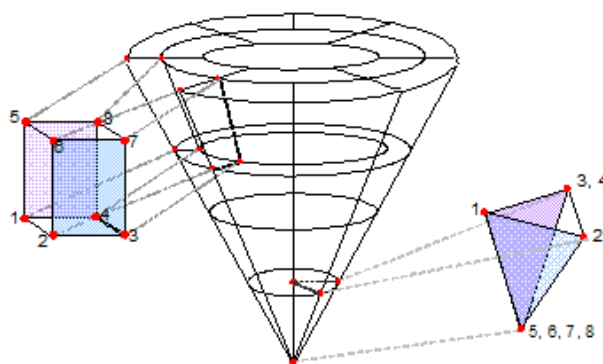


Figure 3.15: Specification of elements of type SOLID185 in ANSYS

There are a variety of possible types of elements that can be used to model solid structures in ANSYS. The structural solid, SOLID185, is used to describe the mathematical model of the LV. It is defined by eight nodes, each having three degrees of freedom.

3.1.4 Extraction of features

As repeated before, the strain distribution of the LV model is calculated using the FEM because of the capacity of the method to model soft tissue accurately. The features that need to be segmented from a tMRI slice are the edges of both the inside and outside walls of the LV, in order to create the FEM, and the set of tag lines, in order to calculate its deformation.

As mentioned before, the problem with segmentation is the time it takes and the expertise required for accuracy. It is well established that one of the most time-consuming processes in tMRI based heart analysis is the extraction of the tags and boundaries. In addition, tag segmentation based motion estimation techniques were identified in even the early research by Kerwin [KP98] as having the potential to improve result accuracy by showing that there is a loss of motion accuracy near the LV boundary that traced back from the accuracy of the tag recognition algorithm. Since the focus of the work is the motion estimation and not the segmentation itself, semi-automated and manual segmentation approaches are explored. Although manual segmentation is more likely to provide the most accurate motion and estimation results, it is labour intensive and is the last approach considered. The different semi-automated approaches that are investigated for their applicability are edge-based, region-based and active contour model based segmentation. In addition, a gradient vector flow method that uses the knowledge of the geometry of the ventricle and the tag lines to act as heuristics in guiding the segmentation and a non-rigid registration based approach are explored as well. These approaches are explored using modified Matlab code from various publicly available sources.

Of the techniques explored in MATLAB, the most notable methods are edge-based segmentation and the use of snakes. The use of varying amounts of manual control is also explored for every trialled approach.

3.1.4.1 Edge-based segmentation using MATLAB

The first method that was explored to extract the chamber wall edges and the tag line features from the tMRI slices using Matlab is edge based segmentation.

As the name suggests the aim of edge-based segmentation is to identify points in the image at which the brightness changes which is then organised into a set of curved line segments or edges. However, due to the complexity of the tMRI slices this is not always easy.

The first results of segmentation using the Sobel approach is seen in figure 3.16. As seen the edges that are detected are in the areas that are of no interest to us. Since this may have been caused by the fact that the tissue region that

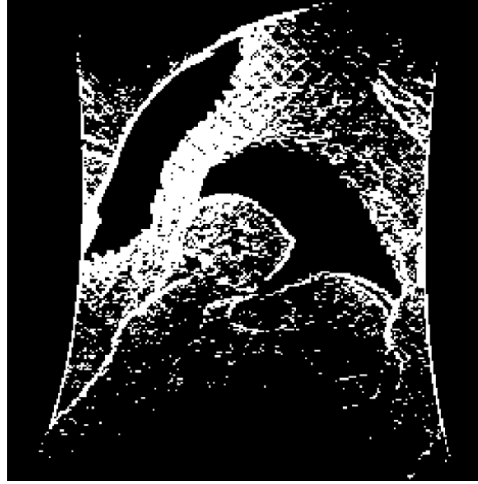


Figure 3.16: Initial edge-based segmentation attempt
Results in MATLAB

should be identified is a very small portion of the slice in the original image, when the Canny edge detector algorithm is tried the original image is cropped to include only the heart chamber tissue. Although this algorithm yields better results with some of the required edges detected, as seen in figure 3.17, the results would not be usable without further manual intervention and was hence deemed as not accurate enough for our purpose.

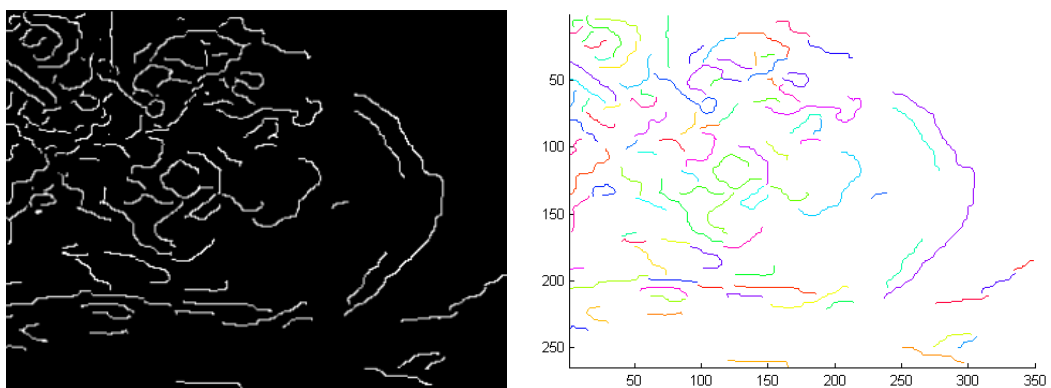


Figure 3.17: Canny edge-based segmentation
Results in MATLAB

3.1.4.2 Snakes using MATLAB

The active contour model, or snakes, is a framework for delineating an object outline. The framework works by minimising the energy associated to the contour as a sum of an internal and external energy, where the external energy is dictated by the position and the internal energy is dictated by the shape. Figure 3.18 shows the result of a simple version of the active contour method as implemented in Matlab.

As seen in the figure active contour methods for image segmentation allow a contour to deform iteratively to partition an image into regions. The next snake that is tried with the tMRI slices is using level set methods which are popular due to its power and versatility. Since these methods are slow to compute the efficient sparse field method implemented by Lankton [Lan09] is used. The results of using this method, as shown in figure 3.19, are better than previous methods with one of the edges of the chamber walls detected.

The final variation of the snake that is tried is the Gradient Vector Flow or GVF snake. The use of GVF active contours are explored because of its known ability to handle broken object edges. The gradient vector flow computation causes diffuse forces to exist far from the object, and crisp force vectors near the edge, which is combined with the internal forces. The implementation of the GVF snake is explored as a semi-automatic segmentation method with the heuristic of prior knowledge of the structures. This is done using modified C++ code from various publicly available sources. The inside walls are detected by starting the search from the centre of the slice while the outside wall is detected by starting from the edges of the slice moving towards the centre.

As seen in figure 3.20, this method provides the best results with the closest identification of the chamber walls. The top left image shows the initial contour that is used as the heuristic, while the top right shows the external energy. The bottom left image shows the internal force and the bottom right image shows the movement of the snake and the final result. However, due to the amount of noise present in the data, a considerable amount of modifications to the algorithm or manual interaction would be required to get accurate results. Due to the time constraints involved in detecting both the chamber walls and tag lines it was

3.1 Strain Estimation Pipeline

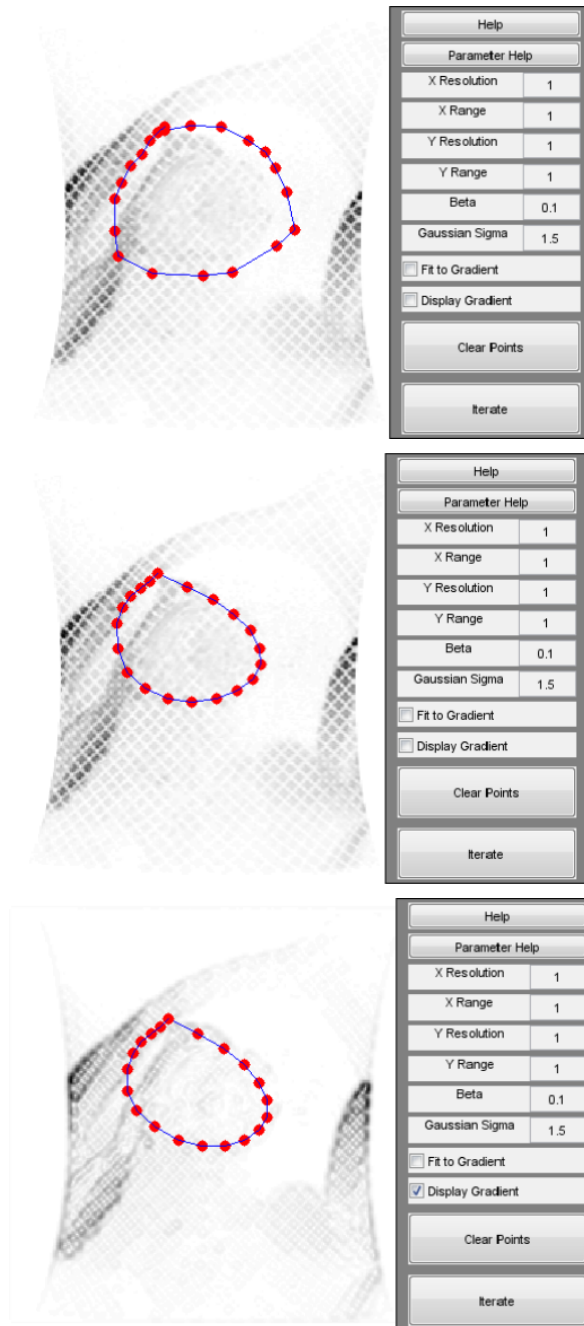


Figure 3.18: Basic active contour model based segmentation
Results in MATLAB

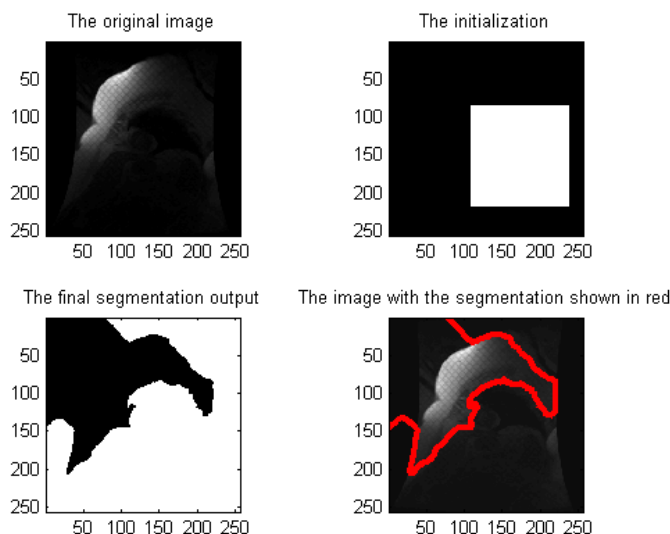


Figure 3.19: Result of sparse field method
implemented by Lankton [Lan09] in MATLAB

decided to abandon the semi-automatic segmentation in favour of the manual segmentation despite its time intensive nature.

3.1.4.3 Conclusion

Tuning the different ‘Extract Features’ algorithms to achieve reasonable accuracy in MATLAB for the most part involved manual intervention or the introduction of more manual controls, finally taking almost as much time as a completely manual segmentation process. In addition, the ‘Create FEM’ module requires any output to be in the intermediate ‘Virtual Slice’ format of the SEP requiring further processing of any results of the segmentation algorithms. The difficulty in converting the results of region based segmentation and the non-rigid registration methods made these algorithms unsuitable for the SEP. Although converting the results of the edge-based segmentation and active contour model algorithms into the ‘Virtual Slice’ format is not complex, the achieved accuracy with these methods was unreliable with the results dependant on both the dataset and the position of the slice.

The complete SEP can be seen in figure 3.21.

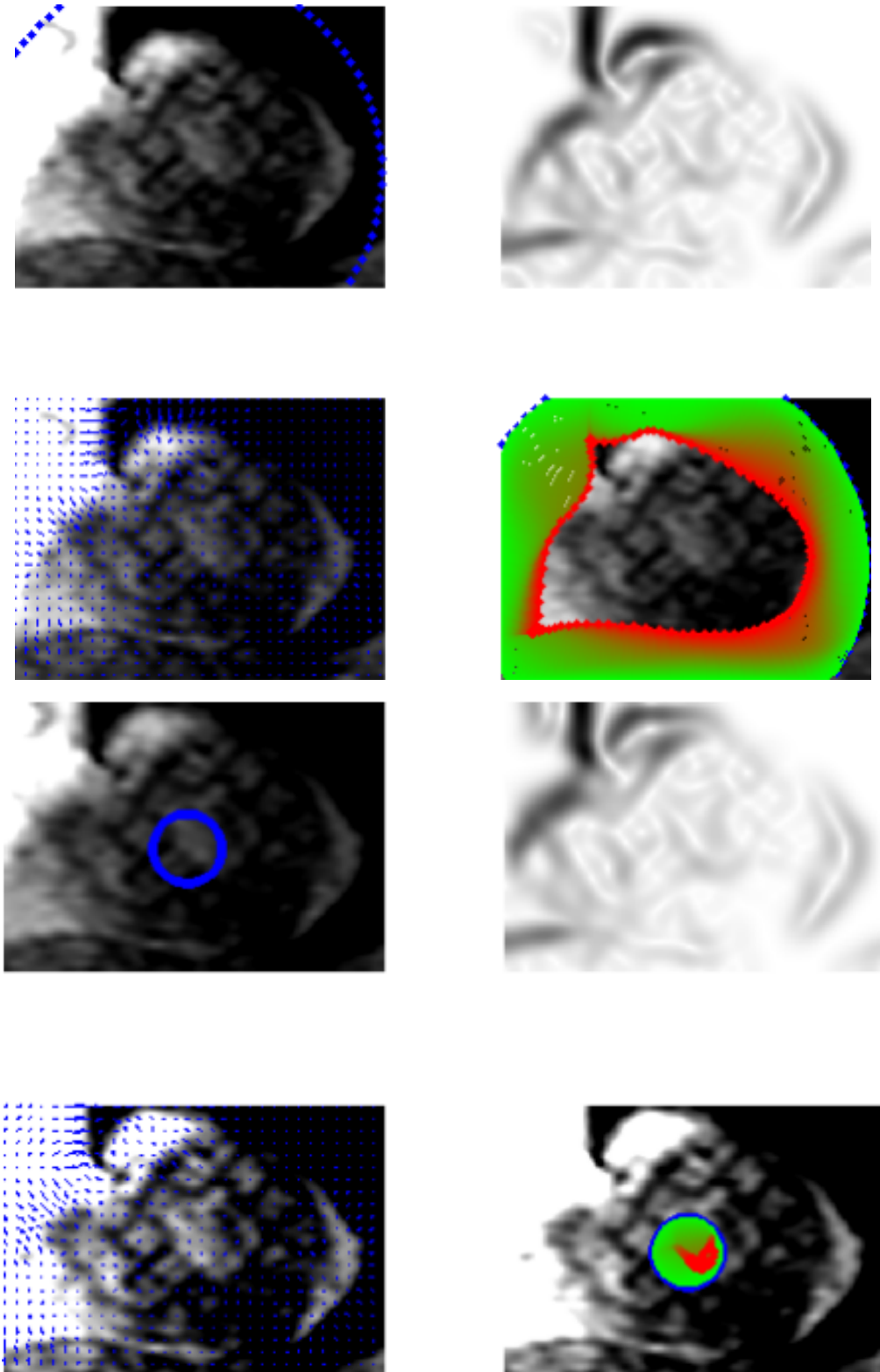


Figure 3.20: Using GVF to extract chamber walls
Results in MATLAB

3.1 Strain Estimation Pipeline

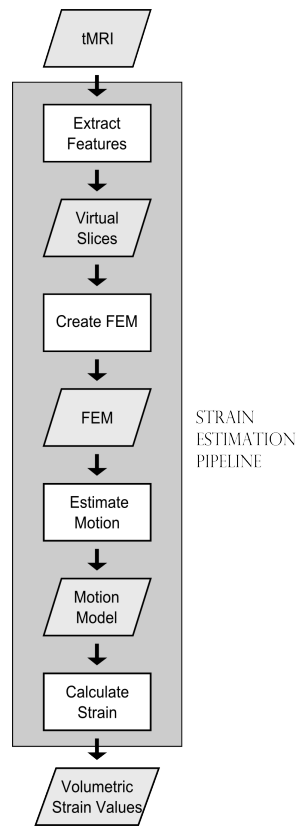


Figure 3.21: Final SEP with the expected inputs and outputs

3.2 Evaluation and validation of results

Before the SEP can be used with any confidence to process tMRI slices, the result of the SEP and its constituent modules need to be verified or validated. This section briefly discusses the specifics of developing the Strain Estimation Pipeline and validating its output, to test the accuracy of the regional strain model that can be achieved by using it. According to Bhola [Bho90], “evaluation is a process of judging the merit or worth of something”. There is broad consensus that the major goal of evaluation should be to influence decision-making through the provision of empirically-driven feedback. The most important basic distinction in evaluation types is that between formative and summative evaluation. Formative evaluations strengthen or improve the object being evaluated, helping to form it by examining the delivery of the program or technology, the quality of its implementation, and the assessment of context, procedures, etc. Summative evaluations, in contrast, examine the effects and outcomes by summarizing or describing what happens subsequent to delivery of the program and determining the overall impact beyond the immediate target outcomes. Thus, formative evaluations are ongoing through the course of the project and summative evaluation is effectively, the evaluation of the result.

The evaluation of the SEP comes under the formative evaluation of the project and involves the investigation of the process of delivering the results and possible alternatives. On the other hand, the summative evaluation of the project involves the evaluation of the LV Regional Strain model. This involves answering the main question of the effectiveness of the program and its impact, ideally examining the results and existing data to address new questions or use methods not previously employed and integrate multiple studies to arrive at an overall or summary judgement. To avoid confusion, formative evaluation of the project is referred to simply as evaluation and summative evaluation is referred to as validation. The evaluation of the SEP and its modules are discussed in further detail in Chapter 3 and the validation of the results of the SEP are discussed in Chapter 5.

3.2.1 Validation of tMRI processing algorithms

There are a number of methods that have been used to verify the results of the algorithms that process tMRI. Although the most popular approach taken is manual verification using the tMRI slices, algorithms are frequently validated using synthetic or simulated data. The techniques used are dependant on the process itself. For instance, manual verification tends to be used for image processing tasks like segmentation while simulated or synthetic data tends to be used to verify the motion reconstruction. Most segmentation techniques, like Kumar [KG94], are validated and evaluated by comparing its results to that achieved by an expert manual segmentation. Manual verification is also used by Chandrashekhara [CMR04] to validate the results of their non-rigid registration algorithm by tracking tag intersections and comparing the results. However, a drawback of this kind of verification is that it is limited to the plane of the tMRI slice and thus cannot verify the more complex through-plane motion when used to validate the motion reconstruction accuracy.

The approach generally taken for validation of the reconstructed motion is to use a simulation model. This may be a physical simulation approach as taken by Young [YAD⁺93], Kraitchman [KYCA95], Park [PMYA96], Sampath [SP07] and Abd-Elmoniem [AEOPS07]. These researchers use a phantom model whose strain patterns can be calculated to validate their algorithms. However, the problem with this approach is that the model tends to be a very basic annulus or ring shaped gel phantom thus not accounting for the varying complexity of the LV geometry and motion.

Subsequently, the next approach taken is to generate a mathematical model that simulates the heart ventricle or ventricles and to generate tMRI of this model, which in turn is used to validate algorithms. Researchers tend to extend and adapt the work in Arts [AHD⁺92] and Waks [WPD96], which simulated the motion of prolate spheroidal shell using canine LV motion data obtained using implanted beads. The next stage in the validation process is the faithful simulation of tMRI after which the slices created are used to test and validate the algorithms. Kerwin [KP98] validates their method by tracking specific material points during deformation. This is a popular approach used by many other

3.2 Evaluation and validation of results

researchers including Amini [ACC⁺98], Amini [ACER01], Huang [HADRA99], Rougon [RPP⁺05] and Tustison [TA06]. A fairly recent approach is to use synthetic data to validate tracking algorithms. Xu [XPI⁺10] creates data used for validation by superimposing synthetic tags on static ex vivo ovine heart images. The intersection points of the synthetic image dataset are then tracked using a 3D optical flow based algorithm and the result is validated against a manually tracked result. The limitation with the simulation and synthetic approach is the validation is restricted to the two dimensions of the tMRI image generated making the calculated through-plane motion largely unverified.

All these methods work in principle but are sometimes not as robust they need to be. For instance, Montillo [MMA02] first does a qualitative comparison of the results of the automated segmentation algorithm against the expert manual segmentation. At the end of this process, the experts decided that the results of the algorithm are better than that of the expert, adjusting the expert segmentation results to match that of the algorithm. The resulting modified expert segmentation is then used to make the quantitative validation of the automated segmentation.

3.2.2 Evaluation and validation of SEP

Following the validation approaches in previous research would imply that each module of the SEP needs to be validated separately with a different method. However, given the number of modules in the SEP, the ideal solution would be a single validation methodology by which the individual module can be evaluated during development and the SEP, in its entirety, can be validated.

As mentioned before, the problem with using manual verification is that, since there are only two dimensions on each slice that are known, the motion in the third dimension cannot be verified. In addition, manual verification or validation is subjective in its nature. This limitation makes the use of a physical simulation model, like a gel phantom, a better verification approach. However, since the use of a physical simulation model simplifies the geometry to be a simple doughnut shaped object, it limits the complexities that an algorithm would need to deal with in the validation phase. The remaining approach of using mathematical

3.2 Evaluation and validation of results

simulation is not the obvious choice for validating segmentation. However, the simulation of the various inputs and conditions is the most versatile validation approach with the capability to fulfil the validation requirements of the different modules.

In addition, the creation and validation of the SEP and its evaluation can be thought of as a single problem with dual domains and the use of simulation solves both problems of validation and evaluation of the SEP. To that end, a simple mathematical model is simulated along with tag planes that intersect the model as would be induced in tMRI. Forces are applied to deform the model and in turn the tag planes, so that virtual tMRI slices depicting the moving volume can be acquired. The resulting regional strains as calculated by the SEP are compared against those of the simulated deforming mathematical model. This approach is followed for each module of the SEP as will be explained in detail later. This approach will isolate the errors resulting from a given module of the SEP from those caused by the anatomy, medical conditions, technology and associated noise as well as the other modules of the SEP. When the results from the SEP are acceptable for the simulated model, it can be applied to the medical images of the LV.

As seen in figure 3.22, domain one is the creation and validation of the SEP using simulation and calculates the deformation or regional motion based on the forces applied. Domain two is the evaluation of the SEP, calculating and comparing the strain resulting from the deformation of the simulation against the regional strain pattern output by the SEP. The strain patterns from the two domains can be compared against the other to calculate the achievable accuracy of the pipeline and possibly that of the different constituent algorithms used during the creation of the SEP.

The steps of the methodology are shown in figure 1.3 as seen in Chapter 1. A simulation based approach also allows for the qualitative comparison of various motion estimation algorithms against each other. It allows the simulation of the different tMRI acquisition options to test and compare in terms of the accuracy that can be achieved when processed by the SEP. The acquisition options to be tested include the axes along which the object is to be imaged, the number of phases that need to be acquired, the number of slices to be acquired along

3.2 Evaluation and validation of results

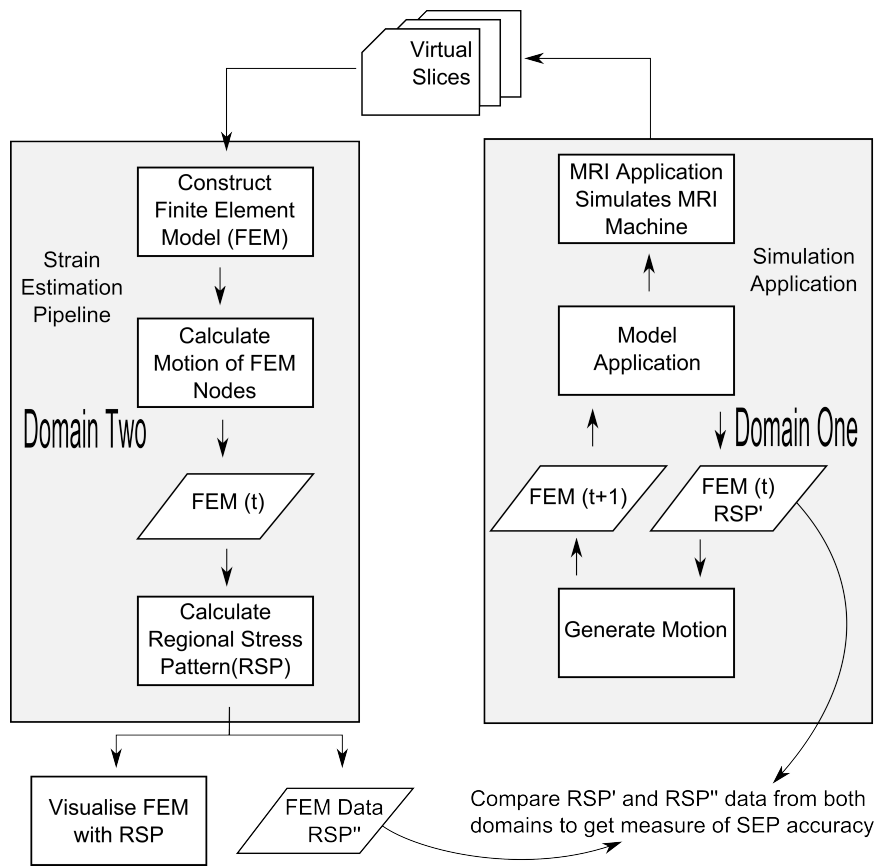


Figure 3.22: Validating the SEP

3.3 Implemented software tool chain

each axis, the distance between the slices, the space between tag lines and the tag pattern used. This is not normally possible in a medical environment since the acquisition properties are restricted by the physical constraints of the MRI machine. The simulation would, thus, help to find the conditions that would result in better accuracy in the event of improved hardware, etc. The combination of acquisition options that result in an acceptable accuracy level may also be considered important in the pipeline evaluation. An additional function of the evaluation process would be to find the individual parameters or the combination of parameters that will result in the highest regional motion estimation accuracy. The validation of the SEP, on the other hand, involves the quantification of its error-proneness and an appropriate sensitivity analysis method. Thus, using simulation and splitting the problem into the two domains, the SEP is implemented and the accuracy that can be achieved using various different algorithms in the SEP can be calculated. Although the initial focus of the research is the creation of a SEP prototype, subsequent development of the prototype will critically investigate the different reconstruction methods in terms of reconstruction accuracy.

3.3 Implemented software tool chain

The first step in the project is to simulate the tMRI dataset which, as seen on the right section of figure 3.23, is done using a number of tools.

3.3.1 ‘Extract Features’

The final result of the Segmentation module has been defined as the Virtual Slice(VS). A VS of a given time phase describes the inside and outside contours, represented as two closed lines, and the tag lines, represented by multiple open lines, is discussed further in Chapter 4.

Given that the aim of the research is to build an accurate motion reconstruction and strain distribution model of the cardiac tissue, the method of the segmentation needs to produce reliable and accurate results in order to minimise

3.3 Implemented software tool chain

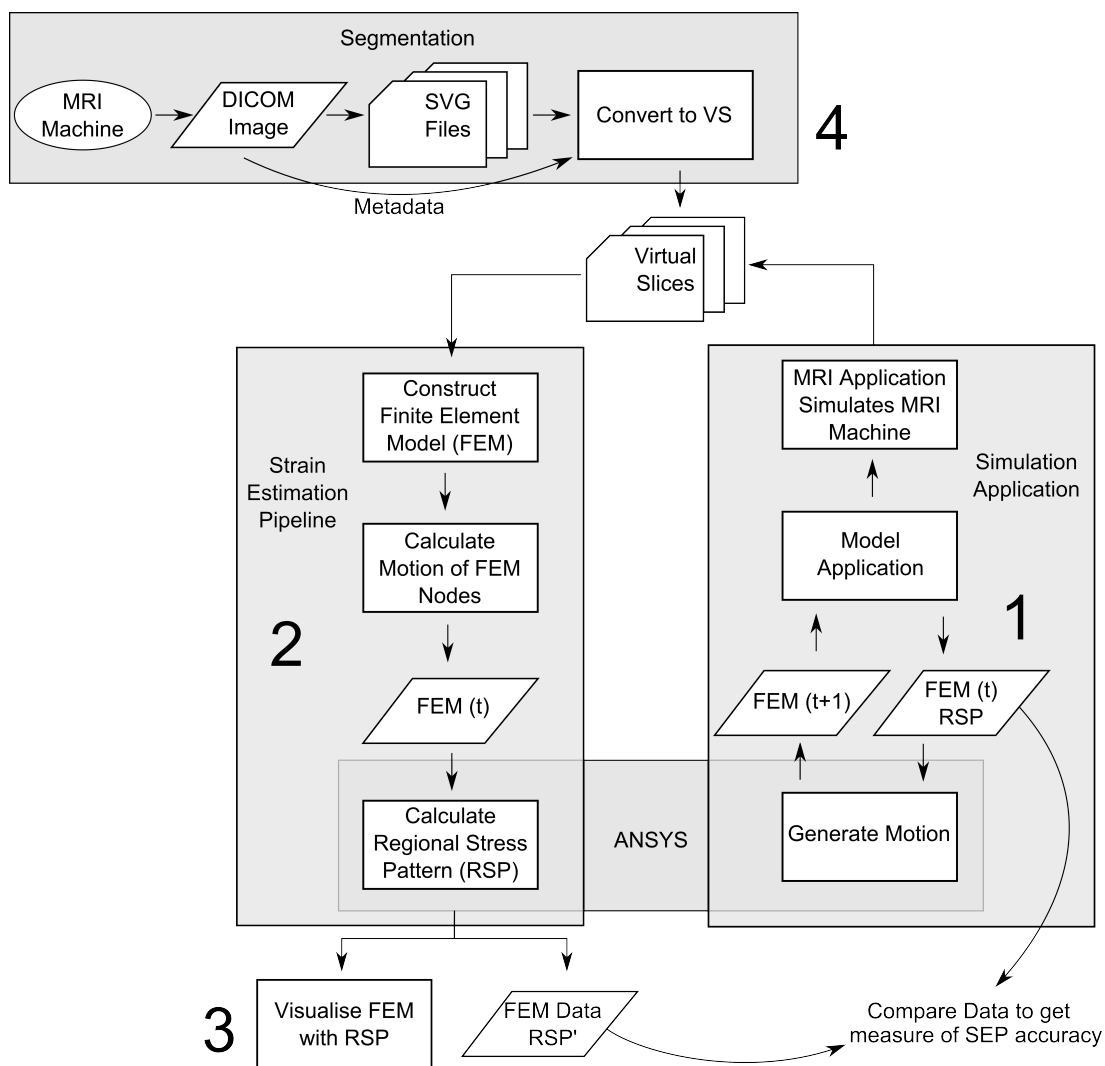


Figure 3.23: Software tool chain

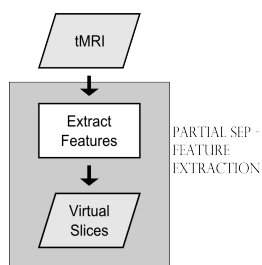


Figure 3.24: Data flow when extracting features from tMRI dataset

3.3 Implemented software tool chain

the error of the final result. It is for this reason that the semi-automatic algorithms were abandoned in favour of manual segmentation despite its labour intensive nature.

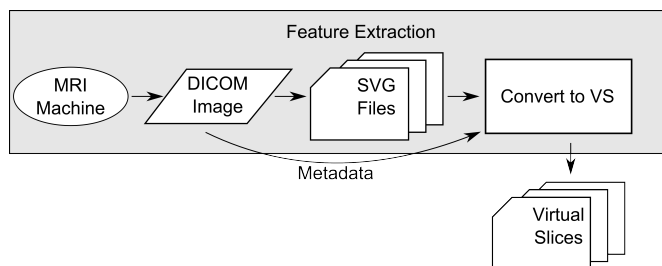


Figure 3.25: Segmentation software tool chain
used to segment tMRI dataset

The problem of manually segmenting the tMRI dataset is tackled over a number of stages, as shown in figure 3.25. The first step is to convert the tMRI slices from its native DICOM format to jpeg format so that it can be modified by an off-the-shelf paint application if needed. Since the output of the segmentation module needs to be in the intermediate VS format, these jpeg files are imported to a Scalable Vector Graphics (svg) file that facilitates storing the image along with any segmented information as lines or lists of connected points, as seen in figure 3.26.

The ‘Segment Stack’ module involves the conversion of the tMRI slices into the required VS format. Since one of the biggest problems when segmenting tMRI dataset is the low resolution (208 x 256) of the image slices, the derived jpeg images are scaled before importing them into the svg files for segmenting. Once the chamber walls and tagged tissue lines are identified, the svg data is scaled to the original dimensions, aligned and parsed together with the DICOM header information to create the required Virtual Slices using a Python script.

3.3.2 ‘Create FEM’

The input of the ‘Create FEM’ module has been defined to be the VS while the final result of the module is the list of nodes and elements along with the forces

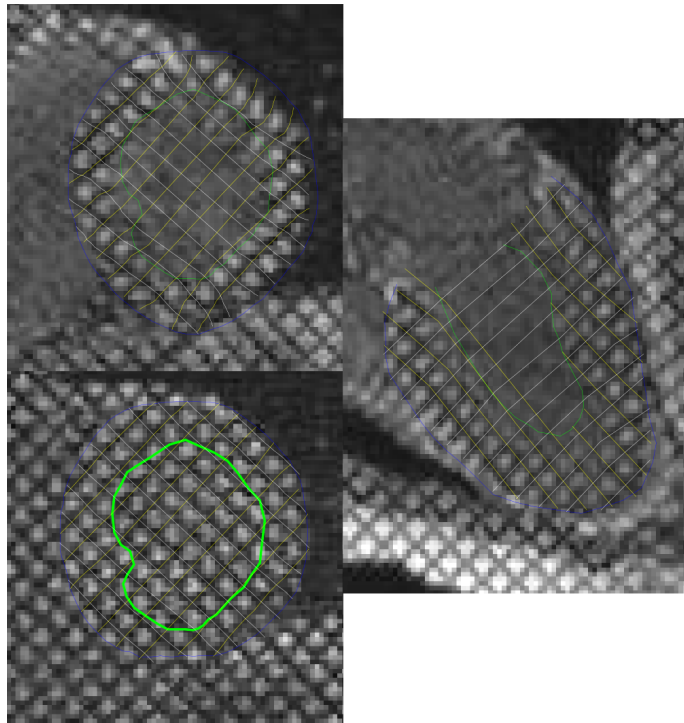


Figure 3.26: Segmented slices in scalable vector graphics (SVG)

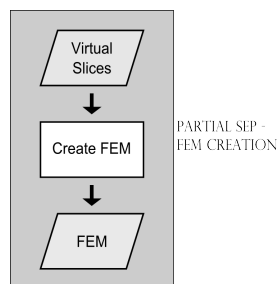


Figure 3.27: Data flow to create FEM

3.3 Implemented software tool chain

in the required ANSYS format.

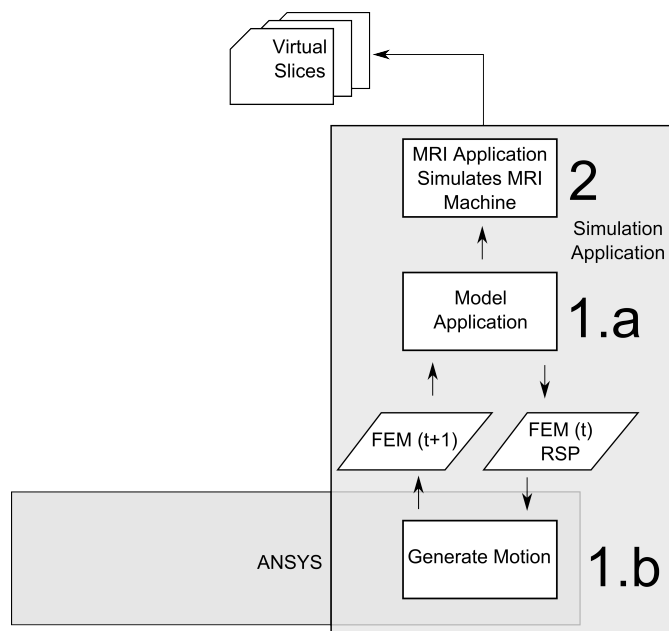


Figure 3.28: Software tool chain to create FEM

At the initial timestep the mathematical model along with the tag planes information is generated in the format required by ANSYS along with any forces that are to be applied to the FEM. The model is deformed by the forces applied to it by ANSYS and returned to the program that simulates the tMRI acquisition. Repeating this process over a number of timesteps generates the Virtual Slices, which are then put through the SEP - creating a FEM, estimating the motion of the thus created FEM and calculating the strain values using ANSYS. In order to validate the SEP the resultant FEM is compared to the simulated FEM using Matlab code. The details of the various stages are discussed in the following chapters. Chapter 4 explains the process of acquiring the simulating tMRI data to use to validate the SEP. This is followed by the details of the validation of the SEP in Chapter 5 and the use of the validated SEP to process the tMRI data in Chapter 6.

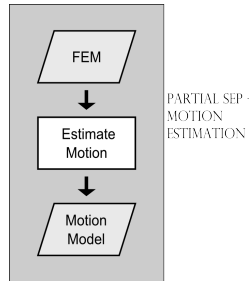


Figure 3.29: Data flow to estimate motion

3.3.3 ‘Estimate Motion’

The tag line information from the VS are used to create the motion cloud and the node list from the ANSYS FEM file are used to query the motion cloud. Thus, the ‘Estimate Motion’ module uses the output FEM file generated by ANSYS and the VS as inputs as shown in figure 3.30. The module outputs the motion of each node of the FEM as a node modification file in the format dictated by ANSYS.

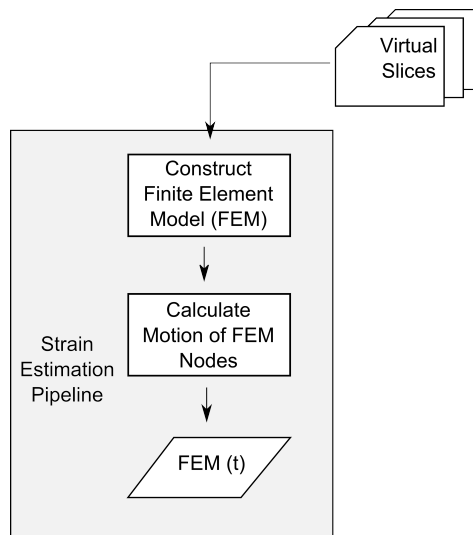


Figure 3.30: Software tool chain used to estimate motion of FEM

3.3.4 'Calculate Strain'

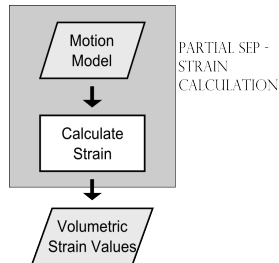


Figure 3.31: Data flow to calculate strain

The 'Calculate Strain' module takes as its input the node modification files output by the 'Estimate Motion' module and in turn generates the FEM node strain file as shown in figure 3.31.

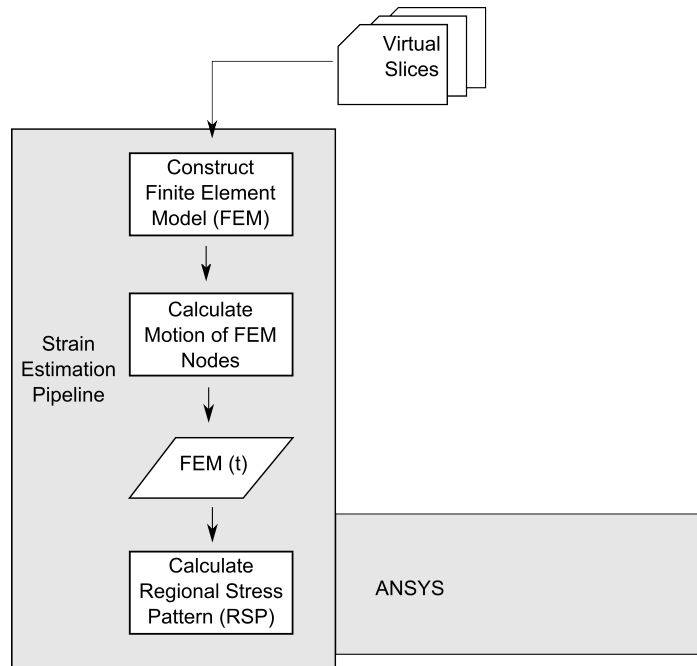


Figure 3.32: Software tool chain used to calculate regional strain of FEM

3.4 Chapter summary

This chapter discusses the process of converting the tMRI slices into the desired regional strain model along with an analysis of the existing research. The details of the procedure that will be followed to process the tMRI in this project, called the Strain Estimation Pipeline or SEP, are also introduced here. The main processes that are identified are the segmentation of the image slice, the creation of a FEM based on this segmented information, followed by the estimation of motion of the FEM and finally the calculation of the strain of the FEM.

This is followed by the details of how the SEP and its modules are implemented and the tool chain used in the project. The final section is a discussion of the various validation approaches followed in the past research and the simulation approach by which the SEP and its results are validated. The concepts introduced in this Chapter of the SEP, evaluation and validation are discussed in more detail in Chapters 4 and Chapter 5. Chapter 4 further details the development of the SEP and the simulation that is used to evaluate the modules of the SEP, while Chapter 5 discusses the validation of the SEP and its use in processing tMRI data.

4

Developing a Strain Estimation Pipeline

Due to the nature of in-vivo tMRI imaging, it is impossible to test the accuracy of the results of the SEP without extra data like that of real implants or gadolinium images that it may be matched against. It is however possible to test the accuracy of the SEP by simulating the expected tMRI input. This chapter covers the details of the simulation technique used to develop the SEP modules, test the motion estimation algorithms and validate the SEP as shown in figure 4.1.

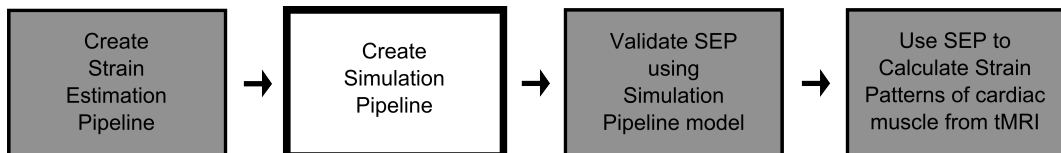


Figure 4.1: Research stage: simulation pipeline

As explained in the previous chapter, the SEP needs to be tested and its results validated during its creation before it can be used with confidence. It would also be ideal if the error in the calculated stress model can be minimised during this process. As briefly mentioned in the previous chapter, both the creation of the SEP and validation of the outputs can be achieved by considering them as two sides to the same problem. The proposed solution of simulating a tMRI dataset allows both testing the SEP during creation and validating its results. Using this

approach the accuracy of the SEP is measured by comparing the simulated stress distribution (that result in the simulated tMRI) against those estimated by the SEP.

Simulating the tMRI data involves a number of steps that are discussed in detail through the chapter. The first is the generation of a simple mathematically defined volume and inducing virtual tag planes in the volume. The next step is the application of forces to deform the defined model and finally the acquisition of a virtual slice of this simulated volume.

The last section details the evaluation and refining of the SEP as part of its development process, with each module of the SEP individually tuned to maximise the accuracy of its individual and overall output. This ensures that the error in the output from the previous module in the SEP will not affect the development and accuracy of the next module and thus the final result.

4.1 Overview of simulation pipeline

The mathematical model, tag planes and forces to be applied are generated from a set of user defined parameters. The mathematical model is generated and represented as a FEM in ANSYS (with the virtual tag planes integrated into the FEM). The forces are then applied to the nodes of the model using ANSYS, at each time step and the results stored. Image slices are then acquired at user defined positions of the volume for each time step. The stages of the simulation can be seen clearly in the figure 4.2. As shown in the figure, the simulation of the Virtual Slices(VS) can easily be split into the main modules of ‘Build Model’, ‘Apply Forces using ANSYS’ and ‘Acquire Virtual Slices’.

Each of the main modules of the simulation that finally result in the VS, have data outputs that can be used in the development of the SEP as seen clearly in the figure. During the development of the SEP it is thus possible to give each module a simulated input of maximum possible accuracy rather than an input that resulted from the previous module in the SEP. This approach will assist the development since we can be sure that any errors found after the processing of data are a result of the module under development and not a cumulative error.

4.1 Overview of simulation pipeline

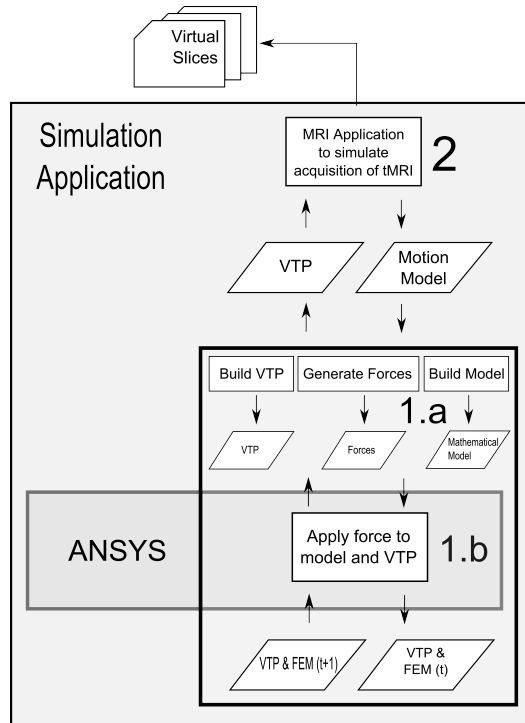


Figure 4.2: ‘Virtual Slice’ simulation

Table 4.1: Overview of Simulation Pipeline processes

1. Generate mathematical model based on user options
2. Generate forces to deform mathematical model
3. Generate Tag planes
4. Produce ANSYS FEM (input) file
(Integrated mathematical model and tag planes)
5. Produce ANSYS Force file
6. For each required time step
 6. 1. Acquire all required slices
 6. 2. Sort the list of MC points in increasing distance from the node
 6. 3. Use ANSYS to generate output FEM file
 6. 4. Read FEM file output from ANSYS
 6. 5. Update MathModel
 6. 6. Update TagPlanes
7. Generate node modification file for ANSYS

4.2 Generating the mathematical model

The first step in the simulation of tMRI requires the generation of a simple mathematically defined volume and inducing virtual tag planes (VTP) to reflect the deformation of the model.

The literature discussed in Chapter 3 shows that research groups use fairly complex geometry, combining volumetric representations to model the ventricle more accurately. Past research also shows that the motion of the apex is difficult to track and that this is most likely due to a combination of the geometry and the global motion of the heart within the thoracic chamber. It is for this reason that a conical volume is chosen over a hemispherical or prolate hemispherical volume. The simple mathematical model may provide or exacerbate some of the complexities caused by the shape of the chamber and thereby making the motion estimation module inherently tuned for it.

4.2.1 Creating the FEM

The two approaches considered in defining the conical volume, was the use of a swept volume or that of a set of discrete points. Although the use of a swept volume will result in a truer representation it is computationally more expensive than using a point mesh. In addition, using a point mesh also makes the definition of the FEM easier. This approach also makes it easier to modify the geometry, into one that models the LV geometry more closely, in the future if and when required.

4.2.1.1 Defining the conical volume

A cone can be thought of as a set of circles the diameters of which decreases towards the pinnacle. A conical volume in turn can be defined as a set of cones that lie along the same axis with increasing diameter and height as seen in figure 4.3. The points of a conical volume can be organised according to the distance from the base (level), the rotational angle of the point on a circle (sector) and the radius or diameter of the cone (ring). The model will resemble a cone more closely as the number of sector values increase as seen in figure 4.4.

4.2 Generating the mathematical model

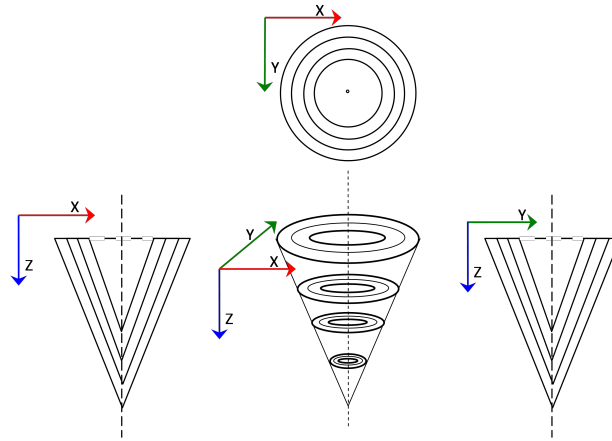


Figure 4.3: Conical volume definition

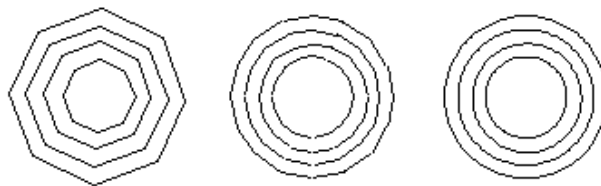


Figure 4.4: Cross-section of conical volume changes with number of sectors

4.2 Generating the mathematical model

The points of the conical volume can be defined in a Cartesian coordinate system with the axis of the cone lying along the z axis and base on the x-y plane, as in figure 4.3.

Thus, the z value of a point of the cone denotes the distance from the base, while the x and y values denotes the ring and the position along the ring or sector of the cone. More information on the representation can be found in Appendix B.

4.2.1.2 Finite Element Model

Once the geometry is created, it is then meshed into ‘nodes’ and ‘elements’ as required by ANSYS. Although there are a number of possible element types to model solid structures in ANSYS, the SOLID185 3D structural solid is used since each of the eight nodes of an element has the required three degrees of freedom. The meshing into nodes and elements can be seen in figure 4.5. As seen in the

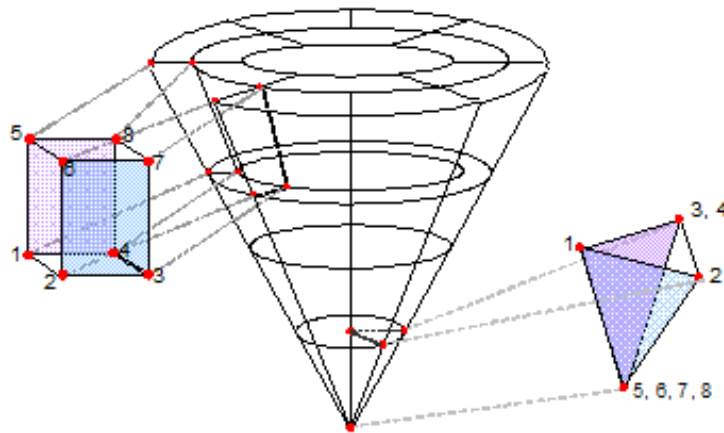


Figure 4.5: Conical simulation volume
ANSYS Solid185 element definition

figure, the conical tip of the model or the apex of the LV is modelled (using the SOLID185 element) with four of the nodes pointing to the same location to avoid multiple element types in the model.

4.2.2 Creating the ‘Virtual Tag Planes’

A VTP needs to be defined as a surface to capture the three dimensional motion information of the model closely mimicking tissue tags. The most commonly used representations of surfaces are polygon mesh surfaces, parametric surfaces and quadric surfaces. Quadric surfaces are best used to represent surfaces that can be mathematically defined by quadratic equations like the familiar spheres, ellipsoids and cylinders. It was thus not considered appropriate since a VTP is unlikely to easily fit an implicit equation. The choice of parametric surfaces would provide an accurate representation but algorithms working with it will be more complex than using the less accurate polygon mesh surface. Despite the reduced accuracy provided by polygon meshes, it is used to model VTPs since accuracy can be improved by increasing the number of points used in the mesh.

4.2.2.1 Defining the VTP

VTPs may initially be thought of as a collection of points on a plane but with the passage of time the points that form a VTP move so that this may no longer be true. The motion of the points will result in a deforming surface rather than a plane in contrast with the term VTP.

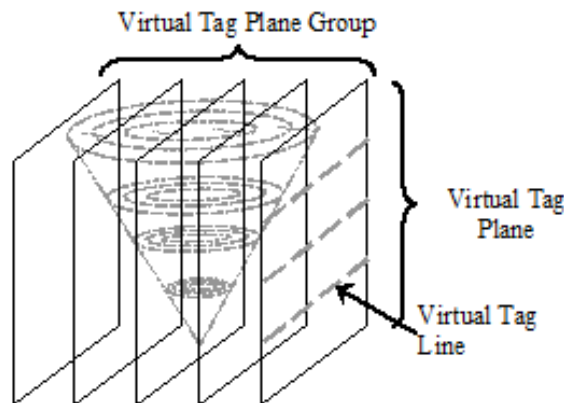


Figure 4.6: Virtual tag plane definition

VTPs that initially have the same normal or orientation are grouped together. A VTP is organised into a list of lines, called ‘virtual tagged line’ (VTL), which

4.2 Generating the mathematical model

in turn is defined as a list of points. The representation of the VTP can be seen more clearly in figure 4.6. The position of a point in a VTL is calculated as the intersection of the line with the model volume. The behaviour of the points of each VTL and of every VTL of a VTP is independent of the other but dependent on the nodes of the model.

4.2.2.2 Intersections with the mathematical model

The points that make a VTP are calculated as the intersection of the plane in its initial state with the polygon mesh representing the conical volume. Since it is computationally less expensive to calculate the intersection of a line against the model, the intersection of the VTLs and the model are calculated, taking advantage of the representation of the VTP.

4.2.2.3 Identifying influencing nodes

The nodes of the FEM that are used in the calculation of the points of a VTL are in effect those that are closest to the VTP. It is important to keep track of the '*influencing*' nodes since they dictate the position of the intersection points that define a VTL and thus the motion of the VTP through time. These nodes are thus used when integrating the VTP into a FEM to ensure that the motion of the VTP is accurate. Each point of a VTL can have up to eight influencing nodes depending on its proximity to the edges of the model as shown in figure 4.7.

The integration of the VTP into the ANSYS FEM is done by using linking elements between each point of the VTPs with each of the identified influencing nodes. The connections between an influencing node and a VTL point is modelled using a LINK180 element, which is a structural element that provide the necessary degrees of freedom, with the same material property that is used to model the SOLID185 elements as seen in figure 4.7.

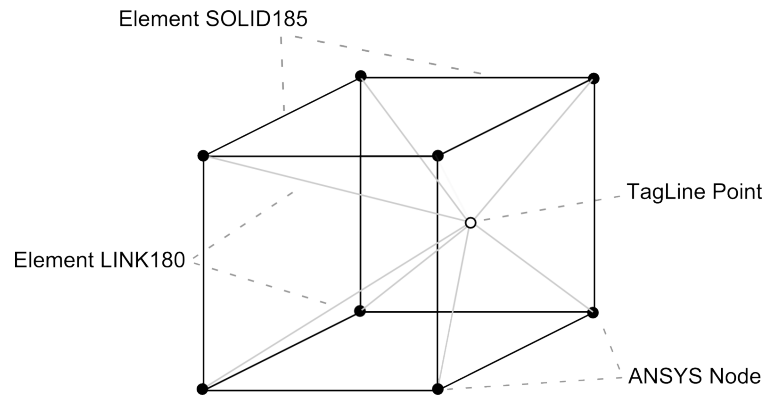


Figure 4.7: VTP points (LINK180) and influencing nodes (SOLID185)

4.3 Motion model simulation

The LV is known to create its pumping action by the reduction of its chamber volume. It is also known that the roll of muscle moves from the apex towards the base while also moving towards the centre of the chamber. This motion is simulated by splitting the complex motion. The normal motion and deformation of the heart is split into a twisting deformation, a radial contraction and a longitudinal contraction. The motion model simulation can recreate conditions of both the normal and abnormal motion of the LV.

4.3.1 Deforming forces

The efficient pumping action of the heart chamber is generated by the gradual reduction of the volume of the chamber from the apex towards the base. In the simulation, this volume reduction is replicated by a combination of the twisting of the chamber and motion of the chamber from the apex towards the base. The twisting or wringing motion of the chamber enables the muscle tissue to reduce the chamber volume thus producing the required pumping from the bottom up. Although there is a reduction in muscle volume it is important to note that according to Rodriguez [REW06] there is no more than a 4% reduction in the wall volume. Thus, simulating the regular motion of the heart wall chamber

requires forces acting in the radial, longitudinal and circumferential directions to be applied to the set of points of the FEM.

A twisting deformation can be generated by applying tangential forces to the inner and outer surfaces in opposing directions. The required radial contraction can be mimicked by applying radial forces acting towards the central axis of the volume and the longitudinal contraction by forces whose value decreases towards the base of the model. This can be seen more clearly in figure 4.8.

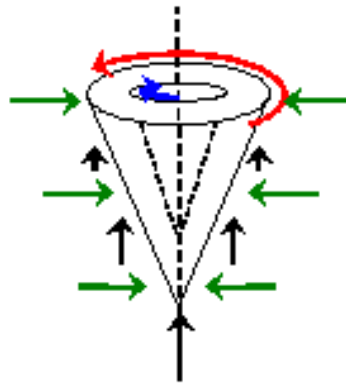


Figure 4.8: Forces to mimic motion of heart

The magnitude of the forces to be applied to the model depends on the required extent of deformation and is varied to assess the sensitivity of the pipeline. Each of the types of full volume forces can be applied with a temporal and spatial gradient along the surface and through the volume of the model to mimic the normal motion of the chamber.

Abnormal local motion of the model is simulated either by the lack of forces in a region of the volume or applying unbalanced regional forces.

Figure 4.9 shows a regional force acting on the node indicated in white and the neighbouring nodes that will be affected are indicated in grey. These regional forces can also be applied with a temporal and spatial gradient and along the surface as well as through the volume to simulate heart disease conditions.

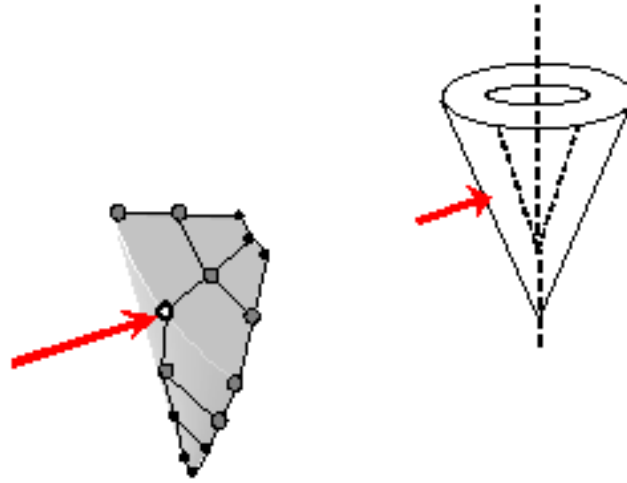


Figure 4.9: Regional force

4.3.2 Application of forces

The forces that deform the model are applied using the FEM package ANSYS. The required forces are presented as a list to be applied at the various nodes of the FEM.

The motion of the VTP is a result of the forces applied by ANSYS since the points that form the VTLs that form the VTPs are connected to the FEM. It may be noted that the connections have material properties that may influence the movement of the FEM due to the extra connections to nodes. The effect may not be negligible but it does not affect the intent of the simulation since it is from the same point in the simulation creation (from the same motion model) that the VS are acquired and the strain patterns of the simulation are calculated. The internal structure of the simulation is immaterial to the ultimate outcome of creating and validating the SEP.

4.4 Acquisition of ‘Virtual Slices’

The VS represents the intersection of the acquisition plane against the VTPs, the inside wall and the outside wall of the model. The positions of the acquisition planes are defined by the user and thus, the acquisition of the VS involves

calculating the positions at which the acquisition plane intersects the chamber model walls and the VTPs that are initially orthogonal to it. As explained earlier, tMRI slices are acquired with tag planes induced along axes that are orthogonal to each other. A stack of these tMRI slices, 6mm apart, will image the entire chamber. The distance between the VTP will be in the range of 6-8mm to mimic the conditions of tMRI and the VS are acquired between the range of 10 - 20 time steps or phases.

VS are also acquired with varying the numbers of the phases, the distance between the VTPs and the number of slices in a stack in order to explore the possibility of optimal conditions as well as assess the sensitivity of the Motion Estimation method.

The representation of the VS as a list of lines will mean that we can avoid the additional step of segmentation when testing the SEP. This is useful during development since segmentation is known to be the most error-prone process.

4.4.1 Acquisition coordinate axes and planes

As mentioned briefly, the long axis is defined as the axis that passes through the centre of the apex of the model and runs through the centre of LV the chamber volume. The short axes are defined as the two axes that are orthogonal to the long axis and each other. In this project, the acquired long axis slices will be rotated around the long axis as shown in figure 4.10. The distance between consecutive short axis slices will be between 5 - 8mm and the angle between consecutive long axis images varies between $30^\circ - 40^\circ$ as per tMRI specifications.

The acquired VS need to be in a coordinate system having three orthogonal axes to reconstruct the complete motion of the model. A Polar coordinate system is chosen since it provides more uniform richness of motion information, although a Cartesian coordinate system is also applicable. The VS is acquired to view the tag lines along two short axes and the long axis. The short axis slices image two sets of tag planes in perpendicular directions on the same plane while the long axis slice is orthogonal to the two short axis slices as shown in figure 4.11. Thus, the VTP are induced in the myocardial tissue using a Cartesian coordinate system and the virtual image slices are acquired following a Polar coordinate system.

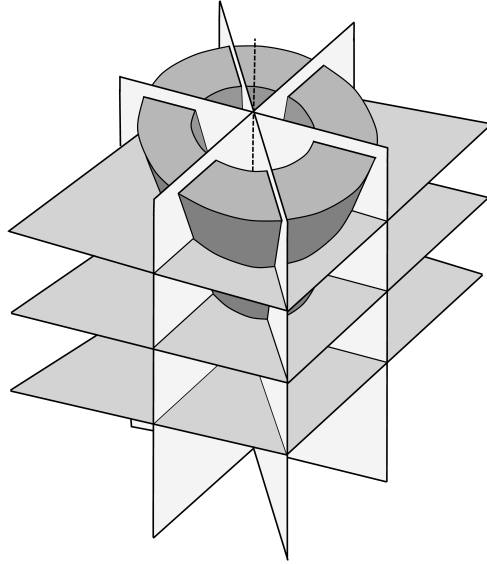


Figure 4.10: Planes of acquiring simulated tMRI slices of mathematical model

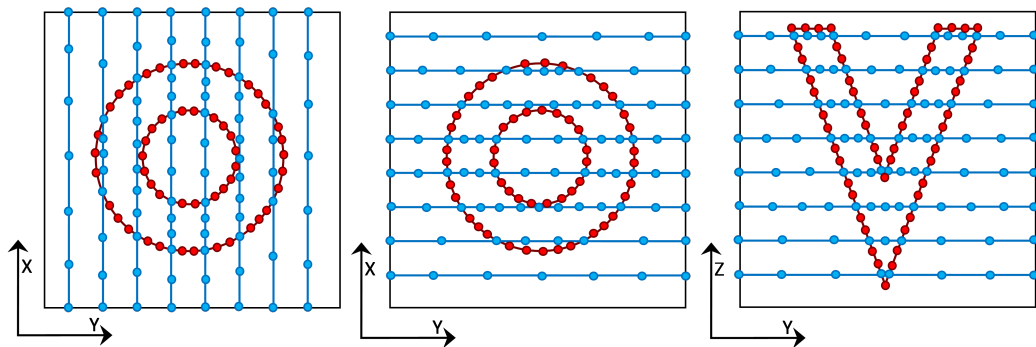


Figure 4.11: Sample of virtual tMRI slices that will be acquired

4.4.2 Acquiring VTP information

Acquiring the VTP information involves calculating the intersection of the acquisition plane against each VTP. The first type of intersection is when a VTL lies on the acquisition plane and the second when the acquisition plane lies in between two VTLs. While finding the intersection points in the first case is trivial, in the second case the positions of the points defining a virtual tag are calculated as the intersection of the line formed by corresponding points on two VTLs and the acquisition plane as seen in figure 4.12.

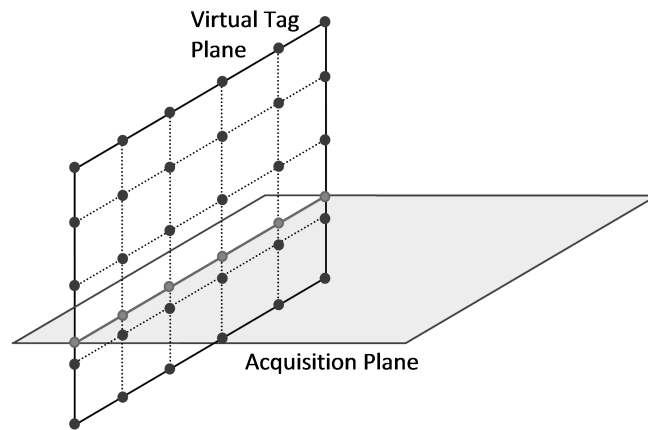


Figure 4.12: Virtual tag line
calculation of intersections

The VTP information can be acquired to form tag lines or grids on the VS, as is the case with tMRI. Acquisition of tag grids would have the additional requirement of storing the intersection points of the VTP, which is a simple case of calculating the intersection of two lines.

4.4.3 Acquiring model wall contour information

Acquiring the model wall contour information involves finding the intersection of the inside and outside surfaces of the model with the acquisition plane. This is fairly straightforward due to the representation of the model. Once the level or

the levels of the model that are closest to the acquisition plane are found, it is the simple case of finding the intersection of the line formed by adjacent points along the surface and the acquisition plane as shown clearly in figure 4.13.

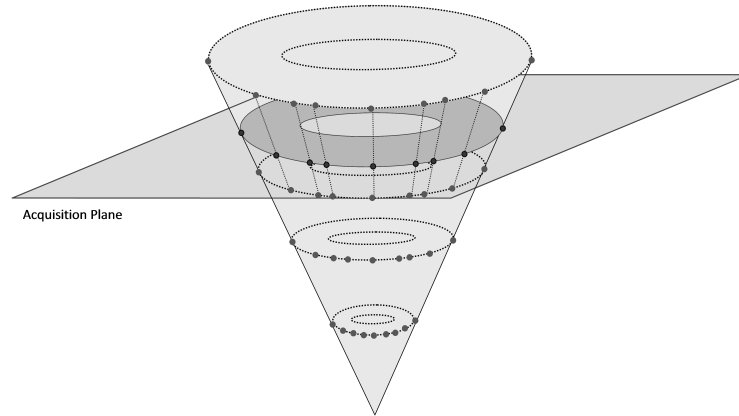


Figure 4.13: Model wall contour
calculation of intersections

4.5 Developing the SEP modules

The SEP is developed in reverse to allow the tandem development of the SEP and the simulation pipeline. As seen in figure 4.14, the SEP and the simulation pipeline are opposite processes, with one creating a mathematical model from tMRI slices and the other creating virtual tMRI slices from a mathematical model. With this in mind, both the simulation pipeline and the SEP have been designed to have the same intermediate data formats, making it possible to use the intermediate outputs of the simulation pipeline as inputs to appropriate SEP modules during the development phase to allow for testing, evaluation and validation of the SEP modules.

Using the intermediate data of the simulation pipeline allows each individual module of the SEP to be tested and refined before evaluating its performance as part of the SEP. Once the SEP in its entirety is created, the SEP is further refined

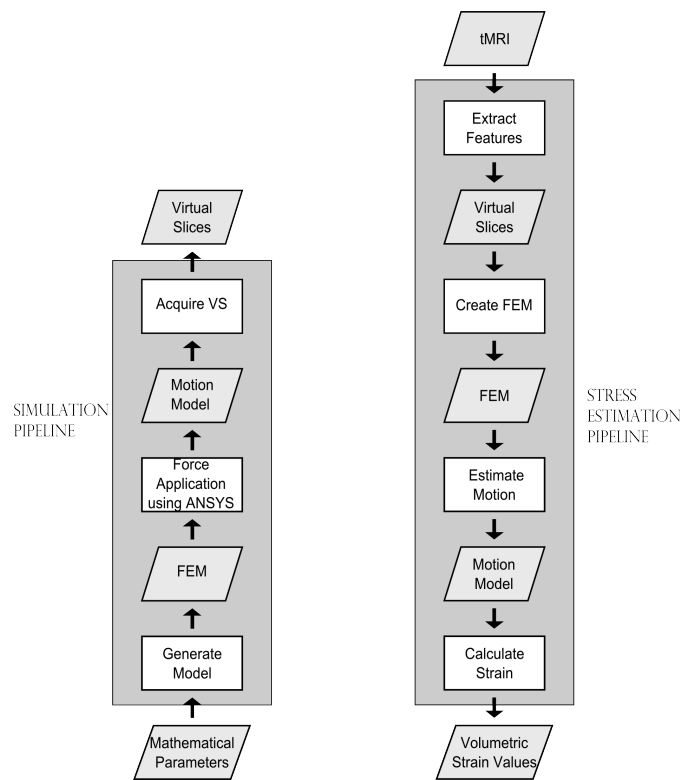


Figure 4.14: Validating the SEP

to maximise the accuracy and to find the individual parameters or the combination of parameters that will result in the highest regional motion estimation accuracy.

4.5.1 ‘Calculate Strain’

As evident from figure 4.15, the ‘Calculate Strain’ module of the SEP can use the intermediate *motion model* data of the simulation pipeline as its input during development and evaluation. The ANSYS process by which the strain pattern of the model is calculated does not need to be evaluated or validated since this is the operation available from the ANSYS package. Additionally, since there is only one way to calculate strain using ANSYS, the SEP module cannot be checked in an unbiased manner since it is the same operation used in the simulation pipeline. The only possible comparison that can be made would be by varying the material properties of the FEM, which allows us to gauge how much the material property values influence the calculated strain.

The reason why this is an interesting comparison is that in addition to quantifying the strain of a region, it is clinically useful to clearly identify areas of either high or low strain against the mid-range values which most of the tissue will display. Thus, it is important to identify areas that may have drastically increased or reduced strain to its surroundings to mark areas for exploration of abnormal function. It is for this reason that the strain values are calculated for the FEM with the same motion but different material properties (within the range that can be expected of tissue). It is important to note that this may result in false positives and so when quantifying the regional strain the closest match to the material properties of the cardiac tissue is used. Thus, the evaluation of the ‘Calculate Strain’ module involves the comparison of the calculated strain values for the FEM with the same motion but different material properties.

The details of the forces that deform the simulation model can be found in section 4.3.1 with the magnitude of the applied forces arrived at by a process of trial and error. As a result, when arriving at the simulation models used for the validation of the SEP there were instances when the combination of forces applied and material properties of the simulated model resulted in visually insignificant

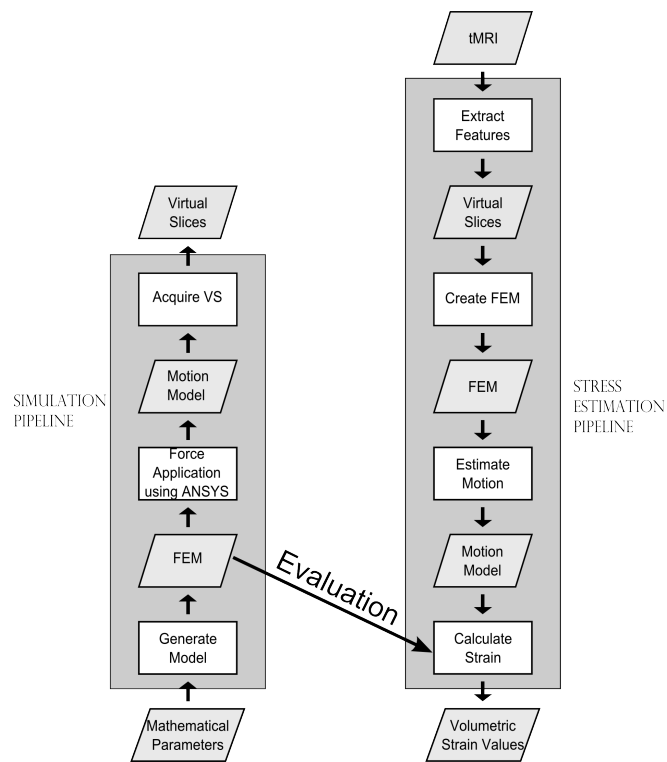


Figure 4.15: Evaluation of 'Calculate Strain' using simulation data

motion and limited strain values. This was dealt with by increasing the magnitude of the forces applied to the simulated mathematical model, reducing the elasticity of its solid or a combination of both.

4.5.2 ‘Estimate Motion’

The ‘Estimate Motion’ module requires information of both the FEM and the tag lines in order to validate its output. As seen in figure 4.16, the validation of the process uses the intermediate mathematical model, output of the ‘Generate Model’ module, as well as the extracted tag line information from the generated VS, output of the ‘Acquire VS’ module.

To evaluate and check the accuracy of its algorithm, the output of the ‘Estimate Motion’ module is first compared to the input (the motion model) of the ‘Acquire VS’ module of the simulation pipeline. The next phase of the evaluation is to verify the output of the partial-SEP including the ‘Estimate Motion’ module, given the input of the VS as seen in figure 4.16. This is done by comparing the forces required to create the regional stress model output of the partial-SEP (including ‘Estimate Motion’), against the forces applied to the mathematical model in the simulation pipeline. Since the calculation of the regional stress pattern and the forces acting on the models employs the use of ANSYS for an identical operation on two separate motion models with possibly different material properties from two different sources (simulation pipeline and SEP), it is deemed to be acceptable to compare the two motion models instead of comparing the regional stress models or the forces acting on the models.

During the development phase the intent is to identify and test different approaches against each other to determine the best algorithm during the refining process and validation of the SEP as the focus of the SEP development is the algorithm used for motion estimation. As expected, the different approaches were identified as a result of dealing with complexities that came to light during the development of the basic motion estimation algorithm. One of the initial problems faced during the trial and error phase of the development was that the estimated motion of the nodes were found to be either insignificant or oscillating about their original location. To deal with this issue, the basic motion estimation algorithm

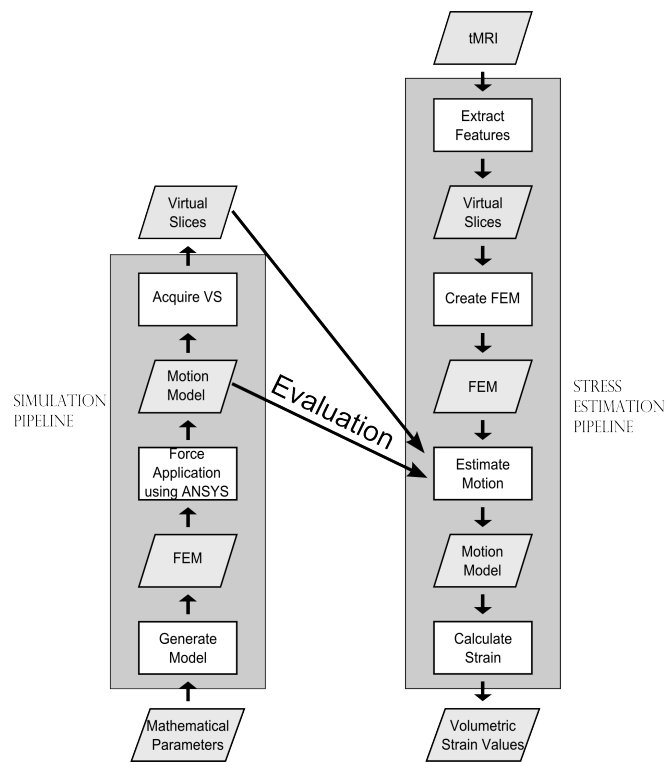


Figure 4.16: Evaluation of 'Estimate Motion' using simulation data

was first modified to reduce the influence of MC points based on its distance from the node, making the contribution of an MC point indirectly proportional to its distance from the node as described in algorithm 3.2. This in turn reduced the prevalence of oscillating points in the final result. The algorithm was then further modified to change the threshold conditions (distance or number) to allow for more contributing MC points, as described in algorithms 3.3 and 3.4, which in most cases resulted in an increase in the magnitude of the calculated movement of the nodes.

In addition to the issues faced by all the nodes of the model, there were special issues faced by the nodes close to or on the surface of the model. The first, was that these nodes were found to gravitate towards the centre of the model faster than expected. It was in dealing with this problem that the spatially aware selection of MC points was first trialled. As detailed in algorithm 3.5, the closest MC points in each quadrant are selected rather than merely selecting the closest MC points which helps to avoid inadvertent localisation as would be the case for nodes close to or on the surface of the model, where the chosen MC points would tend to be in the same quadrants as discussed in detail in Chapter 3.

The second issue faced by nodes close to or on the surface of the model is that they are susceptible to the influence of noise or spurious motion information. As widely documented in the literature to be likely caused by information from surrounding tissues, it is handled by adding a check in the algorithm to exclude any selected MC points that lie outside the model volume.

4.5.3 ‘Create FEM’

As seen in the figure 4.17, during development of the ‘Create FEM’ module the accuracy of its algorithm is tested by using as its input the VS that are the output of the ‘Acquire VS’ module of the simulation pipeline. To evaluate and check the accuracy of the ‘Create FEM’ algorithm, the output of the module is first compared to the input of the ‘Acquire VS’ module, i.e. the mathematical model (motion model at initial time step). The next phase of the evaluation is to verify the output of the partial-SEP, including the ‘Create FEM’ module, given the input of the simulation pipeline’s VSas seen in figure 4.17. As mentioned before, this

4.5 Developing the SEP modules

can be done by comparing the forces required to create the regional stress model output of the partial-SEP (including ‘Create FEM’), against the forces applied to the mathematical model in the simulation pipeline. However, as mentioned in the previous section, since the calculation of the regional stress pattern and the forces acting on the models employ the use of ANSYS for an identical operation on two separate motion models with different material properties from two different sources (simulation pipeline and SEP), it is acceptable to compare the two motion models instead of comparing the regional stress models or the forces acting on the two models.

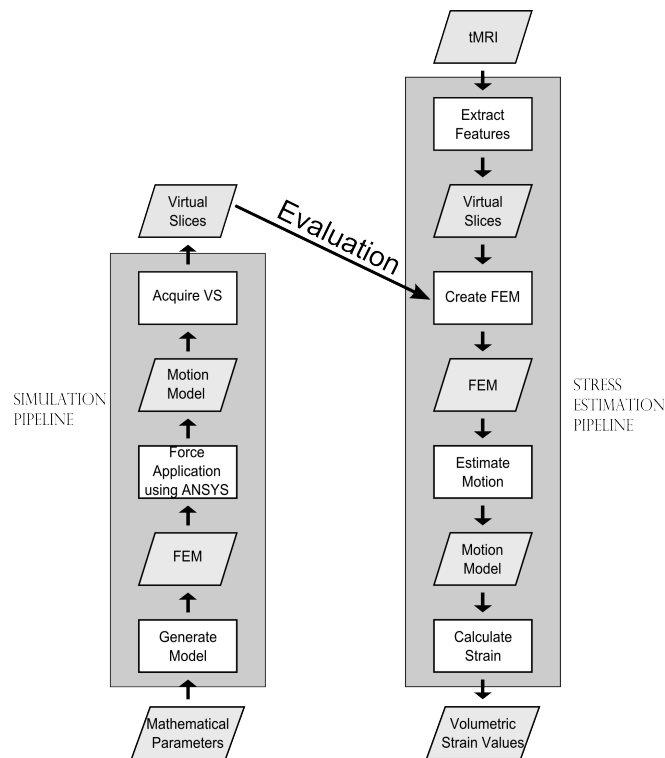


Figure 4.17: Evaluation of ‘Create FEM’ using simulation data

It is important to note that since the underlying structure in the simulation pipeline is a FEM, special care is taken to ensure that the existing FEM structure of the simulated input is ignored by the ‘Create FEM’ module during its development and evaluation. This is effectively done by changing the required

4.5 Developing the SEP modules

resolution of the ‘Create FEM’ output from the existing resolution of the simulation pipeline’s VS. In addition, it is important to disregard the solid type used in the simulation since this may influence the manner in which the FEM deforms.

During the evaluation phase, in order to identify if there is a change in the accuracy achieved based on the type of solid used in the simulation pipeline and the SEP, a number of different solid types and their degenerated forms are tested. This involves using ANSYS to apply forces to the FEM models created with the different solid types, checking if different solid types result in greater accuracy or respond in vastly different ways to that expected. The solid types that are explored include SOLID45, SOLID185, SOLID95 since these solid types have degenerated forms which allows for a uniform solid type throughout the model instead of different elements depending on the shape required. Degenerated forms of a solid are defined by specifying multiple vertices to be at the same physical point as seen in figure 4.5.

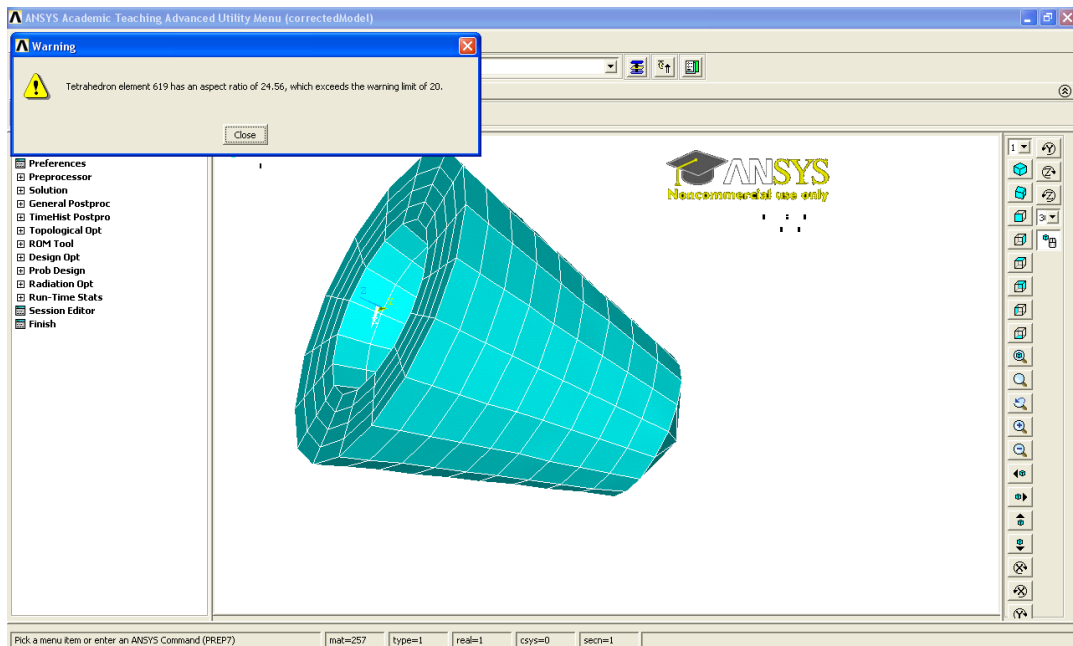


Figure 4.18: Results of refining
ANSYS shape errors - Jacobean matrix error

Although the creation of the FEM is automated it is only possible to evaluate

and validate the FEM once it is loaded into ANSYS and operations performed on the model. On loading a FEM into ANSYS, it is normal to face issues before a FEM is deemed stable enough to perform deforming operations and analysis. The first and most common issue is that a number of the elements used can be flagged as having illegal shapes causing a ‘Jacobian Matrix’ error as seen in figure 4.18. This was especially true of the tetrahedral elements at the tip of the cone caused by the angles created between the different faces of the elements. The problem in the tip of the model was averted by increasing the number of elements used in the tip. However, this modification in the algorithm was unsuccessful when the error was caused by elements in the remainder of the model. After modifying the algorithm to generate more elements and changing the shape of the elements with no success, the solution was finally found to be simply an increase in the scale of the model.

The other problem faced when loading the FEM in ANSYS is that despite successfully loading a model, it can collapse when forces are applied to it. The solution to this was found in the standard FEM procedure of increasing the number and/or magnitude of the constraints (restraining forces) to the ANSYS solution.

4.5.4 ‘Extract Features’

As seen in the figure 4.19, the development of the ‘Extract Features’ module does not use any output of the simulation pipeline for testing, unlike the other modules of the SEP. Although it is possible to simulate the tMRI stack, it was deemed unnecessary at the prototype stage since it is possible to visually evaluate the accuracy of a segmentation. As a result, the initial module of the SEP is not evaluated using any output of the simulation pipeline, intermediate or final. Instead, the evaluation of the ‘Extract Features’ module involved visually assessing and comparing the results of the different segmentation approaches that can be employed against the results of manually segmenting the wall contours and tag line information from a tMRI slice.

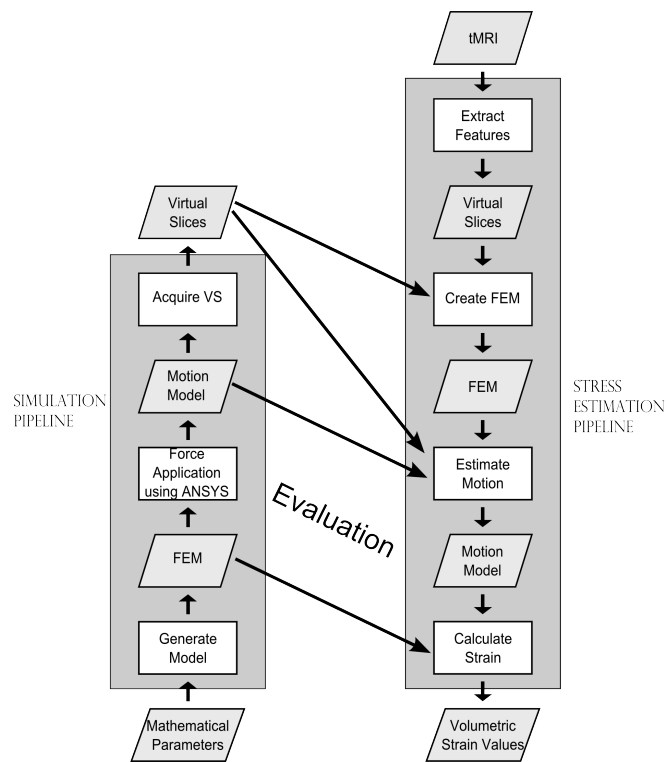


Figure 4.19: Evaluation of 'Extract Features' using simulation data

4.6 Chapter summary

This chapter discusses the development of the SEP. As elaborated in Chapter 3, the SEP is best evaluated using simulation. To that end, a simulation pipeline is used to create a mathematical model to evaluate the SEP and its result. The first four sections of this chapter discuss the simulation pipeline and the modules used to create the required mathematical model that can be used to evaluate the SEP.

The final section of the chapter discusses the development and evaluation of the different SEP modules. The development of the ‘Calculate Strain’, ‘Estimate Motion’ and ‘Create FEM’ modules are aided by the use of the VS and the intermediate outputs of the simulation pipeline. In contrast, the ‘Extract Features’ module is developed without the use of simulated data since a simple visual inspection of the module output against the input is possible to assess accuracy of the module.

This lays the ground for the next chapter which discusses both the validation process of the SEP and its results.

5

SEP Validation and Use

Once the SEP is developed and evaluated, it is validated using the simulated tMRI VS as input. As implied by figure 5.1, this chapter discusses the research stage that focuses on the validation of the SEP.

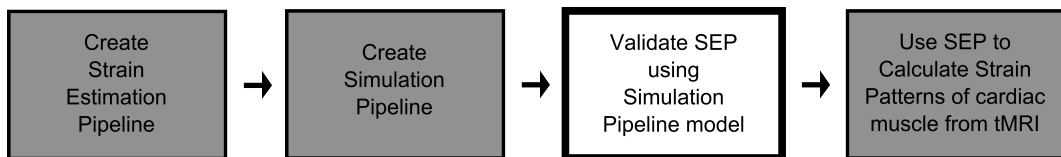


Figure 5.1: Research stage: validation

The first section details the methodology of the validation of the SEP. This includes a discussion of the possible methods of quantifying the effectiveness or accuracy of the SEP results, the different ‘Estimate Motion’ algorithms and the mathematical models to test the validity and efficacy of the SEP.

The remaining sections of the chapter analyse the results of the tests comparing the selected simulated model against the model created by the SEP.

5.1 Methodology of validation

Since the measure of error is integral to the methodology of the SEP validation this is the first topic to be discussed. The next topic of discussion is the ‘Estimate Motion’ module and the different algorithms and user options to be tested. This

is followed by a discussion of the simulation models that are designed to test and validate the SEP and variations of the motion estimation algorithms.

5.1.1 Measure of comparison

As discussed in Chapter 4, quantifying the accuracy of the SEP involves comparing its resultant model against the simulated model in order to quantify the difference between the two. Since the models are represented by the 3D positions of its nodes and the movement of the nodes are quantified by change in position, the x, y and z components will be compared. This requires that the identified method of measuring the likeness of the two models needs to be capable of handling a fair amount of data since there are approximately 400-800 elements and 10-20 time steps resulting in 4000-16000 element comparisons for each validation test run.

The root mean square deviation or root mean square error (rmse) is a frequently used measure of the differences between values predicted by a model and the values actually observed from the thing being modelled. As the name implies, rmse is calculated as the square root of the mean of the set of squares of the difference between the values of the two sets of data. Thus, a smaller rmse implies higher accuracy. The calculation is made in Matlab with separate values for each of the components of the position (x, y and z).

As mentioned before, this is a well established measure to calculate the difference between any two sets of data indicating the accuracy of the method. To enable easier comparison of rmse values generated from the different validation test runs, the values of each time step are plotted in a graph, where the time steps lie along the x-axis and the rmse values are along the y-axis.

5.1.2 ‘Estimate Motion’ algorithm variations

The primary aim of testing the different algorithms and user options of the ‘Estimate Motion’ module is to find the relative achievable accuracy of each algorithm. Thus, it involves comparing the results of various proposed algorithms against each other to find the algorithm with the best performance under different test situations.

The different variations to the module are organised according to the aspect of the module that is modified. In other words, the modifications that deal with the selection of MC points based on threshold conditions are grouped together while the variations that deal with the contribution of the selected MC points towards the calculated motion are grouped together for comparison. Although the majority of the algorithm variations deal with the selection of the MC points, the last subsection deals with the estimation of motion based on the different mechanics models.

5.1.2.1 Selection of MC points

The modifications to the ‘Estimate Motion’ module that deal with the selection of MC points based on user-defined threshold conditions are:

1. **Threshold Number:** Change the number of MC points that contribute to the new position of the FEM point to check if reducing or increasing the number of points will affect the accuracy.
2. **Threshold Distance:** Change the maximum distance of a MC point from the FEM point in order to check if reducing or increasing the distance of the contributing points will affect the accuracy.

The details of these algorithms can be found in tables 3.3 and 3.4 of Chapter 3. Although it is a change in algorithm when deciding if the selection of the MC points should be influenced by meeting threshold conditions and which threshold conditions are met, the value of the thresholds are a user option to control the algorithm.

5.1.2.2 Weight of selected MC points

These variations to the algorithm work on the assumption that all the selected MC points may not influence the final position of a given node to the same extent. For this reason, weights are attached to each of the selected MC points as a means to control how much each influences the new position of the node. Such weights are commonly the inverse of the distance between two points and is based on the assumption that the position of a node should be most influenced

by the nearby points and less by the more distant points. A variation on this is to base the weights on Newton's law of universal gravitation where the weight of a selected MC point is the inverse or proportional to the inverse of the squared distance between the two points. This ensures that the contributions of further away points are further inhibited.

Thus the two variations to the module that use weights attached to the selected MC points to influence the resultant positions are as follows:

1. The contribution of an MC point is inversely proportional to its distance from the node whose new position is to be calculated.
2. The contribution of an MC point is inversely proportional to the square of the distance between the points if the contributions of the further points need to be inhibited.

5.1.2.3 Location of selected MC points

The final variation to the selection of the MC points is based on the assumption that the distribution of the points within the MC may not be uniform. Since there may be a concentration of MC points, and thus motion information, in a given direction or areas relative to a node, the final variation to the selection algorithm ensures that the MC points are selected according to their location in space to ensure that all legal directions are represented. As explained in Chapter 3 and seen in figure 3.8, the spatially aware selection of MC points chooses the closest MC points in every quadrant to contribute to the computation of the new position of the FEM node to make sure that points in every direction contribute to the calculation rather than simply the closest MC points. In other words the area around a node is split into eight quadrants and the closest MC point(s) in each quadrant is used to compute the new position to minimise the influence of a region that is motion information rich.

5.1.2.4 Mechanics model

As discussed in Chapter 3, the two mechanics models that are used in the two motion computation algorithms are Classic mechanics and Analytical mechanics.

The classic mechanics algorithm calculate the path of motion based on the Newtonian equations of motion while using analytical mechanics the motion path of a node is calculated based on Hamiltonian or Lagrangian equations in the form of spring connections.

5.1.3 Simulated models

In addition to testing that the SEP can be used for a reasonably accurate reconstruction of the basic mathematical model and its motion, simulations can also be used to test the sensitivity of the SEP to variations of the basic model. To this end, additional mathematical models and simulations are created to model specific test criteria. These include models that have irregular force patterns acting on them to replicate abnormal strain situations and thinner chamber walls to replicate the thin RV walls to test if the SEP's motion estimation module can be extended to handle the RV chamber. The final test simulation models various acquisition conditions including changing the number of induced tag planes and the number of acquired slices to test the sensitivity of the SEP to various acquisition properties and conditions.

The basic model, described in Chapter 4, is designed to test each module of the SEP. For instance, the conical geometry tests the 'Create FEM' module as well as the sensitivity of the different 'Estimate Motion' algorithms to the lack of motion information for the conical tip. When a given algorithm is deemed as having a reasonable accuracy with the basic or ideal model, forces of varying magnitudes and patterns are applied to create a test simulation of abnormal motion. The different magnitudes of forces are also used to help address the question of how many slice acquisitions need to be made in the duration of a heart beat to estimate motion with reasonable accuracy. Hence, varying the force patterns, the number of tag planes and the number of acquired slices are used to test the sensitivity of the 'Estimate Motion' module.

5.2 Validation tests using simulation

As mentioned before, a number of different simulations are used for the purpose of validating the SEP and its modules as well as identifying the algorithms that achieve the best accuracy. Of the validation test runs of the SEP, a total of 26 are discussed below to describe the findings. The values that are used to control the SEP and motion estimation algorithm include the type of estimation (Newtonian/Lagrangian), the type of numerical method used by the MC and the resolution of the model that is created. These values are parameters that are controlled by a text file in order to allow for easy modification of the SEP.

5.2.1 Mechanics model

The comparison of the Lagrangian motion estimation against the Newtonian algorithm proved simpler than anticipated by the almost immediate collapse of the models. Figure 5.2 shows a model using the Lagrangian motion estimation before its collapse. On the other hand, the Newtonian algorithm resulted in stable solutions as seen in figures 5.3. A stable solution may have been achieved given more time to modify the spring values appropriately.

Although tweaking the spring values may result in a stable Lagrangian motion estimation solution for a given model it was decided that this is not likely to be a reliable way to create stable solutions since these values may need to be modified for each model that needs to be created using the SEP.

5.2.2 Weight of selected MC points

The first simulations were designed to compare how using different types of weights in the ‘Estimate Motion’ module affect the accuracy of the SEP result. To this end a basic simulation model is created with even forces acting on the nodes of the FEM, 10 tag planes induced in each direction component and 10 VS acquired in the required orientations.

The effect of weighting the selected MC points on the accuracy of the SEP results is further tested by varying the threshold number of MC points that can be selected. As seen in figure 5.4, the comparison of validation tests shows that

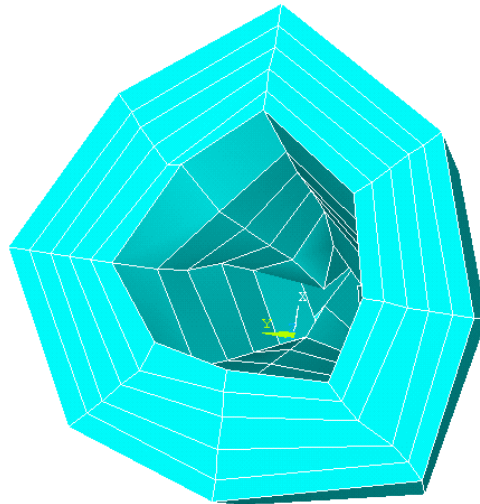


Figure 5.2: Validation of SEP using Lagrangian motion estimation

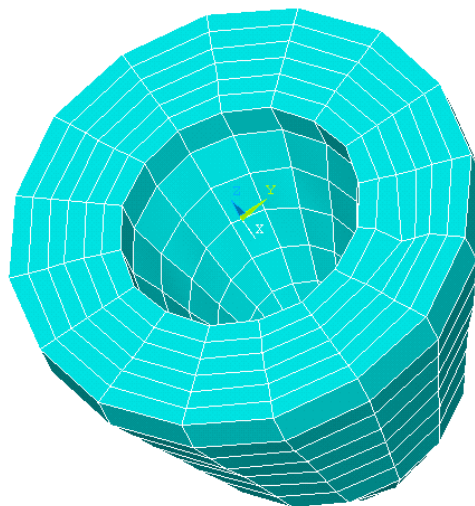


Figure 5.3: Validation of SEP using Newtonian motion estimation

5.2 Validation tests using simulation

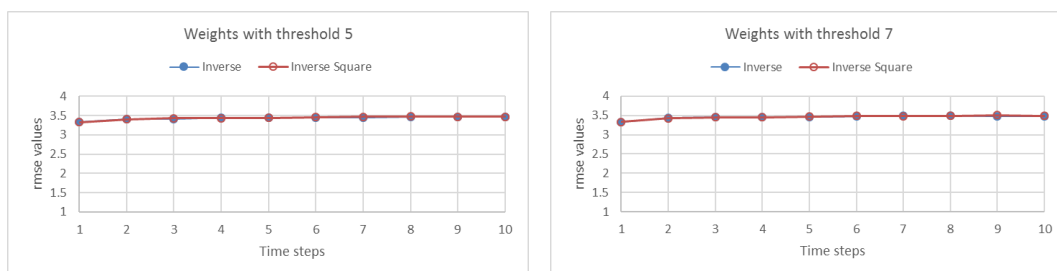


Figure 5.4: Varying weights of MC points

The graphs compares the rmse values at each time step; the graph on the left compares the performance of the inverse and inverse square weighted selection of MC points with the threshold number of MC points is 5; the graph on the right compares the performance of the inverse and inverse square weighted selection of MC points with the threshold number of MC points is 7

there is an insignificant difference in accuracy resulting from the use of the inverse and inverse square weighting. Figure 5.5 shows that this remains the case when the error of the results is split in to its constituent coordinate components.

5.2.3 Selection of MC points using threshold distances

The next set of tests are to establish the effect of changing the threshold distance on the result of the SEP. This is done on the basic simulation model described above with threshold number values of 5 and 7. The weights of the MC points are kept constant at the inverse square setting since it was established in the first phase that the weights do not have a significant effect on the accuracy of the SEP. As seen in figure 5.6, the test results are identical for the threshold number values of 5 and 7 and comparable for both threshold distances of 5 and 10. However, it is clear that keeping a lower threshold distance is advantageous to avoid the small fluctuation in the accuracy at time steps 4 and 5.

5.2.4 Applied force patterns

The next phase of simulations are designed to establish that the SEP works with reasonable accuracy for different force patterns. To this end, the basic simulation

5.2 Validation tests using simulation

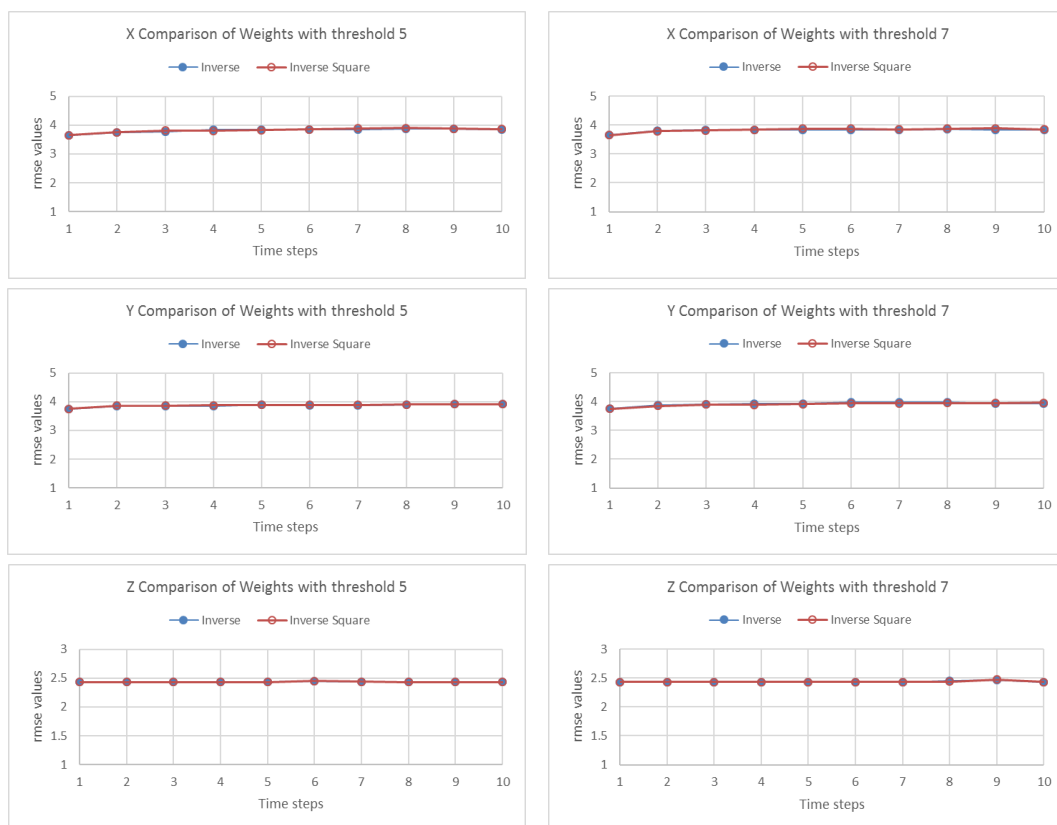


Figure 5.5: Varying weights of MC points - coordinate components

The graphs compare the rmse values of the different coordinate components at each time step; the graphs on the left compares the performance of the inverse and inverse square weighted selection of MC points with the threshold number of MC points is 5; the graphs on the right compares the performance of the inverse and inverse square weighted selection of MC points with the threshold number of MC points is 7

5.2 Validation tests using simulation

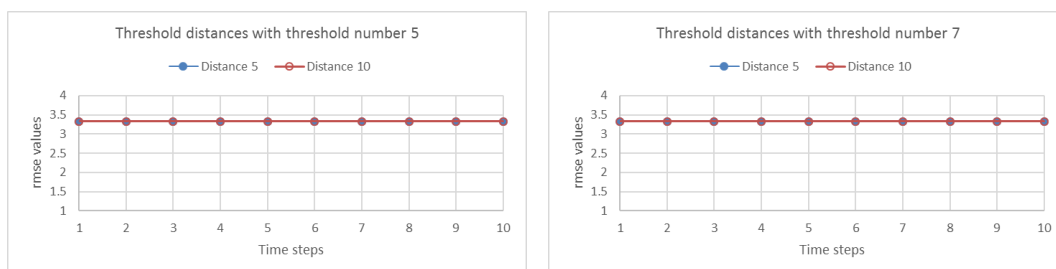


Figure 5.6: Varying threshold distances of MC points

The graphs compare the rmse values of the test runs using different threshold distances at each time step; the graphs on the left compares the selection of MC points using threshold distance of 5 and 10 with the threshold number of MC points is 5; the graphs on the right compares the selection of MC points using threshold distance of 5 and 10 with the threshold number of MC points is 7

model was modified to have non-uniform forces acting on it. The basic motion estimation algorithm for these tests are set to have constant threshold distance and weighting of selected MC points since it was shown that variations provide comparable results. The user settings of the algorithm that are used to make the comparison of force pattern identification are varying the threshold numbers of 5 and 7 as well as the spatially aware and basic options. Thus, applying uniform and non-uniform force patterns on the basic simulation model and using the different user options of the ‘Estimate Motion’ module generate four different validation scenarios.

As seen in the graphs in figure 5.7, the SEP performs with comparable accuracy despite the forces applied on the simulated model.

5.2.5 Selection of MC points using threshold numbers

The first set of simulations can also be used to find the effect of threshold numbers on the accuracy of the SEP results. As seen in figure 5.8, by keeping a constant weighting of either inverse or inverse square it is possible to find the effect of the threshold number on the accuracy of the SEP by comparing the results of the SEP versions with threshold number of 5 or 7. Applying non-uniform forces to the simulation model allows for the verification that the results are independent of the

5.2 Validation tests using simulation

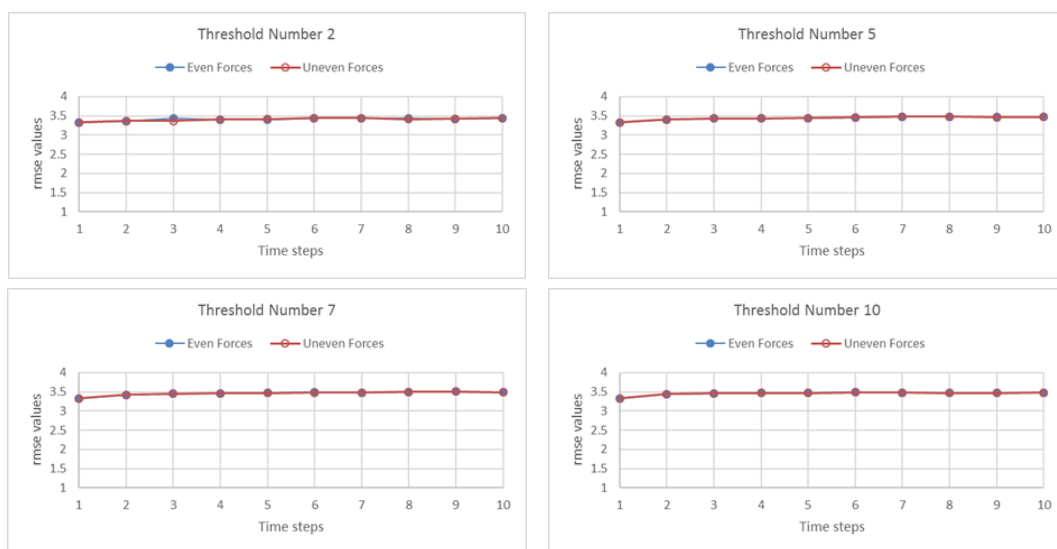


Figure 5.7: Varying force patterns

The graphs compare the rmse values of the test runs using different force patterns (uneven and even) at each time step

applied forces as seen in the graph on the right side of figure 5.8. This comparison of validation tests shows that lower threshold numbers result in marginally better accuracy.



Figure 5.8: Varying threshold numbers

The graphs compare the rmse values of the test runs using different threshold numbers at each time step; the graph on the left compares the selection of threshold number (5 and 7) of MC points while varying the weights with a uniform force pattern; the graph on the right compares the selection of threshold number (5 and 7) of MC points with a non-uniform force pattern

5.2 Validation tests using simulation

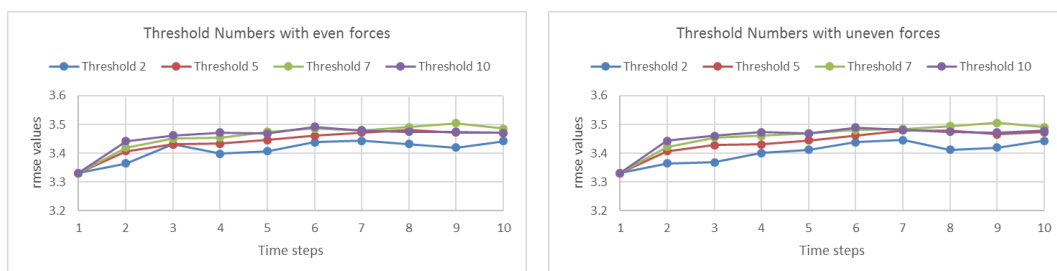


Figure 5.9: Varying threshold numbers with non-uniform force pattern applied. The graphs compare the rmse values of the test runs using different threshold numbers at each time step; the graph on the left compares the selection of varying threshold numbers of MC points with a uniform force pattern; the graph on the right compares the selection of varying threshold numbers of MC points with a non-uniform force pattern

Since it is unexpected that the influence of fewer MC points results in higher accuracy, further tests are conducted by varying the threshold numbers as seen in figure 5.9. Comparing the accuracy of the SEP results with the threshold number values of 2, 5, 7 and 10 confirms that the lower threshold numbers result in better accuracy regardless of the force patterns that are applied.

5.2.6 Location of selected MC points

The next simulations test the accuracy that is achievable by selecting MC points using a spatially aware algorithm compared against the basic selection algorithm that is spatially ignorant. The validation tests are conducted separately for threshold numbers 5 and 7. As seen in figure 5.10, for both values of threshold numbers the spatially aware selection of MC points results in an improvement of the achieved accuracy. Figure 5.11, shows the comparison of the accuracy achieved using spatially aware selection with various threshold values. Unlike the accuracy with the regular selection algorithm, increasing the threshold numbers does not change the accuracy drastically. However, in the case of the spatially aware selection algorithm, increasing the threshold number value reduces the accuracy in the beginning but improves the accuracy of the last phases.

5.2 Validation tests using simulation

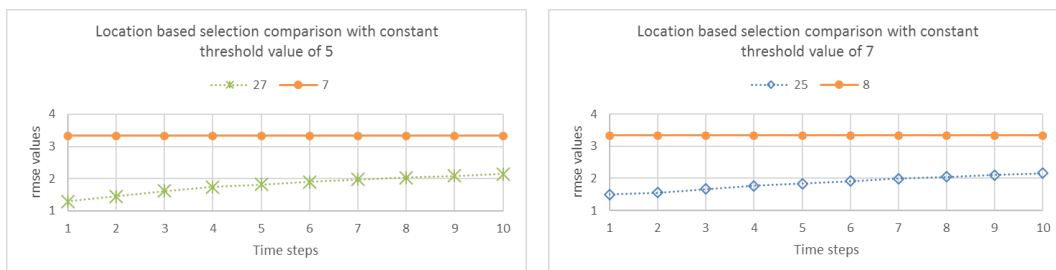


Figure 5.10: Varying threshold space

The graphs compare the rmse values of the test runs at each time step; the graph on the left compares the spatially aware (Test run 27) and unaware (Test run 7) selection of threshold number (5) of MC points; the graphs on the right compares the spatially aware (Test run 25) and unaware (Test run 8) selection of threshold number (7) of MC points

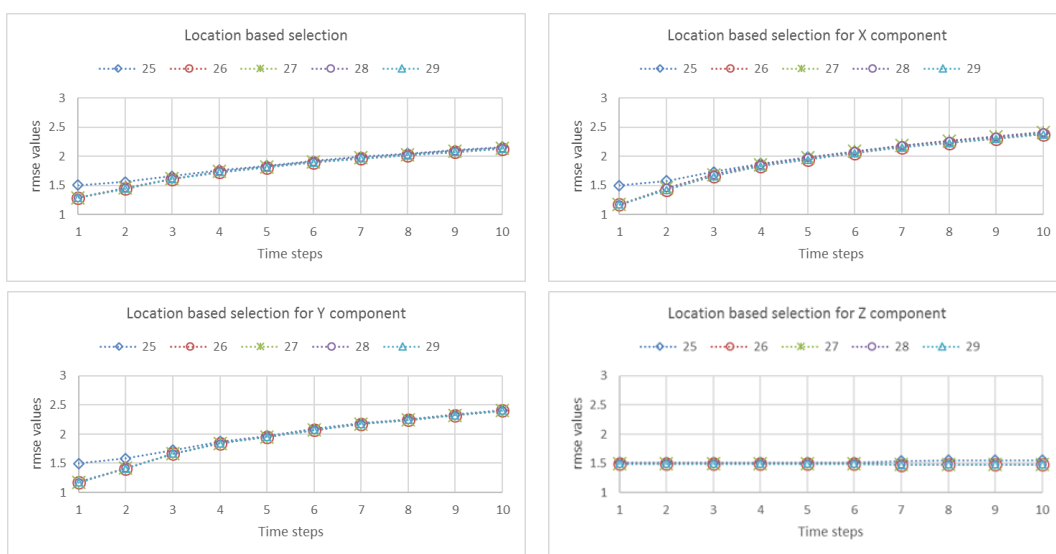


Figure 5.11: Location based algorithm

The graphs compare the rmse values of the test runs at each time step; Test run 25 uses a threshold number of 7; Test run 26 uses a threshold number of 5; Test run 27 uses a threshold number of 5; Test run 28 uses a threshold number of 2; Test run 29 uses a threshold number of 2

5.2.7 Induced numbers of VTP

The next validation tests are designed to find a relationship between the number of VTP and the accuracy of results. As seen in figure 5.12, the results are comparable with the increased number of VTP when the threshold value of 7 is used in the SEP and marginally improves the accuracy when the threshold value of 5 is used in the SEP.

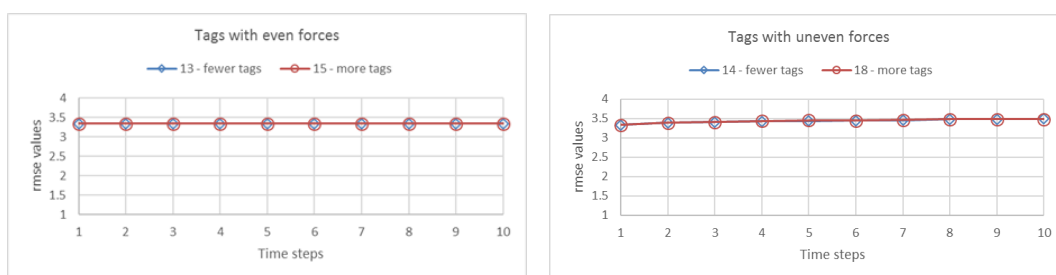


Figure 5.12: Varying numbers of VTP

The graphs compare the rmse values of the test runs at each time step; Test runs 13 and 14 use 10 VTP while test runs 15 and 18 use 20 VTP

Figure 5.13 shows that the results are comparable even when comparing the different coordinate components separately.

5.2.8 Acquired number of VS

The next set of validation tests double the number of acquired VS to compare the resulting achievable accuracy. As evident from figure 5.14, when the spatially ignorant selection of MC points is made in the ‘Estimate Motion’ module, increasing the number of VS reduces the accuracy as expected. However, the increase in the number of VS improves the accuracy in a spatially aware selection of MC points despite the increased threshold number value of 7.

Figure 5.15, shows that the results are comparable even when comparing the error of the different coordinate components.

5.2 Validation tests using simulation

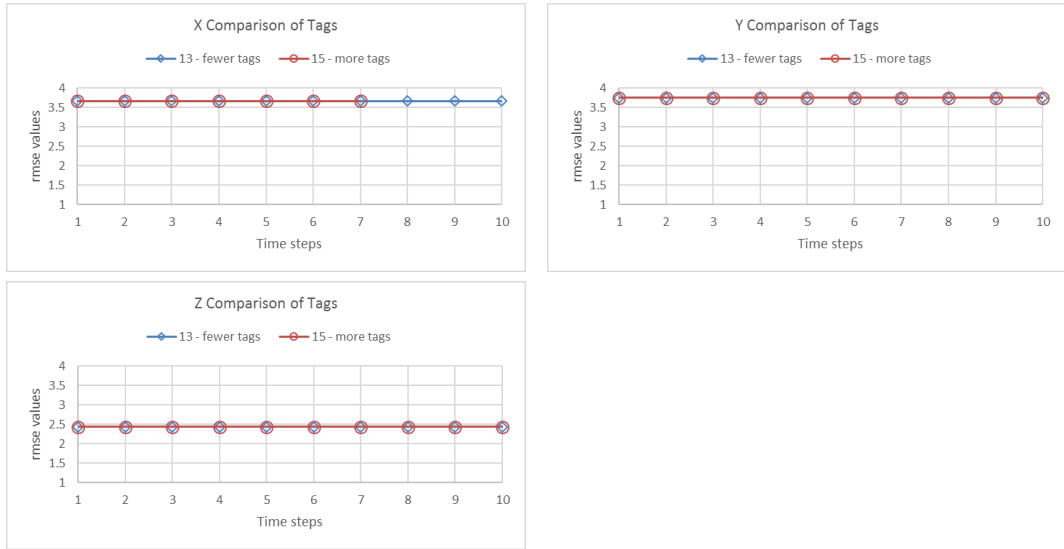


Figure 5.13: Error components for varying number of VTP

The graphs compare the rmse values of the different coordinate components at each time step; Test run 13 uses 10 VTP while test run 15 uses 20 VTP

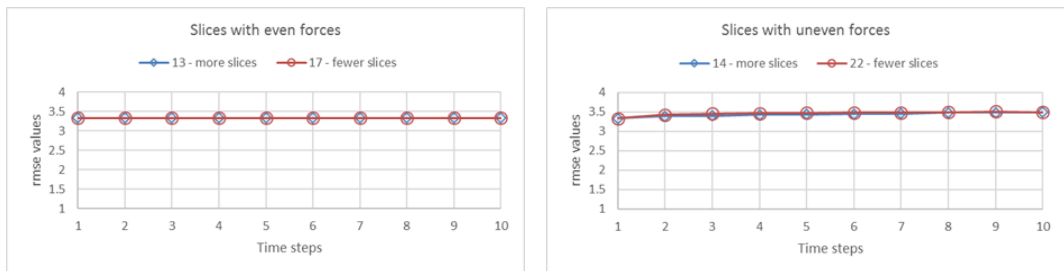


Figure 5.14: Varying number of VS with even & uneven forces

The graphs compare the rmse values of the test runs at each time step; Test runs 13 and 14 use 20 acquired VS while test runs 17 and 22 use 10 acquired VS

5.2 Validation tests using simulation

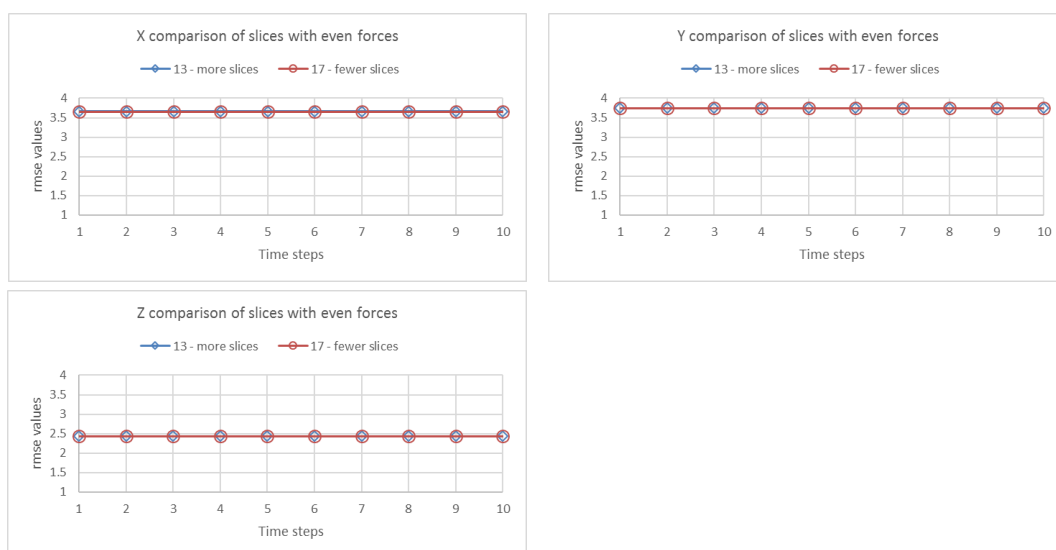


Figure 5.15: Error components for varying number of VS

The graphs compare the rmse values of the different coordinate components at each time step; Test run 13 uses 20 acquired VS while test run 17 uses 10 acquired VS

5.2.9 Number of elements in FEM

The final validation test set reduces the number of elements used in the SEP to compare the achievable accuracy.

The first comparison is made using the basic simulation model with the different number of elements in the constructed FEM as input to SEP versions with the normal selection of MC points and constant values of inverse square weighting and a threshold number of 7. As seen in figure 5.16, using fewer number of elements in the FEM noticeably improves the achievable accuracy of the results.

The next comparison is made using the same basic simulation model with the different number of elements in the constructed FEM as input to SEP versions with a spatially aware selection of MC points, constant values of inverse square weighting and threshold numbers of 5 and 2. As seen in figure 5.17, there is no resulting improvement in accuracy from using fewer elements in the FEM.

Figure 5.18 shows that the accuracy of the SEP in both the x and y directions are better with fewer elements. The results of the SEP in the z direction, however, are marginally better when more elements are created. Thus, it may be possible

5.2 Validation tests using simulation

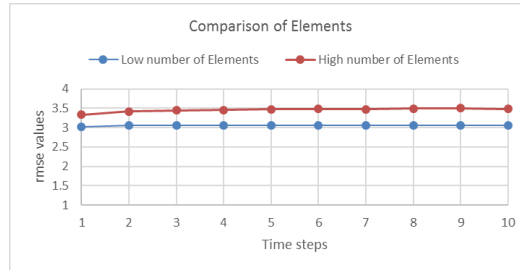


Figure 5.16: Varying number of FEM elements

The graphs compare the rmse values at each time step; the comparison is made between a FEM containing 394 elements and another FEM containing 788 elements

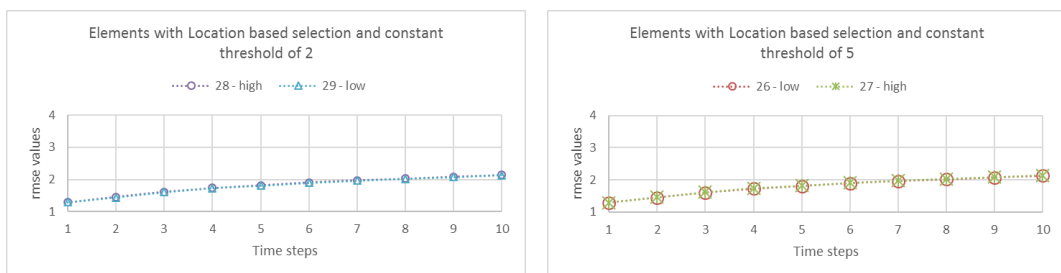


Figure 5.17: Varying number of FEM elements using location based selection algorithm

The graphs compare the rmse values of the test runs at each time step; Test runs 27 and 28 have a FEM containing 788 elements; Test runs 26 and 29 have a FEM containing 394 elements

5.2 Validation tests using simulation

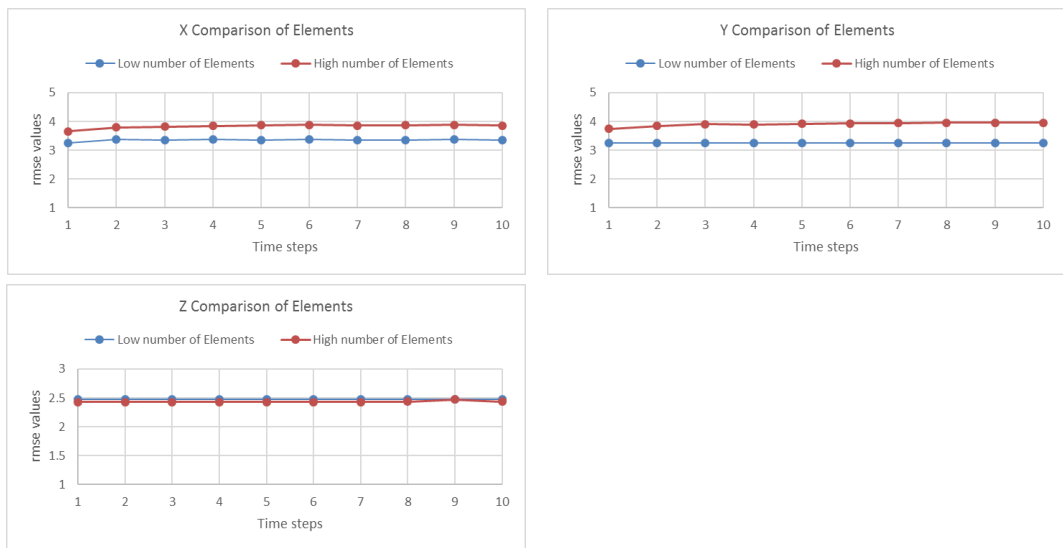


Figure 5.18: Error components for varying number of FEM elements - coordinate components

The graphs compare the rmse values of the different coordinate components at each time step; the comparison is made between a FEM containing 394 elements and another FEM containing 788 elements

to improve the overall SEP accuracy by increasing the number of elements in the z direction alone. A possible reason for this behaviour could be the magnitude of the motion in the z axis is more than that in the xy plane. The results of the validation tests may be in part because the value of the ‘fewer’ elements was not appropriate for the resolution of the image. It is thus appropriate to conclude that further test runs would need to be designed and conducted to have a definitive conclusion on the effect of element numbers on the SEP accuracy. However for the values tested, it appears that fewer elements result in better accuracy on the xy plane and reduced accuracy in the z axis.

5.3 Achieved accuracy of SEP

The validation tests discussed in the previous section show that the SEP can be used to estimate motion and that as expected, the accuracy of the results is dependent on the algorithms used. In this section, to further study the results of the validation tests the rmse of each validation test is calculated to give us an idea of how each fared against the others. In addition, the rmse values of the different coordinate components have been compared to give further insight. The final analysis of the accuracy of the results is made by splitting the FEM into sections along the LA to study if the accuracy is consistent across the sections as well as if particular algorithms fare better in certain sections of the model.

As seen in figure 5.19, the accuracy of the SEP results with the spatially aware selection (validation test runs 25-29) of MC points is consistently better than with the normal selection (validation test runs 1-24). The figure also shows that this is true when the accuracy of the individual coordinate components is calculated.

Since the spatially aware selection of the MC points achieved the best overall results, the results are further analysed by separating the points according to the section of the model along the LA. A study of the graphs in figure 5.20 shows that the accuracy of each section of the model is comparable for all the validation tests. Figure 5.21 shows that the accuracy achieved in the middle section of the model is very marginally lower than the other sections.

5.3 Achieved accuracy of SEP

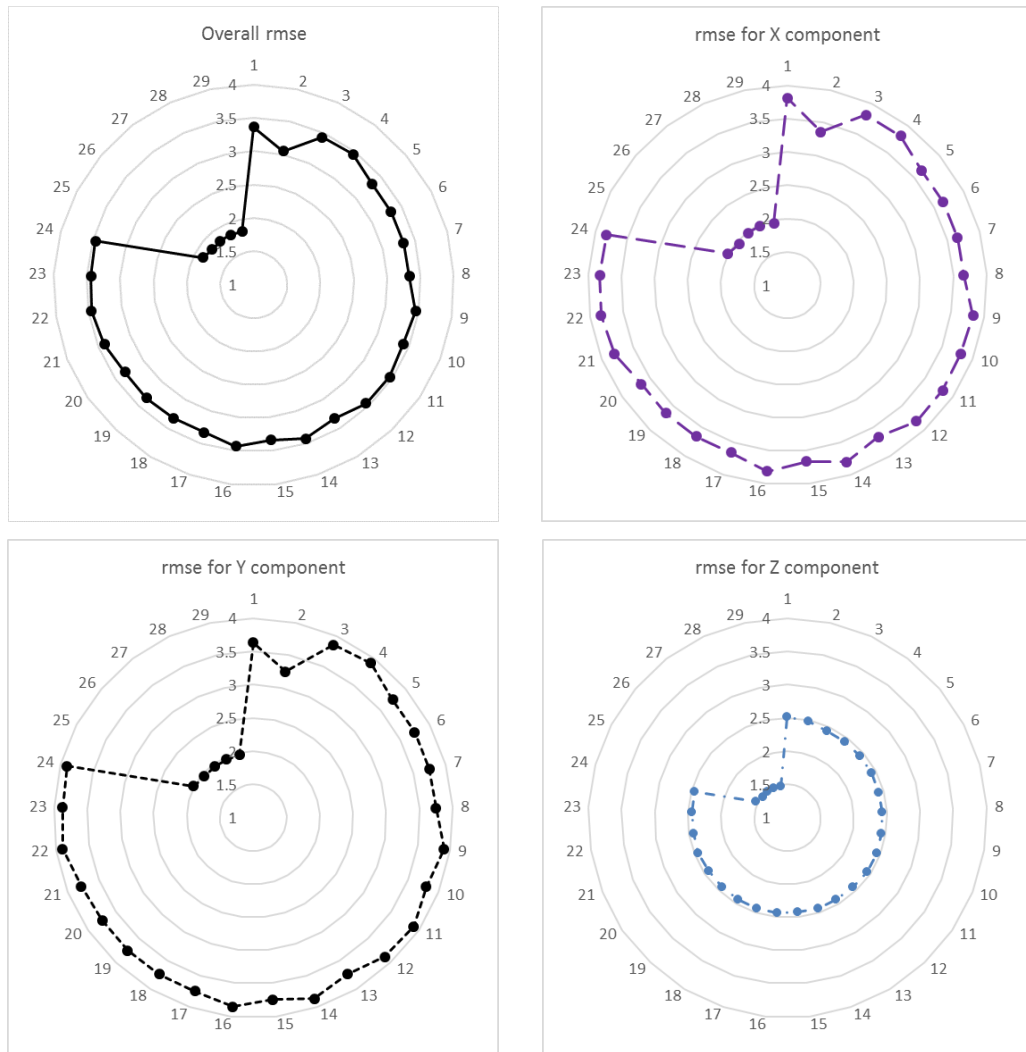


Figure 5.19: RMSE results for each validation test run

The graphs compare the rmse values (overall and for each coordinate component) of each validation test (1-29) conducted

5.3 Achieved accuracy of SEP

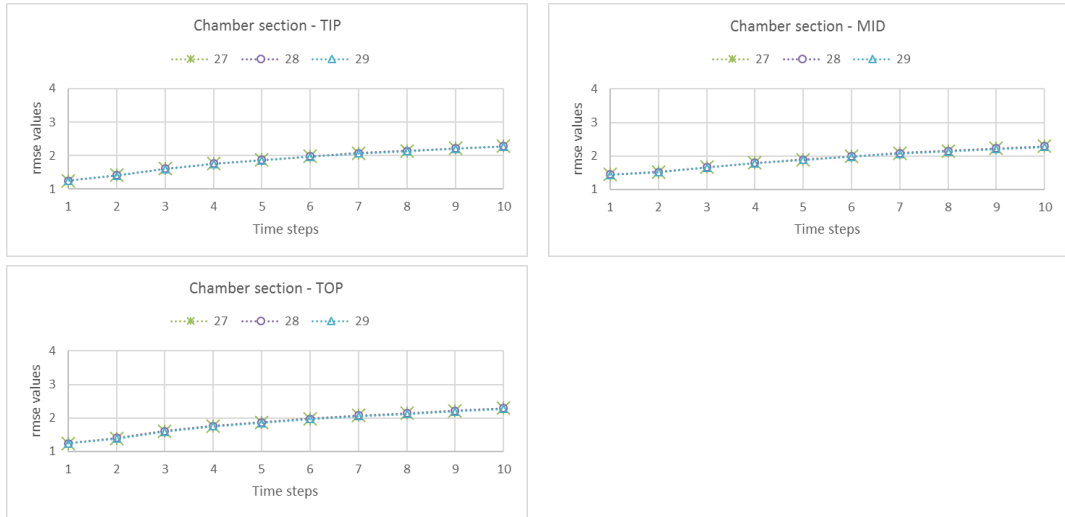


Figure 5.20: RMSE results for the different sections of the model
The graphs compare the rmse values for each of the three sections of the geometry for test runs 27 (threshold number of 5 with 788 elements), 28 (threshold number of 2 with 788 elements) and 29 (threshold number of 2 with 394 elements)

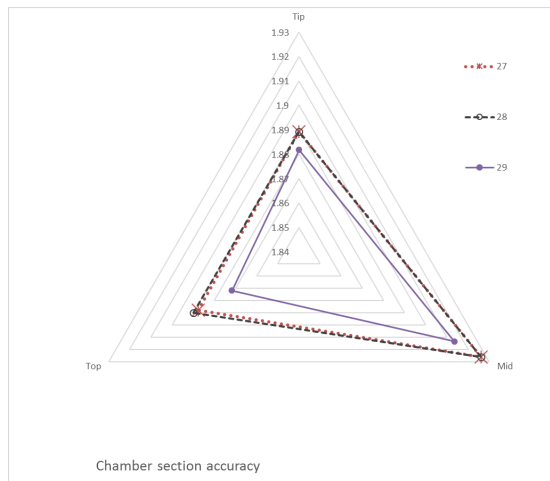


Figure 5.21: Chamber section specific rmse results for varying number of FEM elements

The graph compares the rmse values for test runs 27 (threshold number of 5 with 788 elements), 28 (threshold number of 2 with 788 elements) and 29 (threshold number of 2 with 394 elements)

5.4 Analysis of tMRI dataset

Since the use of the spatially aware selection of MC points produced the best accuracy during the validation of the SEP, it is this algorithm that is used to process the tMRI. The tMRI dataset of 175 slices is organised into 25 slices, one for each time step, in each of three SA locations and four LA locations. The following sections detail the use of the different SEP modules to process the acquired tMRI data.

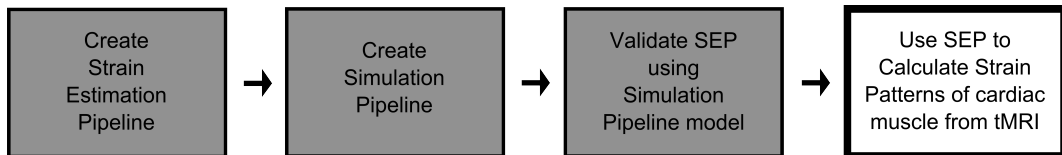


Figure 5.22: Research stage: cardiac strain patterns using SEP

5.4.1 Using the ‘Extract Features’ module to identify chamber walls and tag lines in tMRI data

Although the tag lines need to be identified in each of the 175 tMRI slices, the chamber walls are only needed at the beginning of the sequence or in each of the SA and LA slice locations at the initial time step, which is used for the creation of the FEM.

5.4.1.1 Identifying chamber walls

One of the problems with the tMRI dataset is that the chamber walls are hard to discern for the initial time steps, as evident in figure 5.23. This led to identifying the chamber walls at a later time step and modifying the identified lines to fit the contours that are visible at the resting phase, as seen in figure 5.24. In other words, the wall contours are segmented in about 5 or 6 slices for each of the seven sequences of slices. Thus, in total between 35 and 42 slices are segmented to get the chamber wall edges.

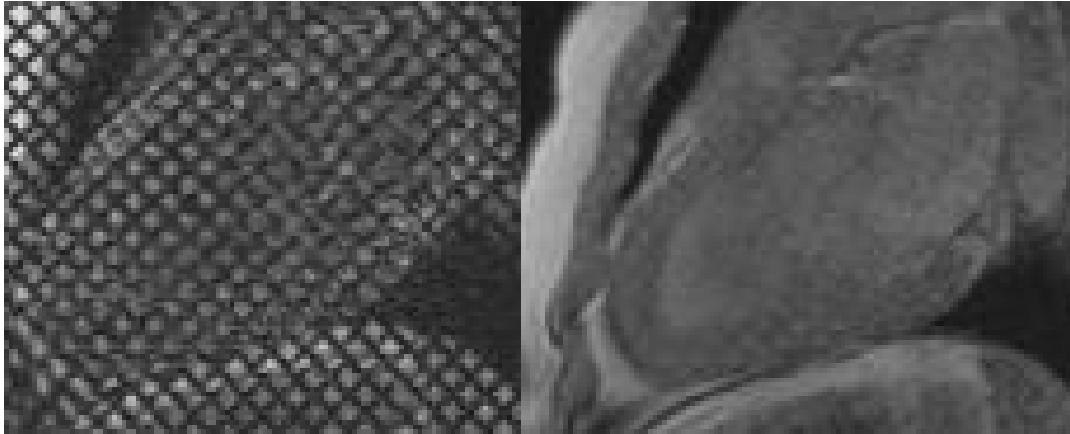


Figure 5.23: tMRI LA slices at time step 0 and 24

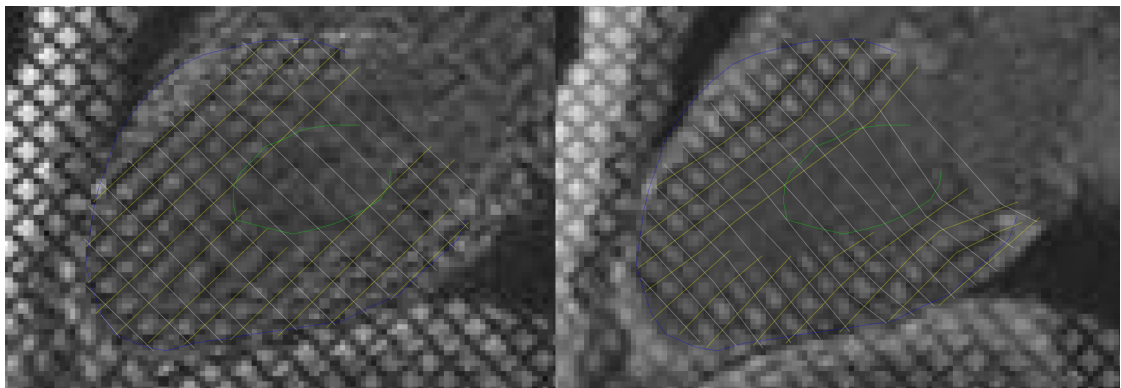


Figure 5.24: Chamber wall identification

Chamber contours are identified from t_0 slice using chamber contours identified from t_5 slice

5.4.1.2 Identifying tagged tissue

The tMRI dataset is acquired with the induced tags in the grid pattern, meaning that there are two directions in which the sets of tag lines need to be segmented for each slice of the dataset. This in turn means that there are between 20-25 usable tags, within chamber walls, to be segmented per slice making the task time consuming and laborious.

The segmentation of tag lines is made less complex by modifying the tag lines from the previous time step instead of having a fresh start at every step. This reduction in time taken to segment the tag lines proved especially useful towards the end of the time sequence when segmenting slices can be extremely difficult due to the fading of the tag lines, as seen in figure 5.25.

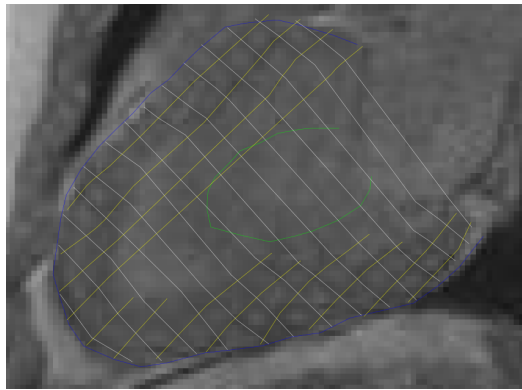


Figure 5.25: Identified tag lines at time step t22

5.4.2 Using the ‘Create FEM’ module to create an ANSYS FEM from the processed tMRI data

The generated VS is accurately loaded into ANSYS and the FEM was generated. However, the generated FEM was created with shape errors and some of the elements are not formed. The most likely cause of these errors is the resolution of the images and resolving the shape errors will require manual intervention to resolve the shape errors. The alternative solution may be to scale the VS as done during the segmentation. In other words, the dimensions of the VS can be

scaled up for the creation of the FEM and correspondingly scaled down for the final calculated strain results. The other option is to generate a FEM with large elements and use ANSYS to increase the number of elements making it possible to interactively change the resolution of the FEM. The final generated model without the offending elements can be seen in 5.26.

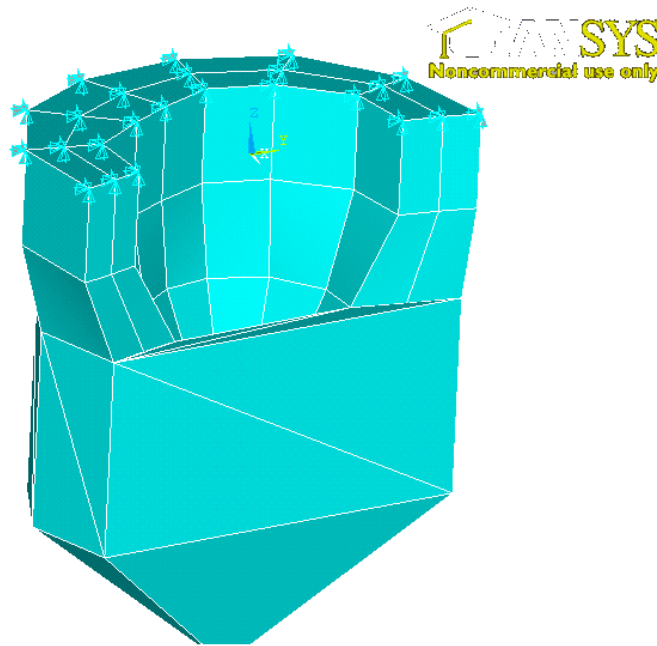


Figure 5.26: tMRI result of SEP before FEM analysis

5.4.3 Using the ‘Estimate Motion’ module to estimate the deformation of the ANSYS FEM created from the processed tMRI data

The deformation of the part of the FEM that was created without errors was estimated successfully but involved user interaction in the ANSYS environment. The ‘Estimate Motion’ module coped well despite the errors since it works with the individual FEM nodes rather than the elements. This meant that the motion of all the generated nodes were estimated. However, warnings were generated

by ANSYS when reading the modification of certain nodes' positions. It may be possible and useful to modify the SEP to generate ANSYS error log files and remove all relevant nodes to avoid futile processing.

5.4.4 Using the 'Calculate Strain' module to produce the regional strain pattern of the ANSYS FEM deformed using the processed tMRI data

The regional strain values of the ANSYS FEM were calculated without any errors since ANSYS removes all the offending elements before processing. However, this does mean that the values are not likely to be relevant to the tMRI data.

5.4.5 Results of processing tMRI data using SEP

A comparison of the results of processing the tMRI data using the SEP and another process would be ideal to verify the results and to quantify the achieved accuracy. However, this was not possible since the datasets available were not used to detect regional motion in the same way. The Cardiac Atlas project data was made available for public use as part of a segmentation challenge for a conference, while the UCLA data was anonymised patient data that was provided as a favour and as a consequence had not been used before.

5.5 Chapter summary

This chapter details the methodology of validation as well as the various simulation models that are used to validate and test the achievable accuracy of the SEP.

The first section discusses the methodology of validating the SEP, identifying the measure of comparison that is used, the algorithm variations that are tested as well as the various simulation model options. The next section details the various tests that are conducted along with the analysis of the achieved accuracy of the different SEP algorithms and user defined conditions. Based on the validation test results, it should be possible to increase the accuracy of the SEP that uses

5.5 Chapter summary

the regular selection of MC points, by reducing the threshold number value along with the number of elements. However, of all the motion estimation algorithms tested, the spatially aware selection of MC points proves to achieve best accuracy.

The final section details processing the tMRI data using the validated SEP.

6

Conclusions

Heart disease is a problem across the world's population that isn't restricted to any cross section of the population and so any tool or technology that can detect heart disease early reducing the number of heart disease related fatalities is needed and useful. As explained in Chapter 1, MRI is the best imaging modality for non-invasive investigation due to the limited exposure to radiation. Of the various MRI techniques that are applicable for cardiology, tMRI is especially useful to investigate regional strain patterns of the heart due to its capacity to visualise the abnormal motion of the chamber muscle which is an early indicator of heart diseases like CAD and myocardial ischaemia. Thus, researching the use of tMRI in cardiology for the diagnosis of CAD and myocardial ischaemia is an active area due to its applicability in the identification of regional strain patterns and the scope in the field. This results in an increasing number of techniques available by which to tag tissues making tMRI a constantly developing technology. The number of tMRI techniques have resulted in a variety of ways in which the datasets can be processed. However, to build a clinically useful tool there needs to be a standard method of processing tMRI datasets that can adapt to changes in the tMRI technology. The SEP suggested in this research is such a standard methodology or framework that can be used to process tMRI datasets.

By using the SEP concept it is possible to cater for developments and has requirements of the research by simply modifying the section of the pipeline it deals with. For instance, when using advanced tMRI techniques it may be possible to use an entirely automatic feature extraction approach in place of the

manual segmentation approach taken here to extract the features of the dataset. In a similar manner any algorithm may be replaced in the SEP as long as the intermediate data remains the same and the simulation pipeline is used to validate the modified SEP. An additional advantage of having an organised and testable methodology to process tMRI data is that it makes it possible to compare the accuracy of different algorithms. Although the processes that tMRI slices undergo to convert them into useful regional motion information along with the strain pattern of the LV may be known, organising it as a pipeline is novel.

In the literature the use of finite element analysis is normally by means of a purpose built tool. The use of the commercial FEM package, ANSYS, in the SEP has allowed for the faster development of the prototype. ANSYS has proved to be a very comprehensive tool with a multitude of shape and material property settings that are applicable but have yet to be explored fully.

The accuracy achieved by the SEP using the MC is acceptable for the purpose of a diagnostic tool. Although there may be a need to improve the accuracy if it were to be extended for treatment planning. A diagnostic tool needs to be fast providing fairly accurate results rather than slow with highly accurate results to move closer towards real-time or near real-time diagnosis. The need for fast diagnosis is to avoid multiple patient sittings to investigate and plan treatment when required. In other words, a fast diagnostic tool with reasonable results allows for further investigation and treatment planning to be conducted in the same visit for MRI scans.

The final contribution of the research comes in the form of the simulation pipeline and its use in validating the SEP and its modules. Previous research use a variety of methods to validate their methods, ranging from the use of synthetic or simulated data to manual verification. The method for validation however, is dependant on the process in question, with segmentation algorithms normally validated by manual verification and motion tracking algorithms validated by synthetic or physically simulated data. The other problem with these validation methods is that only two dimensions are accounted for as explained in Chapter 3. The use of the simulation pipeline allows for the validation of the SEP and all of its constituent modules by a single validation methodology that deals with all three dimensions of motion rather than the two dimensions of the slice plane.

As stated in Chapter 1, the aim of the research was to develop a diagnostic tool using tMRI, to identify abnormalities in wall motion of the LV in order to identify and investigate CAD and myocardial ischaemia. The objectives that were identified to achieve this aim include the following:

- Obj 1 Identify the main modules that will process the tMRI data to calculate a regional strain model
- Obj 2 Identify and implement a validation process for the modules identified
- Obj 3 Implement and validate the modules used to calculate a regional strain model from tMRI data using the implemented validation process
- Obj 4 Analyse tMRI data resulting in a motion model of the myocardium and the regional strain and stress maps for the deforming myocardium
- Obj 5 Find a relationship between the distance between consecutive slices, the number of phases acquired, the tag plane distance and the accuracy of the reconstructed motion

The first section of this chapter is a review of the progress made on each of these objectives along with the problems faced. This is followed by a brief discussion of the direction that the research can take in the future. Details of the steps taken towards achieving the listed objectives can be found in the thesis chapters (Objective 1 in Chapters 2 and 3, Objective 2 in Chapter 4 and the remaining in Chapter 5).

6.1 Achieved objectives

The progress made on Objective 1 is discussed in section 6.1.1 along with a discussion on the use of ANSYS in the research. Section 6.1.2 details the progress on Objective 2, while section 6.1.3 details Objective 3. This is followed by Objective 4 and 5 in sections 6.1.4 and 6.1.5, respectively.

Ideally, the final step to test the hypothesis of the thesis would be to test the adaptability of the SEP to process tMRI slices that have been acquired using a different technique which was not possible due to the delay in acquiring the tMRI

datasets. However, the capacity of the SEP to adapt to changes can be argued as being inherent by means of its design. Additionally, as different algorithms were tested in the evaluation of different modules and validation of the SEP this can be used as further proof of the capability of the SEP to be modified to process a tMRI dataset that was acquired with a different tissue tagging technique.

6.1.1 SEP

The details of the identification of the modules used to process the tMRI data are discussed in Chapter 2 while the implementation details of the SEP are found in Chapter 3. As is evident from the validation tests, the SEP can be used to estimate motion with a degree of accuracy.

The tool chain used to implement the SEP was successful as a prototype, proving especially useful due to the ease with which modifications can be made when testing the different algorithms and models in the validation phase. Using multiple products to form the SEP although ideal for this scale of project cannot be optimised for speed. Adopting the pipeline architecture made it easy to add and change methods or entire modules as long as the intermediate data format stays the same. On completion of the work it can be asserted that organising the processing of tMRI dataset to produce the required strain model as a pipeline is useful.

Although a number of segmentation options were explored during the course of this project, due to the time constraints imposed by the difficulty in obtaining the required tMRI data, a fully manual segmentation approach was employed for the feature extraction purposes of the prototype. This and the occasional need for human intervention when using ANSYS has meant that the developed SEP is not an automated process. The FEM creation module was effective in most cases, however shape violation warnings were occasionally raised by ANSYS when some of the mathematical models were loaded during development of the SEP. Although, it was technically possible to check for shape violations within the ‘Create FEM’ module this was decided against as it would have resulted in built-in restrictions on the solid types that are supported. The other option to deal with these errors would have been to generate a very basic skeleton of the FEM

and interactively increase the resolution within the ANSYS package. This was finally decided against to reduce the amount of user interaction required within the ANSYS environment. This is an approach that would be worth revisiting in the future to avoid the warnings raised by shape violations.

ANSYS is a powerful FEM package with more capabilities than are required for the generation of the regional strain patterns. One of the advantages of using the package is the ease with which its use can be integrated with other software by means of text based instruction and text files. In addition to its graphical interface with fairly mature data visualisation options, ANSYS also has the advantage of a fairly active expert user base. However, since ANSYS is specifically designed for engineers the resources for modelling tissue are less prolific.

6.1.2 Simulation pipeline as a method of evaluating the SEP

The details of creating the simulation pipeline, the mathematical model and its motion are given in Chapter 4, along with the details of the implementation of the SEP and its constituent modules using the basic mathematical model simulation. The SEP implementation involved the individual modules being developed with the help of the intermediate simulation pipeline outputs as depicted in figure 4.14. This approach to evaluate and influence the development of the SEP proved to be especially convenient and useful, since the tMRI data was available only in the last 4 months of the project.

The human heart is a continuous roll of muscle twisted to form four chambers thus creating a structure considerably more complex than the simple conical volume used to model the LV in the simulation phase. The prolapsed hemispherical geometry that is used in most research is a closer model of the geometry of the LV but does not simulate the conditions of reduced motion information, which as stated in Chapter 4, is the reason for adopting the simple conical shape. In the case of tMRI slices, this sparsity of motion information is a result of the global motion of the LV as well as the magnitude of the through-plane motion in this region. Near the tip of the geometry the magnitude of through-plane motion is modelled by the forces that are applied while limiting the number of nodes

and elements replicates the lack of motion information on a given VS plane as expected from medical data. Thus, instead of modelling the global motion of the LV, the simulation complexity is minimised by replicating the reduced motion information of the tip by means of fewer nodes, elements and consequently the intersecting tag planes that indicate motion in the VS. This does mean that the resulting ‘Create FEM’ module results in a more angular FEM than required when processing tMRI slices. However, this problem is easily rectified by increasing the number of nodes and elements in the tip when processing the tMRI slices. The other option would be to modify the module to generate a prolapsed hemispherical geometry from the slice information. This may involve splitting the creation of the structure into two halves, where one section is modelled to be more cylindrical and the bottom section is modelled to be hemispherical or ellipsoid which may require a different ANSYS element.

6.1.3 Validation of the SEP using simulation

A number of mathematical models have been created and can be modified with ease to facilitate the needs of the validation of the SEP. As detailed in Chapter 5, the simulation pipeline was effective in generating the multiple models that were required to validate the different algorithms used in the SEP modules.

The rmse values of the SEP accuracy for the different algorithms ranged between 3.5 and 1.8, which is deemed to be reasonable. Since the resolution of the tMRI data is quite low the FEM is created accordingly and since ANSYS calculations are unit free that makes the rmse value in pixels and thus acceptable. Although rmse is a suitable and established measure of comparison it is not ideal since the value is dependant on the order of the compared lists. In this project the two lists of nodes were sorted in increasing order of each motion component (first z, then y and then x components) of the first time step and then compared in that same order for all the remaining time steps. This was the simple solution to the limitation of rmse as a measure but to minimise post-processing it would be worth exploring other similarity measures in the future. The use of mutual information, a concept from probability theory and information theory that measures the mutual dependence of the two random variables, would be an

appropriate measure to explore. It measures the information that two variables share, calculating how much knowing one of the variables reduces uncertainty about the other, which is why it is used in registration to measure how alike two images are. Mutual information could thus be used as a measure of the similarity in the position and strain values of the model result of the SEP and the simulated model.

The validation of a tracking algorithm using synthetic data in the literature takes account of the motion on the plane and not the through-plane motion. Validation of the SEP using the simulation pipeline outputs mean that all the coordinate components of motion are taken into account since it is the two FEM node positions and strain values that are compared when the accuracy is calculated.

6.1.4 Analyse tMRI data generating a regional strain pattern for the deforming myocardium

The FEM generated from the tMRI data was loaded into ANSYS with a few shape violation warnings raised as in the case of some of the mathematical models. However, unlike in the case of the validation tests the time constraint meant that these were left unresolved and the model was processed along with the warnings. Since the shape violation warnings do not affect the motion estimation module, the FEM was successfully updated with the motion of the nodes. This is because estimating the motion using the MC works with individual nodes rather than elements. As expected, the calculation of regional strain using ANSYS raised warnings in the same elements but proceeded to calculate the strain values for the remainder of the model.

6.1.5 The relationship between the tMRI acquisition parameters and the accuracy of the reconstructed motion

Despite the large number of validation tests conducted with the various tMRI acquisition parameters, it was not possible to discern a clear pattern in the achieved

results and find a relationship between the parameters and the accuracy of results as initially hoped for. This is an area that can be further studied by running more carefully planned tests. For instance, in the case of the relationship between accuracy and the number of induced tag planes the minimum number of tag planes required to estimate the motion needs to be found. When the tests were planned for this project the expectation was that more tag planes would result in greater accuracy. Since tMRI slices normally have about 14 tag lines that intersect the LV tissue, the two validation models that were designed and tested had either 10 or 20 tag planes integrated into the model. As discussed in Chapter 5, the results of the different validation models were similar, which would imply that the minimum number of tag lines required to reconstruct the motion is less than 10. The reason that this may be of interest is that fewer tags in a slice would make it easier to segment the chamber walls.

6.1.6 Problems faced

The biggest obstacle in the research project was the difficulty in obtaining the required tMRI data. The problems cited when attempting to source the data ranged from the need for privacy, anonymity and required permissions from the patient, to convincing cardiologists and radiologists. Once these hurdles were appropriately negotiated the next problem faced was in receiving an incomplete dataset.

After exhausting local avenues and the associated delays, the tMRI data was finally sourced after contacting the international research community. However, even this was fraught with ethical issues and it was only in the last 4 months of the project that the two tMRI datasets, using different techniques, were received from UCLA (Elliot McVeigh) and from the Cardiac Atlas Project (Alistair Young). The slices from UCLA were acquired using an advanced tagging technique that produces non-visual tags whereas the dataset from the Cardiac Atlas Project used a basic tagging technique, producing visual tissue tags.

The ‘Extract Features’ module of the SEP was most affected as a result of the difficulty and delays in obtaining the required tMRI dataset. Ideally, an automated or semi-automatic segmentation technique would be employed to use as

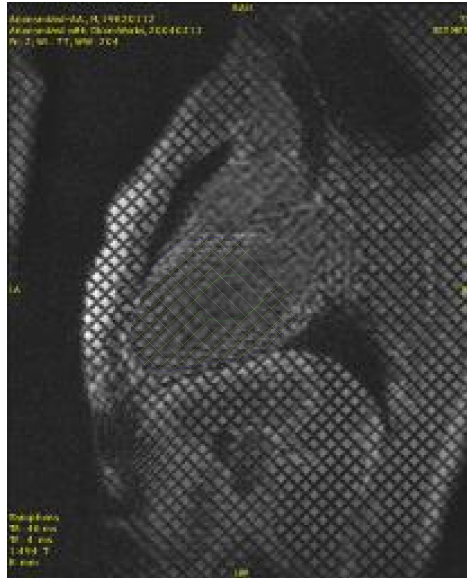


Figure 6.1: Initial tMRI image before segmentation

part of the SEP but due to the time constraints of this project manual segmentation was opted for. This meant that once the image slices were segmented the svg files required further processing to convert them into the required VS format making the whole thing an extremely time consuming job. The manual segmentation of tMRI data is time consuming due to the quality and size of the images as seen in figure 6.1.

6.2 Future work

The following sections discuss briefly the areas in which further research can be conducted. The first section deals with the limitations of the diagnostic tool as it exists and the direction of further research to improve it, while the next section deals with extending the tool.

6.2.1 Limitations of current SEP tool

The first subsection discusses the ‘Extract Features’ module while the next one discusses the modifications that can be made to the ‘Estimate Motion’ module

algorithms.

6.2.1.1 ‘Extract Features’

The obvious direction of future work with this research would be to implement an automatic or semi-automatic feature extraction module. As based on the initial exploration described in Chapter 3, the use of the Gradient Vector Flow snake would be the first method to be further investigated as it showed the most promise. The methods that would be investigated to detect the tag lines would include the use of non-rigid registration techniques and Gabor filters, as used by Montillo[MAM04] and Qian[QMA06].

An unfortunate consequence of the delay in obtaining the data and the resulting time constraint is that the non-visually tagged dataset was not processed at all. Thus, the next logical step when continuing the research would be to test how easily the SEP can be adapted to process advanced tMRI data. This is likely to involve changing the ‘Extract Features’ module to an algorithm involving the use of HARP techniques allowing the other modules to remain the same.

6.2.1.2 ‘Estimate Motion’

Despite the failure of the Lagrangian mechanics implementation of the ‘Estimate Motion’ module, it is worth further exploring its use because it is an effective way of accounting for the tissue properties within the motion estimation calculations. Since it is likely that the Lagrangian motion estimation was not successful due to an insufficient number of spring connections additional spring connections between the different tag planes, creating a 3D volume that is interconnected with springs, may provide better results and a stable Lagrangian motion estimation solution.

The results of the validation tests indicate that the error of the SEP results increases with each time step which may be due to the fact that the fading of the tags are not factored into the motion estimation algorithm. Although it could be caused by the cumulative error with a spatially aware selection this is unlikely in the basic selection as evident from the rmse graphs of chapter 5. A steadily increasing rmse for each time step may indicate a cumulative error

with the spatially aware selection algorithm whereas the stable rmse values that correspond to the time steps when the tags start fading in the case of the spatially ignorant selection implies that the fading tags are a concern that needs to be addressed in further development. As mentioned before, the tags in the tissue are not clearly visible for the entire duration of the heart beat. They continually fade during the heart beat until they are hard to discern towards the end of systole as shown in figure 2.1. This makes the segmentation difficult and error-prone since the tag lines fade into the surrounding tissue. Accounting for the inherent uncertainty caused by the fading of tags in the motion estimation calculations may thus reduce the increase in error of the SEP results over time.

A direct consequence of the fading of the tag lines on a slice and the subsequent difficulty in segmentation is that there is an added factor of error introduced. A possible solution to this error introduced by the segmentation, may be to add a component in the MC that speculates the error margin expected as a result of the fading. When the tags fade beyond a certain threshold level multiple motion paths can be estimated for each FEM point resulting in a range of possible values. The median can be used in the motion model and the remaining values indicated as the possible error margin. Alternatively, multiple estimations can be provided with a given a maximum expected margin of error. A single, compound estimation can then be calculated based on the overlap of the different calculated models or the smoothest return to the resting position.

6.2.2 Extending the diagnostic tool

Further research could take the path of extending the diagnostic tool to include the processing of the RV as well as extending the purpose of the tool to include the planning of treatment as discussed below.

6.2.2.1 Mathematical models

The model used for the simulated tMRI slices is guided by the required similarity to the LV chamber as well as the requirement of testing the sensitivity of the motion estimation to various possible variations in the geometry and its deformation. Variations could in future include force patterns that can simulate a

specific disease condition such as extent of ischaemic tissue as well as extending the model to simulate the RV. Additionally, more anatomically accurate models of both, the LV and RV, can be made with modifications to the ‘Create FEM’ module. These modifications may involve creating a model with varied ANSYS elements to account for the differences in geometry.

The future of this work would benefit if it included more extensive work into the materials properties that are best suited to model the LV.

The specification of all solid types often requires major tweaking between models, which meant that it may be difficult to keep the work flow automated. Since the tool required frequent intervention it may be useful to consider moving the finite element analysis into the SEP completely as a future step. However, it is important to recognise that ANSYS should play a part in the planning due to the vast capability and materials to choose from.

6.2.2.2 Treatment planning tool

Studies by [CMJ99] reveal that postischemia, regional strains increased significantly under low-dose dobutamine (within the noninfarcted but at risk regions), whereas regional strain remained unchanged within infarcted regions, thus allowing the identification of salvaged viable regions. Thus, the direction of future research can be to develop a treatment planning tool by assimilating the regional strain results of tMRI and delayed-enhancement imaging, to identify and assess the extent of myocardial ischaemia. The results of each MRI technique will complement the other and will be a better indicator of the extent of the disease, allowing for the detection and planning of treatment when viewed in a single model showing spatial correspondence.

Appendix A

A.1 Electrocardiogram (ECG)

As the heart undergoes depolarization and re-polarisation, the electrical currents that are generated by the heart is generally measured by an array of electrodes placed on the body surface and resulting tracing is called an electrocardiogram. ECG is important not only because it indicates cardiac function but also because it can be used in cardiac gating, a method employed to reduce motion artefacts produced as a result of heart motion and pulsatile blood flow. The ECG shows heart rate and rhythm and can indicate myocardial damage but gives no information on the adequacy of contraction. The ECG is virtually always transiently or permanently abnormal after acute myocardial infarction.

A.2 Ultrasound

Ultrasound in cardiology is a procedure that uses high frequency sound waves to observe the heart beating and image the tissue structure. Ultrasonic waves propagate sufficiently slowly that, for the distances travelled in the body transit times are easily measurable and is fast enough for the data needed for an image to be gathered. This can be done along with the reconstruction within 10-20 msec, which results in 'in vivo' visualising of the beating heart. Ultrasound images are formed very rapidly, essentially, in real time with low cost equipment. Coupled with the advantage of low risk of hazard, ultrasound is one of the most frequently used in diagnostic cardiac imaging. Ultrasound provides two types of information:

tissue position and velocity from the Doppler signal. Unfortunately, Doppler Effect is angle dependent, which means that only the component of velocity in the direction of beam can be measured meaning that only the axial component of the myocardial function can be measured. Additionally the strain components cannot be measured for all myocardial segments since the Doppler probe does not measure the velocity but the component of velocity in the direction of the beam. It also has a low resolution compared to CT, MRI, and radiographs.

A.3 Nuclear Medicine

Unlike CT imaging, Nuclear Medicine, does not image the anatomy of the body but monitors the distribution of radioactive elements that have been inhaled or injected for this purpose. The distribution of these agents or radiopharmaceuticals, is determined by factors such as blood flow, blood volume and a variety of metabolic processes. Thus temporal changes in the spatial distribution of radiopharmaceuticals can be obtained by multiple images and show basic function of the organ or system being examined. This form of imaging is also known as dynamic scintigraphy. Tomographic studies obtained by taking multi-view acquisition overcome most problems caused by the projection of 3D information on a single planar view. This technique is called Emission Computed Tomography (ECT). The technique of ECT can be classified into two separate modalities - Single-photon Emission Computed Tomography (SPECT) and Positron Emission Tomography (PET). SPECT and PET are used widely in cardiac imaging in order to detect coronary artery disease and evaluate the extent and severity of coronary stenosis, assess myocardial viability, outcome and efficacy of therapy. Since Nuclear Medicine is established on the principal of imaging the distribution of the radioisotope agent perfusion can be easily estimated. PET is currently the standard most accepted for the definitive determination of myocardial viability and also permits the in vivo, non-invasive quantitative measurement of myocardial blood flow. Therefore, its contribution in measuring myocardium perfusion is significant. Like CT scanning, Nuclear Medicine is based on the principles of radiology and reflects the same hazards. The amount of radiation from a nuclear medicine procedure is comparable to that received during a diagnostic CT. The

design of the radiopharmaceuticals substances is a challenge as it should fulfil several, often conflicting constraints. Relatively poor spatial resolution and signal to noise ratio are inherent problems for all nuclear medicine imaging methods in comparison to X-Ray or MR. However, as ECT is not an anatomical imaging technique by nature, it is not sensible to compare image quality directly with those obtained from anatomical modalities such as CT, ultrasound and magnetic resonance. The effectiveness of Nuclear Medicine does not lie in very high resolution but rather in its ability to monitor and image metabolic processes with very high sensitivity.

A.4 Magnetic Resonance Imaging

A.4.1 The machine

An MRI machine has a horizontal tube running through the magnet from front to back, called the bore of the magnet. The patient lying on the back slides into the bore on a special table. Once the body part to be scanned is in the exact centre of the magnetic field, the scan can begin. The first MRI exam performed on a human being was on the 3rd of July 1977. An MRI machine consists of two types of magnets, a main magnet and several gradient magnets. The system is rated based on the strength of the main magnet using a measure known as a Tesla. The main magnetic field needs to be one that is very uniform or homogeneous and of incredible strength and stability for high-quality imaging. The appendix describes magnets that make such magnetic fields possible. There are three gradient magnets inside the MRI machine, which are of extremely low strength compared to the main magnetic field. Typically the strength of the main magnet ranges from 0.5 to 3 Tesla and that of the gradient magnets range between 18 and 27 millitesla. The main magnet immerses the patient in a stable and very intense magnetic field, and the gradient magnets create a variable field. The rest of the MRI system consists of a very powerful computer system, equipment that allows the transmission of Radio Frequency pulses into the patient's body while they are in the scanner, and other secondary components.

A.4.2 Principles

The working of MRI is based on the spinning motion of specific nuclei present in biological tissue. The human body consists of billions of atoms with nuclei all randomly spinning or precessing in every direction. For the purposes of MRI the only atoms in the human body that is of concern are the hydrogen atoms. It is an ideal atom for MRI because its nucleus has a single proton and a large magnetic moment. The large magnetic moment means that, when placed in a magnetic field, the hydrogen atom has a strong tendency to line up with the direction of the magnetic field. The MRI machine applies an RF pulse that is specific only to hydrogen towards the area of the body that is to be imaged. The pulse causes the protons in that area to absorb the energy required to make them spin, or precess, in a different direction. This is the resonance part of MRI. The RF pulse forces them to spin at a particular frequency in a particular direction. The specific frequency of resonance is called the Larmour frequency and is calculated based on the particular tissue being imaged and the strength of the main magnetic field. These RF pulses are usually applied through a coil. MRI machines come with different coils for the many different parts of the body and usually conform to the contour of the body part being imaged. At approximately the same time, the three gradient magnets jump into the act. They are arranged in such a manner inside the main magnet that when they are turned on and off very rapidly in a specific manner, they alter the main magnetic field on a very local level. This means that an exact area can be pictured. The machine can be manipulated to get images from different directions with the gradient magnets. Thus a slice of any part of the body in any direction can be imaged which is a huge advantage over any other modality. Most imaging modalities use injectable contrast or dyes for certain procedures. MRI is no different. What is different is the type of contrast used, why and how it works. MRI contrast works by altering the local magnetic field in the tissue being examined. Normal and abnormal tissue will respond differently to this slight alteration, giving us differing signals. These varied signals are transferred to the images, allowing us to visualize many different types of tissue abnormalities and disease processes better than we could without the contrast. When the RF pulse is turned off,

A.4 Magnetic Resonance Imaging

the hydrogen protons begin slowly return to their natural alignment within the magnetic field and release their excess stored energy. When they do this, they give off a signal that the coil now picks up and sends to the computer system. What the system receives is mathematical data that is converted, through the use of a Fourier transform, into a picture that we can put on film. That is the imaging part of MRI.

Appendix B

B.1 Defining the conical volume

The position along the ring is easier to describe in Polar coordinates, with the radius, 'r' and the angle of rotation, 'theta'. This can however, be easily converted to the equivalent Cartesian coordinates using the trigonometric relationship in Figure B.1.

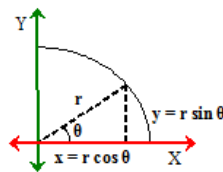


Figure B.1: Calculation of points on concentric circles of volume

Figure B.2 shows the trigonometric relationship between the variables defining the volume. The value of the radius, 'r' changes with 'h', and can be calculated using basic geometry theorem of similar triangles.

B.2 Defining the VTP

Types of intersections

There are four types of intersections that can occur between a VTL and the model. The first type is the case when the VTL passes through a node of the

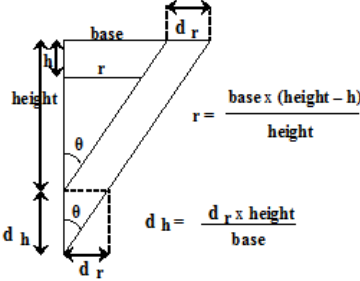


Figure B.2: Calculation of points along length of conical volume

model. The second type of intersection is when the VTL passes in between two adjacent nodes. The adjacency of nodes is checked along each of the three dimensions of ring, sector and level that are used in the definition of the model as explained before. The third type is when a VTL intersects a plane formed

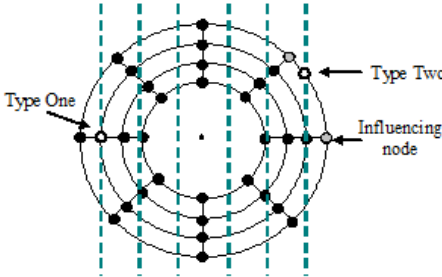


Figure B.3: Intersection types One & Two

by three neighbouring nodes, which is also checked along the three dimensions of the model, and the fourth is when a VTL intersects a plane formed by four neighbouring nodes of the model.

Calculations of intersection points

The first type of intersection does not require a calculation of the position, but the position of each of the other types of intersections are calculated using vector mathematics. The second is calculated as the intersection of two lines while the

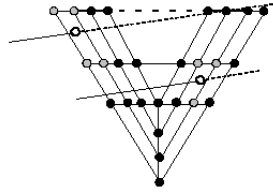


Figure B.4: Intersection types Three & Four

third and fourth types of intersection are the intersection of the VTL with the identified plane.

Padding of VTL

In cases where a VTL doesn't intersect the model at a sufficient number of positions it is padded with extra points. This means that extra points are inserted at a number of positions along the VTL depending on the distance between existing adjacent points. The padded points in a VTL are influenced by its neighbouring

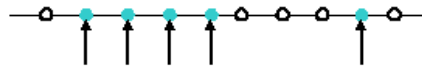


Figure B.5: Padding of a line with additional points

points in the VTL and are thus, only indirectly influenced by the nodes of the model. Using padded points and ensuring a minimum number of points in a VTL will thus make the VTP appear a relatively smooth surface.

B.3 Springs

B.3.1 Forces acting along a spring

The force exerted by a spring on the two connected particles p_0 and p_1 is equal and opposite and acts along the line connecting the particles. Thus if a force F_s acts on particle p_0 then $-F_s$ acts on p_1 . F_s is given by the following equation F_s

$= K_s (L - L_r)$ where K_s is the spring constant, L is the length of the spring and the L_r is the length of the spring at rest. The force caused by damping acting on the particles can be expressed as $F_d = -K_d (v_0 - v_1)$ where K_d is the coefficient of damping and v_0 and v_1 are the velocities of the two particles. The total force acting on a particle by a spring connected to it is given by $F = F_s + F_d$ ie. $F = (K_s (L - L_r) - K_d ((v_0 - v_1) \cdot L / |L - L_r|)) * L / |L - L_r|$. Hence F is the force acting on particle p_0 and $-F$ is the force acting on particle p_1 and $|L - L_r|$ is the magnitude of the vector connecting the two particles p_0 and p_1 .

References

- [ABW99] A.H. Aletras, R.S. Balaban, and H. Wen. High-resolution strain analysis of the human heart with fast-dense. *Journal of Magnetic Resonance*, 140(1):41–57, 1999. 21, 22
- [ACC⁺98] A.A. Amini, Y. Chen, R.W. Curwen, V. Mani, and J. Sun. Coupled b-snake grids and constrained thin-plate splines for analysis of 2d tissue deformations from tagged mri. *IEEE Transactions on Medical Imaging*, 17(3):344–356, 1998. 32, 33, 39, 43, 44, 70, 83
- [ACER01] A A Amini, Y Chen, M Elayyadi, and P Radeva. Tag surface reconstruction and tracking of myocardial beads from spamm-mri with parametric b-spline surfaces. *IEEE Transactions on Medical Imaging*, 20(2):94–103, 2001. 39, 44, 50, 83
- [AD89a] L. Axel and L. Dougherty. Heart wall motion: Improved method of spatial modulation of magnetization for mr imaging. *Radiology*, 172:349–350, 1989. 8, 24
- [AD89b] L. Axel and L. Dougherty. Mr imaging of motion with spatial modulation of magnetization. *Radiology*, 171(3):841–845, June 1989. 8, 18, 19, 24
- [ADBW99] A.H. Aletras, S. Ding, R.S. Balaban, and H. Wen. Dense: displacement encoding with stimulated echoes in cardiac functional mri. *Journal of Magnetic Resonance Imaging*, 137:247–252, 1999. 8, 18, 21, 22

REFERENCES

- [AEOPS07] K.Z. Abd-Elmoniem, N.F. Osman, J.L. Prince, and M. Stuber. Zharp: three-dimensional motion tracking from a single image plane. *Magnetic Resonance in Medicine*, 58(1):639–651, 2007. 21, 83
- [AESOP07] K.Z. Abd-Elmoniem, S. Sampath, N.F. Osman, and J.L. Prince. Real-time monitoring of cardiac regional function using fastharp mri and region-of-interest reconstruction. *Biomedical Engineering, IEEE Transactions on*, 54(9):1650–1656, sept. 2007. 21
- [AGB92] L. Axel, R.C. Gonalves, and D. Bloomgarden. Regional heart wall motion: two-dimensional analysis and functional imaging with mr imaging. *Radiology*, 183:745–50, June 1992. 36
- [AHD⁺92] T. Arts, W.C. Hunter, A. Douglas, A.M.M. Muijtjens, and R.S. Reneman. Description of the deformation of the left ventricle by a kinematic model. *Journal of Biomechanics*, 25(10):1119 – 1127, 1992. 83
- [AMK05] L. Axel, A. Montillo, and D. Kim. Tagged magnetic resonance imaging of the heart: a survey. *Medical Image Analysis*, 9(4):376 – 393, 2005. `Functional Imaging and Modeling of the Heart - FIMH03` `Functional Imaging and Modeling of the Heart`. 20
- [APD⁺10] T. Arts, F.W. Prinzen, T. Delhaas, J.R. Milles, A.C. Rossi, and P. Clarysse. Mapping displacement and deformation of the heart with local sine-wave modeling. *IEEE Transactions on Medical Imaging*, 29(5):1114–1123, 2010. 37, 39
- [AW01] A.H. Aletras and H. Wen. Mixed echo train acquisition displacement encoding with stimulated echoes: an optimized dense method for in vivo functional imaging of the human heart. *Magnetic Resonance in Medicine*, 46(3):523–534, 2001. 21, 22

REFERENCES

- [BHF10] BHF. Coronary heart disease statistics. [online]. [Accessed 9th December 2010]. Available from World Wide Web: <http://www.bhf.org.uk/research/statistics/mortality.aspx>, 2010. British Heart Foundation. 1
- [Bho90] H.S. Bholra. Evaluating "literacy for development" projects, programs and campaigns: Evaluation planning, design and implementation, and utilization of evaluation results. Technical report, UNESCO Institute for Education; DSE [German Foundation for International Development], Hamburg, Germany, 1990. 81
- [BMZ90] B.D. Bolster, E. McVeigh, and E.A. Zerhouni. Myocardial tagging in polar coordinates with use of striped tags. *Cardiac Radiology*, 173(3):769–772, 1990. 8, 19
- [BR01] J. Bogaert and F.E. Rademakers. Regional nonuniformity of normal adult human left ventricle. *American Journal of Physiology - Heart and Circulatory Physiology*, 280:H610H620, 2001. 48
- [CBK⁺00] P. Clarysse, C. Basset, L. Khouas, P. Croisille, D. Friboulet, C. Odet, and I.E. Magnin. Two-dimensional spatial and temporal displacement and deformation field fitting from cardiac magnetic resonance tagging. *Medical Image Analysis*, 4(3):253–268, 2000. 37
- [CBW⁺08] B.P. Cupps, D.R. Bree, J.R. Wollmuth, A.C. Howells, R.K. Voeller, J.G. Rogers, and M.K. Pasque. Myocardial viability mapping by magnetic resonance-based multiparametric systolic strain analysis. *The Annals of Thoracic Surgery*, 86:1546–1553, 2008. 70
- [CHBS⁺10] N. Carranza-Herrezuelo, A. Bajo, F. Sroubek, C. Santamarta, G Cristobal, A Santos, and M J Ledesma-Carbayo. Motion estimation of tagged cardiac magnetic resonance images using variational techniques. *Computerized medical imaging and graphics the official journal of the Computerized Medical Imaging Society*, 34(6):514–522, 2010. 39

REFERENCES

- [CMJ99] P. Croisille, C.C. Moore, and R.M. et. al Judd. Differentiation of viable and nonviable myocardium by the use of three-dimensional tagged mri in 2-day old reperfused canine infarcts. *Circulation*, 99:284–291, 1999. 7, 39, 44, 48, 51, 159
- [CMR04] R. Chandrashekhara, R.H. Mohiaddin, and D. Rueckert. Analysis of myocardial motion in tagged mr images using non-rigid image registration. *IEEE Transactions on Medical Imaging*, 23:1245–1250, 2004. 40, 83
- [CY96] S. Chandra and Y. Yang. Simulations and demonstrations of localized tagging experiments. *Journal of Magnetic Resonance Imaging*, 11:285–288, 1996. 19
- [DAB⁺99] L. Dougherty, J.C. Asmuth, A.S. Blom, L. Axel, and R. Kumar. Validation of an optical flow method for tag displacement estimation. *IEEE Transactions on Medical Imaging*, 18(4):359–363, 1999. 41
- [DDJ04] X. Deng and T.S. Denney Jr. Three-dimensional myocardial strain reconstruction from tagged mri using a cylindrical b-spline model. *IEEE Transactions on Medical Imaging*, 23(7):861–867, july 2004. 39, 46
- [DDJ05] X. Deng and T.S. Denney Jr. Combined tag tracking and strain reconstruction from tagged cardiac mr images without user-defined myocardial contours. *Journal of Magnetic Resonance Imaging*, 21(1):12–22, 2005. 39
- [DJM97] T.S. Denney Jr and E.R. McVeigh. Model-free reconstruction of three-dimensional myocardial strain from planar tagged mr images. *Journal of Magnetic Resonance Imaging*, 7(5):799–810, 1997. 39, 46, 47, 50
- [DJP95] T. Denney Jr and J. Prince. Reconstruction of 3d left ventricular motion from planar tagged cardiac images: An estimation theoretic

REFERENCES

- approach. *IEEE Transactions on Medical Imaging*, 14:625–635, December 1995. 39, 44
- [DP94] Jr. Denney, T.S. and J.L. Prince. Optimal brightness functions for optical flow estimation of deformable motion. *Image Processing, IEEE Transactions on*, 3(2):178–191, mar 1994. 32, 41
- [EG04] F.H. Epstein and W.D. Gilson. Displacement-encoded cardiac mri using cosine and sine modulation to eliminate (cansel) artifact-generating echoes. *Magnetic Resonance in Medicine*, 52(4):774–781, October 2004. 21, 22
- [EGG⁺02] T. Edvardsen, B.L. Gerber, J. Garot, D.A. Bluemke, J.A.C. Lima, and O.A. Smiseth. Quantitative assessment of intrinsic regional myocardial deformation by doppler strain rate echocardiography in humans: Validation against three-dimensional tagged magnetic resonance imaging. *Circulation*, 106(1):50–56, 2002. 51
- [Eps07] F.H. Epstein. Mri of left ventricular function. *Journal of Nuclear Cardiology*, 14(5):729–744, 2007. 51
- [FMMB93] S. Fischer, G. McKinnon, S Maier, and P. Boesiger. Improved myocardial tagging. *Journal of Magnetic Resonance and Medicine*, 30(2):191–200, August 1993. 8, 18, 19
- [FMS⁺94] S.E. Fischer, G.C. McKinnon, M.B. Scheidegger, W. Prins, D. Meier, and P. Boesiger. True myocardial motion tracking. *Magnetic Resonance in Medicine*, 31(4):401–413, 1994. 19, 46
- [FPSO06] A.S. Fahmy, L. Pan, M. Stuber, and N.F. Osman. Correction of through-plane deformation artifacts in stimulated echo acquisition mode cardiac imaging. *Magnetic Resonance in Medicine*, 55:404–412, 2006. 21, 22
- [FvA10] L. Florack and H. van Assen. A new methodology for multiscale myocardial deformation and strain analysis based on tagging mri. *International Journal of Biomedical Imaging*, 2010:8, 2010. 39

REFERENCES

- [GCRK98] K.J. Grande, R.P. Cochran, P.G. Reinhall, and K.S. Kunzelman. Stress variations in the human aortic root and valve: The role of anatomic asymmetry. *Annals of Biomedical Engineering*, 26:534–545, 1998. 10.1114/1.122. 59
- [GPAT97] S. Gupta, J. Prince, and S. Androutsellis-Theotokis. Bandpass optical flow for tagged mr imaging. *International Conference on Image Processing*, 3:364, 1997. 37, 39, 41
- [GZM97] M.A. Guttman, E.A. Zerhouni, and E. McVeigh. Analysis of cardiac function from mr images. *IEEE Computer Graphics and Applications*, 17(1):30–38, January-February 1997. 4, 6, 20, 32, 36, 51
- [HADRA99] J. Huang, D. Abendschein, V.G. Dvila-Romn, and A.A. Amini. Spatio-temporal tracking of myocardial deformations with a 4-d b-spline model from tagged mri. *IEEE Transactions on Medical Imaging*, 18(10):957–972, 1999. 39, 44, 83
- [HM09] D. Herzka and E. McVeigh. Mri of myocardial infarction with tissue tagging. *Current Cardiovascular Imaging Reports*, 2:73–82, 2009. 10.1007/s12410-009-0010-0. 20
- [HMA98] E. Haber, D.N. Metaxas, and L. Axel. Motion analysis of the right ventricle from mri images. In *Proceedings of the First International Conference on Medical Image Computing and Computer-Assisted Intervention, MICCAI '98*, pages 177–188, London, UK, 1998. Springer-Verlag. 30, 38, 39, 45, 47
- [HMA00a] I. Haber, D.N. Metaxas, and L. Axel. Three-dimensional motion reconstruction and analysis of the right ventricle using tagged mri. *Medical Image Analysis*, 4(4):335 – 355, 2000. 36, 45, 47
- [HMA00b] I. Haber, D.N. Metaxas, and L. Axel. Using tagged mri to reconstruct a 3d heartbeat. *Computing in Science and Engg.*, 2:18–30, September 2000. 28, 32, 38, 47, 50, 51, 70

- [HMA03] Z. Hu, D. Metaxas, and L. Axel. In vivo strain and stress estimation of the heart left and right ventricles from mri images. *Medical Image Analysis*, 7(4):435–444, 2003. 39, 51
- [HS81] B.K.P. Horn and B.G. Schunck. Determining optical flow. *ARTIFICIAL INTELLIGENCE*, 17:185–203, 1981. 40
- [HZS⁺09] A.T. Hess, X. Zhong, B.S. Spottiswoode, F.H. Epstein, and E.M. Meintjes. Myocardial 3d strain calculation by combining cine displacement encoding with stimulated echoes (dense) and cine strain encoding (senc) imaging. *Magnetic Resonance in Medicine*, 62(1):77–84, 2009. 9
- [Ibr11] E.H. Ibrahim. Myocardial tagging by cardiovascular magnetic resonance: evolution of techniques–pulse sequences, analysis algorithms, and applications. *Journal of Cardiovascular Magnetic Resonance*, 13:1–40, 2011. 17, 19, 20, 21, 22
- [IS02] V.N. Ikonomidou and G.D. Sergiadis. A rotational approach to localized spamm 11 tagging. *Journal of Magnetic Resonance*, 157(2):218 – 222, 2002. 19
- [IS03] V.N. Ikonomidou and G.D. Sergiadis. Multirate spamm tagging. *IEEE Transactions on Biomedical Engineering*, 50:1045–1051, 2003. 19
- [ISF⁺07] E.H. Ibrahim, M. Stuber, A.S. Fahmy, K.Z. Abd-Elmoniem, T. Sasano, M.R. Abraham, and N.F. Osman. Real-time mr imaging of myocardial regional function using strain-encoding (senc) with tissue through-plane motion tracking. *Journal of Magnetic Resonance Imaging*, 26(6):1461–1470, 2007. 21, 22
- [ISK⁺07] E.H. Ibrahim, M. Stuber, D.L. Kraitchman, R.G. Weiss, and N.F. Osman. Combined functional and viability cardiac mr imaging in a single breathhold. *Magnetic Resonance in Medicine*, 58(4):843–849, 2007. 21, 22

REFERENCES

- [JCM05] D.G. Julian, J.C. Cowan, and McLenachan. *Cardiology*. Elsevier Saunders, 8th edition edition, 2005. 3, 5
- [KG94] S. Kumar and D. Goldgof. Automatic tracking of spamm grid and the estimation of deformation parameters from cardiac mr images. *IEEE Transactions on Medical Imaging*, 13(1):122–132, March 1994. 35, 82
- [KMG⁺00] J.P.A. Kuijer, J.T. Marcus, M.J.W. Götte, A.C. van Rossum, and R.M. Heethaar. Three-dimensional myocardial strain analysis based on short- and long-axis magnetic tagged images using a 1d displacement field. *Magnetic Resonance Imaging*, 18:553–564, 2000. 39, 46, 50
- [KMG⁺02] J.P.A. Kuijer, J.T. Marcus, M.J.W. Götte, A.C. van Rossum, and R.M. Heethaar. Three-dimensional myocardial strains at end-systole and during diastole in the left ventricle of normal humans. *Journal of Cardiovascular Magnetic Resonance*, 4(3):341–351, 2002. 51
- [KP98] W. Kerwin and J. Prince. Cardiac material markers from tagged mr images. *Medical Image Analysis*, 2(4):339–353, 1998. 39, 42, 43, 45, 52, 75, 83
- [KYCA95] D. Kraitchman, A. Young, C. Chang, and L. Axel. Semi-automatic tracking of myocardial motion in mr tagged images. *IEEE Transactions on Medical Imaging*, 14(2):422–432, September 1995. 35, 36, 83
- [Lan09] S. Lankton. Sparse field methods - technical report. Technical report, Georgia Institute of Technology, 2009. 77, 79
- [LCBSM⁺06] M.J. Ledesma-Carbayo, A. Bajo, C. Santa Marta, E. Perez-David, M.A. Garcia-Fernandez, M. Desco, and A. Santos. Fully automatic cardiac motion estimation from tagged mri using non-rigid registration techniques. *Computers in Cardiology*, 33:305306, 2006. 40

-
- [MA92] E.R. McVeigh and E. Atalar. Cardiac tagging with breath-hold cine mri. *Magnetic Resonance in Medicine*, 28(2):318–327, 1992. 8, 19
- [MAM03] A. Montillo, L. Axel, and D. Metaxas. Automated correction of background intensity variation and image scale standardization in 4d cardiac spamm-mri. In *International Society for Magnetic Resonance in Medicine*, page 708, 2003. 34, 35
- [MAM04] A. Montillo, L. Axel, and D. Metaxas. Extracting tissue deformation using gabor filter banks. In *Proc of SPIE: Medical Imaging: Physiology, Function, and Structure from Medical Images*, volume 5369, pages 1–9, 2004. 37, 157
- [MB98] E.R. McVeigh and B.D. Jr. Bolster. Improved sampling of myocardial motion with variable separation tagging. *Magnetic Resonance in Medicine*, 39(4):657–661, 1998. 19
- [McV96] E.R. McVeigh. Mri of myocardial functions: Motion tracking techniques. *Magnetic Resonance Imaging*, 14(2):137–150, 1996. 23, 24
- [MLOMZ00] C.C. Moore, C.H. Lugo-Olivieri, E.R. McVeigh, and E.A. Zerhouni. Three-dimensional systolic strain patterns in the normal human left ventricle: Characterization with tagged mr imaging. *Radiology*, 214(2):453–466, 2000. 51
- [MMA02] A. Montillo, D. Metaxas, and L. Axel. Automated segmentation of the left and right ventricles in 4d cardiac spamm images. In Takeyoshi Dohi and Ron Kikinis, editors, *Medical Image Computing and Computer-Assisted Intervention (MICCAI 2002)*, volume 2488 of *Lecture Notes in Computer Science*, pages 620–633. Springer Berlin Heidelberg, 2002. 36, 84
- [MMA03] A. Montillo, D. Metaxas, and L. Axel. Automated model-based segmentation of the left and right ventricles in tagged cardiac

REFERENCES

- mri. In R.E. Ellis and T.M. Peters, editors, *Medical Image Computing and Computer Assisted Intervention (MICCAI)*, Montreal, Canada, volume 2878, page 507515. Springer, 2003. 36
- [MMMG04] J. MacKay, G.A. Mensah, S. Mendis, and K. Greenlund. *The Atlas of Heart Disease and Stroke*. Nonserial Publication. World Health Organization, 2004. 4
- [MOMZ92] C.C. Moore, W.G. Odell, E.R. McVeigh, and E.A. Zerhouni. Calculation of three-dimensional left ventricular strains from biplanar tagged mr images. *Journal of Magnetic Resonance Imaging*, 2:165–175, 1992. 39, 42, 45
- [MS90] T.J. Mosher and M.B. Smith. A dante tagging sequence for the evaluation of transitional sample motion. *Magnetic Resonance in Medicine*, 15:334–339, 1990. 8, 18, 19
- [MUAM03] A. Montillo, J.K. Udupa, L. Axel, and D.N. Metaxas. Interaction between noise suppression and inhomogeneity correction in mri. pages 1025–1036, 2003. 34
- [NRDJ98] T.D. Nguyen, S.J. Reeves, and T.S. Denney Jr. New magnetic resonance tagging technique for directly measuring the strain tensor of the in-vivo human heart. In *ICIP (1)*, pages 694–698, 1998. 24
- [NUZ00] L.G. Nyl, J.K. Udupa, and X. Zhang. New variants of a method of mri scale standardization. *IEEE Transactions on Medical Imaging*, pages 143–150, 2000. 35
- [OKMP99] N.F. Osman, W.S. Kerwin, E.R. McVeigh, and J.L. Prince. Cardiac motion tracking using cine harmonic phase (harp) magnetic resonance imaging. *Magnetic Resonance in Medicine*, 42(6):1048–1060, 1999. 18, 21
- [OM99] C. Ozturk and E.R. McVeigh. Four-dimensional b-spline-based motion analysis of tagged cardiac mr images. In C.-T. Chen & A. V. Clough, editor, *Society of Photo-Optical Instrumentation*

REFERENCES

- Engineers (SPIE) Conference Series*, volume 3660 of *Society of Photo-Optical Instrumentation Engineers (SPIE) Conference Series*, pages 46–56, May 1999. 33, 36
- [OM00] C. Ozturk and E.R. McVeigh. Four-dimensional b-spline based motion analysis of tagged mr images: introduction and in vivo validation. *Physics in medicine and biology*, 45(6):1683, 2000. 44
- [OMH⁺95] W. ODell, C. Moore, W. Hunter, E. Zerhouni, and E. McVeigh. 3d myocardial deformations: Calculation with displacement field fitting to tagged mr images. *Radiology*, 195(3):829–835, 1995. 32, 39, 44, 46, 47, 50
- [OSAP01] N.F. Osman, S. Sampath, E. Atalar, and J.L. Prince. Imaging longitudinal cardiac strain on short-axis images using strain-encoded mri. *Magnetic Resonance in Medicine*, 46(2):324–334, 2001. 9, 18, 21, 22
- [Osm03] N.F. Osman. Detecting stiff masses using strain-encoded (senc) imaging. *Magn Reson Med.*, 49(3):605–8, 2003. 9
- [PM92] J. Prince and E. McVeigh. Motion estimation from tagged mr image sequences. *IEEE Transactions on Medical Imaging*, 11(1992):238–249, June 1992. 39, 41
- [PMA95] J. Park, D. Metaxas, and L. Axel. Volumetric deformable models with parameter functions: A new approach to the 3d motion analysis of the lv from mri-spamm. In *Proceedings of the Fifth International Conference on Computer Vision, ICCV '95*, pages 700–, Washington, DC, USA, 1995. IEEE Computer Society. 32
- [PMA03] K. Park, D. Metaxas, and L. Axel. A finite element model for functional analysis of 4d cardiac-tagged mr images. In RandyE. Ellis and TerryM. Peters, editors, *Medical Image Computing and Computer-Assisted Intervention - MICCAI 2003*, volume 2878 of *Lecture Notes in Computer Science*, pages 491–498. Springer Berlin Heidelberg, 2003. 36

REFERENCES

- [PMMA05] K. Park, A. Montillo, D. Metaxas, and L. Axel. Volumetric heart modelling and analysis. *Communications of the ACM*, 48(2):43–48, February 2005. 32, 39, 47, 50, 70
- [PMYA96] J. Park, D. Metaxas, A.A. Young, and L. Axel. Deformable models with parameter functions for cardiac motion analysis from tagged mri data. In *IEEE Transactions on Medical Imaging*, pages 437–442, 1996. 36, 43, 45, 47, 70, 83
- [PPLO05] L. Pan, J.L. Prince, J.A.C. Lima, and N.F. Osman. Fast tracking of cardiac motion using 3d-harp. *IEEE Transactions on Biomedical Engineering*, 52:1425–1435, 2005. 21
- [PRP⁺03] C. Petitjean, N. Rougon, F. Prteux, P. Cluzel, and P. Grenier. Measuring myocardial deformations in tagged mr image sequences using informational non-rigid registration. In *Proceedings of the 2nd international conference on Functional imaging and modeling of the heart*, FIMH'03, pages 162–172, Berlin, Heidelberg, 2003. Springer-Verlag. 40
- [PSK⁺06] L. Pan, M. Stuber, D.L. Kraitchman, D.L. Fritzges, W.D. Gilson, and N.F. Osman. Real-time imaging of regional myocardial function using fast-senc. *Magnetic Resonance in Medicine*, 55(2):386–395, 2006. 21, 22
- [QMA06] Z. Qian, D.N. Metaxas, and L. Axel. Extraction and tracking of mri tagging sheets using a 3d gabor filter bank. In *Engineering in Medicine and Biology Society, 2006. EMBS '06. 28th Annual International Conference of the IEEE*, pages 711 –714, 30 2006-sept. 3 2006. 37, 39, 157
- [REW06] I. Rodriguez, D.B. Ennis, and H. Wen. Noninvasive measurement of myocardial tissue volume change during systolic contraction and diastolic relaxation in the canine left ventricle. *Magn Reson Med*, 2006. 57, 103

-
- [RPP⁺05] N. Rougon, C. Petitjean, F. Prteux, P. Cluzel, and P. Grenier. A non-rigid registration approach for quantifying myocardial contraction in tagged mri using generalized information measures. *Medical Image Analysis*, 9(4):353 – 375, 2005. *Functional Imaging and Modeling of the Heart - FIMH03*. 40, 83
- [RTK⁺09] I.K. Russel, S.R. Tecelao, J.P.A. Kuijer, R.M. Heethaar, and J.T. Marcus. Comparison of 2d and 3d calculation of left ventricular torsion as circumferential-longitudinal shear angle using cardiovascular magnetic resonance tagging. *Journal of Cardiovascular Magnetic Resonance*, 11(1):1–7, 2009. 46
- [SCO⁺09] M.L. Shehata, S. Cheng, N.F. Osman, D.A. Bluemke, and J.A.C. Lima. Myocardial tissue tagging with cardiovascular magnetic resonance. *Journal of Cardiovascular Magnetic Resonance*, 11:55, 2009. 51
- [SDA⁺03] S. Sampath, J.A. Derbyshire, E. Atalar, N.F. Osman, and J.L. Prince. Real-time imaging of two-dimensional cardiac strain using a harmonic phase magnetic resonance imaging (harp-mri) pulse sequence. *Magnetic Resonance in Medicine*, 50(1):154–163, 2003. 9, 21
- [SKF12] R.M. Simpson, J. Keegan, and D.N. Firmin. Mr assessment of regional myocardial mechanics. *Journal of Magnetic Resonance Imaging*, pages n/a–n/a, 2012. 8, 9, 10
- [SLSB03] M.A. Spiegel, R. Luechinger, J. Schwitter, and P. Boesiger. Ring-tag: ring-shaped tagging for myocardial centerline assessment. *Investigative Radiology*, 38:669–678, 2003. 19
- [SOP09] S. Sampath, N. Osman, and J. Prince. A combined harmonic phase and strain-encoded pulse sequence for measuring three-dimensional strain. *Magnetic Resonance Imaging*, 27(1):55–61, 2009. 9

REFERENCES

- [SP07] S. Sampath and J.L. Prince. Automatic 3d tracking of cardiac material markers using slice-following and harmonic-phase {MRI}. *Magnetic Resonance Imaging*, 25(2):197 – 208, 2007. 83
- [SSC⁺99] P. Shi, A.J. Sinusas, R.T. Constable, J.S. Duncan, T. Kanade, and O. Faugeras. Volumetric deformation analysis using mechanics-based data fusion: Applications in cardiac motion recovery. *International Journal of Computer Vision*, 35:87–107, 1999. 48
- [SSF⁺99] M. Stuber, M.A. Spiegel, S.E. Fischer, M.B. Scheidegger, P.G. Danias, E.M. Pedersen, and P. Boesiger. Single breath-hold slice-following cspamm myocardial tagging. *Magnetic Resonance Materials in Biology, Physics, and Medicine*, 9(1-2):85 – 91, 1999. 19
- [SU01] P.K. Saha and J.K. Udupa. Scale-based diffusive image filtering preserving boundary sharpness and fine structures. *Medical Imaging, IEEE Transactions on*, 20(11):1140–1155, November 2001. 34
- [TA06] N.J. Tustison and A.A. Amini. Biventricular myocardial strains via nonrigid registration of anatomical nurbs models. *Medical Imaging, IEEE Transactions on*, 25(1):94–112, 2006. 83
- [TAA04] N.J. Tustison, D. Abendschein, and A.A. Amini. Biventricular myocardial kinematics based on tagged mri from anatomical nurbs models. In *Proceedings of the 2004 IEEE computer society conference on Computer vision and pattern recognition, CVPR'04*, pages 514–519, Washington, DC, USA, 2004. IEEE Computer Society. 70
- [TADRA02] N.J. Tustison, D.R. Abendschein, V. Davila-Romn, and Amini A.A. Myocardial strain imaging with tagged mri. In *Proceedings of 16th International Conference on Pattern Recognition*, pages 723–726, Los Alamitos, 2002. IEEE. 46, 70
- [TDRA03] N.J. Tustison, V.G. Davila-Roman, and A.A. Amini. Myocardial kinematics from tagged mri based on a 4-d b-spline model. *Biomedical Engineering, IEEE Transactions on*, 50(8):1038 –1040, aug. 2003. 39, 50

-
- [WA12] H. Wang and A.A. Amini. Cardiac motion and deformation recovery from mri: A review. *Medical Imaging, IEEE Transactions on*, 31(2):487–503, feb. 2012. 11
- [WCA01] Y. Wang, Y. Chen, and A.A. Amini. Fast lv motion estimation using subspace approximation techniques. *IEEE Transactions on Medical Imaging*, 20(6):499–513, June 2001. 39, 44
- [WLY04] B.C. Wnsche, R. Lobb, and A.A. Young. The visualization of myocardial strain for the improved analysis of cardiac mechanics. In *Proceedings of the 2nd international conference on Computer graphics and interactive techniques in Australasia and South East Asia*, GRAPHITE '04, pages 90–99, New York, NY, USA, 2004. ACM. 52
- [WPD96] E. Waks, J.L. Prince, and A.S. Douglas. Cardiac motion simulator for tagged mri. In *Proceedings of Mathematical Methods in Biomedical Image Analysis*, pages 182–191, 1996. 83
- [WTT02] E.X. Wu, C.W. Towe, and H. Tang. Mri cardiac tagging using a sinc-modulated rf pulse train. *Magnetic Resonance in Medicine*, 48(2):389–393, 2002. 8
- [WY03] B. Wnsche and A.A. Young. The visualization and measurement of left ventricular deformation using finite element models. *J. Vis. Lang. Comput.*, pages 299–326, 2003. 52
- [XPI+10] C. Xu, J.J. Pilla, G. Isaac, J.H. Gorman III, A.S. Blom, R.C. Gorman, Z. Ling, and L. Dougherty. Deformation analysis of 3d tagged cardiac images using an optical flow method. *Journal of Cardiovascular Magnetic Resonance*, 12(1):1–14, 2010. 83
- [YA92] A. Young and L. Axel. Three-dimensional motion and deformation of the heart wall: Estimation with spatial modulation of magnetization a model-based approach. *Radiology*, 185:241–247, 1992. 50

REFERENCES

- [YAD⁺93] A. Young, L. Axel, L. Dougherty, D.K. Bogen, and C.S. Parenteau. Validation of tagging with mr imaging to estimate material deformation. *Radiology*, 188:101–108, 1993. 39, 83
- [YFA96] A.A. Young, Z.A. Fayad, and L. Axel. Right ventricular midwall surface motion and deformation using magnetic resonance tagging. *American Journal of Physiology - Heart and Circulatory Physiology*, 271:H2677–H2688, Dec 1 1996. 47
- [YKDA95] A. Young, D. Kraitchman, L. Dougherty, and L. Axel. Tracking and finite element analysis of stripe deformation in mr tagging. *IEEE Transactions on Medical Imaging*, 14(3):413–421, September 1995. 35, 43, 47, 70
- [You99] A.A. Young. Model tags: direct three-dimensional tracking of heart wall motion from tagged magnetic resonance images. *Medical Image Analysis*, 3(4):361 – 372, 1999. 36, 47
- [YRT⁺01] S.B. Yeon, N. Reichek, B.A. Tallant, J.A.C. Lima, L.P. Calhoun, N.R. Clark, E.A. Hoffman, K.K.L. Ho, and L. Axel. Validation of in vivo myocardial strain measurement by magnetic resonance tagging with sonomicrometry. *J Am Coll Cardiol*, 38(2):555–561, 2001. 7, 32
- [ZDY⁺96] S. Zhang, M.A. Douglas, L. Yaroslavsky, R.M. Summers, V. Dilsizian, L. Fananapazir, and S.L. Bacharach. A fourier based algorithm for tracking spamm tags in gated magnetic resonance cardiac images. *Medical Physics*, 23(8):1359–1369, 1996. 37
- [ZPR⁺88] E.A. Zerhouni, D.M. Parish, W.J. Rogers, A. Yang, and E.P. Shapiro. Human heart: Tagging with mr imaging - a new method for noninvasive assessment of myocardial motion. *Radiology*, 169(1):59–63, 1988. Cited By (since 1996): 646. 8, 18, 19